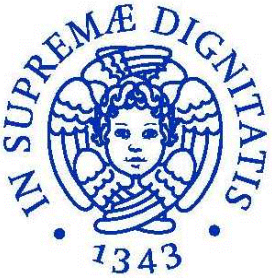

Università di Pisa

Facoltà di Scienze Matematiche Fisiche e Naturali

Corso di Laurea Specialistica in Scienze Fisiche

Anno Accademico 2006-2007

Tesi di Laurea Specialistica

The HAM-SAS Seismic Isolation System for the Advanced LIGO Gravitational Wave Interferometers

Candidato

Alberto Stochino

Relatori

Riccardo De Salvo

(California Institute of Technology)

Francesco Fidecaro

(Università di Pisa)

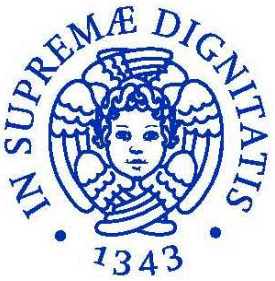

Università di Pisa

Facoltà di Scienze Matematiche Fisiche e Naturali

Corso di Laurea Specialistica in Scienze Fisiche

Anno Accademico 2006-2007

Tesi di Laurea Specialistica

The HAM-SAS Seismic Isolation System for the Advanced LIGO Gravitational Wave Interferometers

Candidato

Alberto Stochino

Relatori

Riccardo De Salvo

(California Institute of Technology)

Francesco Fidecaro

(Università di Pisa)

Ai miei genitori e ai miei fratelli

Abstract

The three LIGO interferometers are full operative and under science run since November 2005. The acquired data are integrated with those obtained by th Virgo experiment within an international cooperation aimed to maximize the efforts for the detection of gravitational waves.

From 2001 LIGO I is expected to be shut down and the construction and commissioning of Advanced LIGO to start. The objective of the new generation interferometers is a ten times greater sensibility with the purpose to extend of a factor of a thousand the space volume covered and to increase of the same order of magnitude the probability to detect events.

To increase the sensibility in the band below 40 Hertz, the main source of noise that Advanced LIGO have to face is the seismic noise. In this perspective, the SAS group (Seismic Attenuation Systems) of LIGO has developed a class of technologies on which the HAM-SAS system is based. Designed for the seismic isolation of the output mode cleaner optics bench and more in general for all the HAM vacuum chambers of LIGO, HAM-SAS, with little variations, can be extended to the BSC chambers as well.

In HAM-SAS the legs of four inverted pendulums form the stage of attenuation of the horizontal degrees of freedom. Four GAS filters are included inside a rigid intermediate structure called Spring Box which is supported by the inverted pendulums and provide for isolation of the vertical degrees of freedom. The geometry is such that the horizontal degrees of freedom and the vertical ones are separate. Each GAS filter carries an LVDT position sensor and an electromagnetic actuator and so also each leg of the inverted pendulums. Eight stepper motors guarantee the DC control of the system.

A prototype of HAM-SAS has been constructed in Italy, at Galli & Morelli and then transferred to Massachusetts Institute of Technology in the US to be tested inside the Y-HAM vacuum chamber of the LIGO LASTI laboratory.

The test at LASTI showed that the vertical and horizontal degrees of freedom are actually uncoupled and can be treated as independent. It was possible to clearly identify the modes of the system and assume these as a basis by which to build a set of virtual position sensors and a set of virtual actuators from the real ones, respect with which the transfer function of the system was diagonal. Inside this modal space the control of the system was considerably simplified and more effective. We measured accurate physical plants responses for each degree of freedom and, based on these, designed specific control strategies. For the horizontal degrees of freedom we implemented simple control loops for the conservation of the static position and the damping of the resonances. For the vertical ones, be-

yond these functions, the loops introduced an electromagnetic anti-spring effect and lowered the resonance frequency.

The overall results was the achievement of the LIGO seismic attenuation requirements within the sensibility limits of the geophone sensors used to measured the performances.

The entire project, from the construction to the commissioning, occurred within a very tight time schedule which left scarce possibility to complete the expected mechanical setup. The direct access to the system became much rarer once the HAM chamber had been closed and the vacuum pumped. Some of the subsystems (among which the counterweights for the center of percussion of the pendulums and the "magic wands") could not be implemented and several operations of optimization (i.e. the lower tuning of the vertical GAS filters' resonant frequencies and the tilts' optimization) had no chance to be completed. Moreover the LASTI environment offered a seismically unfortunate location if compared with the sites of the observatories for which HAM-SAS have been designed. Nonetheless the performances measured on the HAM-SAS prototype were positive and the obtained results very encouraging and leave us confident to be further improved and extended by keeping working on the system.

Riassunto

(*Italian Abstract*)

La presente tesi di laurea è il risultato della partecipazione del candidato allo sviluppo del sistema HAM-SAS per l'attenuazione del rumore sismico negli interferometri di Advanced LIGO.

I tre interferometri nei due osservatori di LIGO sono ormai operativi e in continua presa dati dal Novembre del 2005. I dati acquisiti sono integrati con quelli ottenuti dal progetto Virgo nell'ambito di una cooperazione internazionale volta a massimizzare gli sforzi per la rivelazione delle onde gravitazionali.

A partire dal 2011 sono previsti la dismessa di LIGO I e l'inizio dell'installazione e messa in funzione di Advanced LIGO. L'obiettivo degli interferometri di nuova generazione è una sensibilità dieci volte maggiore con lo scopo di estendere di un fattore mille il volume di spazio coperto e di incrementare dello stesso ordine di grandezza la probabilità di rivelazione di eventi.

Per aumentare la sensibilità nella banda sotto 10 Hertz la principale fonte di rumore che Advanced LIGO deve fronteggiare è il rumore sismico. In tale prospettiva, il gruppo SAS (Seismic Attenuation Sistems) di LIGO ha sviluppato un insieme di tecnologie sulle quali si basa il sistema HAM-SAS, progettato per l'isolamento sismico del banco ottico dell'output mode cleaner e più in generale per tutte le camere a vuoto HAM di LIGO.

In HAM-SAS le gambe di quattro pendoli invertiti costituiscono lo stadio di attenuazione dei gradi di libertà orizzontali (yaw e le due traslazioni sul piano). Quattro filtri GAS sono contenuti all'interno di una struttura rigida intermedia chiamata *Spring Box* che poggia sui pendoli invertiti e provvedono all'isolamento dei gradi di libertà verticali (traslazione verticale e le inclinazioni). La geometria è tale che i gradi di libertà orizzontali e quelli verticali risultano separati. Ogni filtro GAS è accompagnato da un sensore di posizione LVDT e da un attuatore elettromagnetico e così anche ogni gamba dei pendoli invertiti. Otto stepper motors permettono il controllo di posizione statica del sistema.

Un prototipo di HAM-SAS è stato realizzato in Italia e quindi trasportato presso il Massachusetts Institute of Technology negli Stati Uniti d'America per essere testato entro la camera a vuoto Y-HAM dell'interferometro da 15 metri del LIGO LASTI Laboratory.

La collaborazione del candidato al progetto è cominciata nel 2005 con lo studio di uno dei sottosistemi di HAM-SAS, le cosiddette "magic wands", oggetto della tesi di laurea di primo livello e ora parte integrante della tecnica SAS. Nell'Agosto del 2006 un maggiore coinvolgimento è cominciato con la partecipazione alle varie fasi di costruzione del sistema presso le officine meccaniche

della Galli e Morelli di Lucca. Il contributo alla costruzione in Italia ha incluso: il design di alcuni elementi, il processo di produzione dell'acciaio maraging per le lame dei filtri GAS, l'assemblaggio dell'intero sistema in tutte le sue parti meccaniche inclusi sensori, attuatori elettromagnetici e stepper motors e le caratterizzazioni preliminari dei pendoli invertiti e dei filtri GAS. Il sistema è stato inoltre interamente sottoposto ai processi di trattamento per la compatibilità con gli ambienti ad ultra alto vuoto dell'interferometro e in questa fase un contributo sono stati i test spettroscopici tramite FT-IR dei campioni ricavati dal sistema. Durante l'assemblaggio definitivo in camera pulita, come spiegato nell'elaborato, l'impegno è andato dal tuning dei filtri GAS, alla distribuzione precisa dei carichi sui pendoli invertiti e alla messa a punto del sistema per la correzione del tilt verticale.

All'MIT, a cominciare da Dicembre 2006, il candidato ha rappresentato il progetto HAM-SAS per tutta la sua durata. Qui si è occupato, assieme al gruppo SAS, di tutte le fasi dell'esperimento, dal setup dell'elettronica e della meccanica al commissioning del sistema per raggiungere i requisiti di progetto, passando per la creazione del sistema di acquisizione dati, i controlli, l'analisi dei dati e l'interpretazione dei risultati.

I test a LASTI hanno mostrato che, grazie alla particolare geometria del sistema, i gradi di libertà orizzontali e quelli verticali sono disaccoppiati e possono essere trattati come indipendenti. E' stato possibile identificare chiaramente i modi del sistema e assumerli come base con cui costruire un set di sensori di posizione virtuali e un set di attuatori virtuali a partire da quelli reali, rispetto ai quali la funzione di trasferimento del sistema fosse diagonale. All'interno di questo spazio modale il controllo del sistema è risultato notevolmente semplificato e più efficace. Abbiamo misurato accurate physical plant responses per ogni grado di libertà e, sulla base di queste, disegnato specifiche tipologie di controllo. Per i gradi di libertà orizzontali si sono utilizzati semplici loops di controllo per il mantenimento della posizione statica e il damping delle risonanze. Per quelli verticali in più a queste funzioni, i loops introducevano un effetto di antimolla elettromagnetica e abbassavano le frequenze di risonanza.

Il risultato complessivo è stato il raggiungimento dei requisiti di attenuazione sismica di LIGO per il banco ottico entro i limiti di sensibilità dei sensori geofoni utilizzati.

L'intero progetto, dalla produzione al commissioning, si è svolto secondo un programma dai tempi contingentati che ha lasciato scarsa possibilità di completare fino in fondo il setup meccanico previsto. L'accesso diretto al sistema è diventato molto più raro una volta richiusa la camera HAM nell'interferometro e pompato il vuoto. Alcuni dei sottosistemi (tra cui i contrappesi per il centro di percussione dei pendoli e le "magic wands") non hanno potuto essere installati e diverse operazioni di ottimizzazione (come l'abbassamento delle frequenze dei filtri GAS

verticali e dei pendoli invertiti e l'ottimizzazione dei tilt) non hanno potuto essere completate. Inoltre l'ambiente di LASTI ha offerto una locazione sismicamente poco favorevole se confrontata alle sedi degli osservatori per le quali HAM-SAS era stato progettato. Nondimeno le performance ottenute dal prototipo di HAM-SAS sono state positive e i risultati ottenuti molto incoraggianti e ci lasciano fiduciosi della possibilità che possano essere ulteriormente migliorati e ampliati dai lavori ancora in corso.

Aknowledgements

This thesis is the result of a significant experience, for my education as a physicist and my life overall. I am indebted to all the people who made it possible, who gave me a lot of valuable support during my work and also so much good time both in Lucca and Boston. I'd like to acknowledge them here.

First of all I want to thank my supervisors Riccardo De Salvo, who gave me this opportunity and has constantly and strongly supported my work teaching me an innumerable amount of things, and Francesco Fidecaro, who first introduced me to Virgo and LIGO. I would not be writing these lines if it wasn't for them.

The construction of HAM-SAS demanded a great effort and I have to thank Carlo Galli, Chiara Vanni e Maurizio Caturegli from Galli & Morelli. It would not have been possible without their deep commitment, and I would not have had such a good time in Lucca without them.

I also want to thank the many people of the HAM-SAS team for their continuous support during the project and for introducing me to the LIGO systems and in particular: Virginio Sannibale, Dennis Coyne, Yoichi Aso, Alex Ivanov, Ben Abbott, Jay Heefner, David Ottaway, Myron MacInnis, Bob Laliberte. It was a pleasure to work with them.

The LIGO department at MIT has been my house for eight months. I have to thank all the people there for their hearty hospitality and Marie Woods deserves a special thank for being always so kind and helping me with my relocation and my staying at MIT. I want also to thank: Richard Mittleman for being always available in the lab and his support in writing this thesis; Fabrice Matichard for all his valuable tips of mechanical engineering and for our enjoyable coffee breaks in the office; Brett Shapiro, Thomas Corbitt and Pradeep Sarin for their help and pleasant company in the control room.
I also want to thank MIT for letting me experience its exciting atmosphere for all these months.

I have to thank the LIGO Project, Caltech and the National Science Foundation for granting my visitor program, and in particular David Shoemaker and Albert Lazzarini. I'm also grateful to the Italian INFN for granting the beginning of my program.

I want to thank Luca Masini for all his logistic support in Pisa for this thesis. It would not even be printed without him.

The LIGO Observatories were constructed by the California Institute of Technology and Massachusetts Institute of Technology with funding from the National Science Foundation under cooperative agreement PHY 9210038. The LIGO Laboratory operates under cooperative agreement PHY-0107417. This paper has been assigned LIGO Document Number LIGO-P070083-00-R.

Contents

Chapter 1

Gravitational Waves Interferometric Detectors

According to general relativity theory gravity can be expressed as a spacetime curvature[1]. One of the theory predictions is that a changing mass distribution can create ripples in space-time which propagate away from the source at the speed of light. These freely propagating ripples in space-time are called gravitational waves. Any attempts to directly detect gravitational waves have not been successful yet. However, their indirect influence has been measured in the binary neutron star system PSR1913+16 [2].

This system consist of two neutron stars orbiting each other. One of the neutron stars is active and can be observed as a radio pulsar from earth. Since the observed radio pulses are Doppler shifted by the orbital velocity, the orbital period and its change over time can be determined precisely. If the system behaves according to general relativity theory, it will loose energy through the emission of gravitational waves. As a consequence the two neutron stars will decrease their separation and, thus, orbiting around each other at a higher frequency. From the observed orbital parameters one can first compute the amount of emitted gravitational waves and then the inspiral rate. The calculated and the observed inspiral rates agree within experimental errors (better than 1%).

1.1 Gravitational Waves

General Relativity predicts gravitational waves as freely propagating 'ripples' in space-time [3]. Far away from the source one can use the weak field approximation to express the curvature tensor $g_{\mu\nu}$ as a small perturbation $h_{\mu\nu}$ of the Minkowski metric $\eta_{\mu\nu}$:

$$g_{\mu\nu} = \eta_{\mu\nu} + h_{\mu\nu} \qquad \text{with} \quad \left|h_{\mu\nu}\right| \ll 1 \tag{1.1}$$

Using this ansaz to solve the Einstein field equations in vacuum yields a normal wave equation. Using the transverse-traceless gauge its general solutions can be written as

$$h_{\mu\nu} = h_+ (t - z/c) + h_\times (t - z/c) \tag{1.2}$$

where z is the direction of propagation and h_+ and $h_\times$ are the two polarizations (pronounced 'plus' and 'cross'):

$$h_+ (t - z/c) + h_\times (t - z/c) = \begin{pmatrix} 0 & 0 & 0 & 0 \\ 0 & h_+ & h_\times & 0 \\ 0 & -h_\times & h_+ & 0 \\ 0 & 0 & 0 & 0 \end{pmatrix} e^{\,(i\omega t - ikx)} \tag{1.3}$$

The above solution describes a quadrupole wave and has a particular physical interpretation. Let's assume two free masses are placed at positions x_1 and x_2 ($y = 0$) and a gravitational wave with + polarization is propagating along the z-axis, then the free masses will stay fixed at their coordinate positions, but the space in between|and therefore the distance between x_1 and x_2 will expand and shrink at the frequency of the gravitational wave. Similarly, along the y-axis the separation of two points will decrease and increase with opposite sign. The strength of a gravitational wave is then best expressed as a dimension-less quantity, the strain h which measures the relative length change $\Delta L = L$.

Denoting the quadrupole of the mass distribution of a source by Q, a dimensional argument|together with the assumption that gravitational radiation couples to the quadrupole moment only yields:

$$h \sim \frac{G\ddot{Q}}{c^4 r} \sim \frac{G\left(E_{\text{kin}}^{\text{non-simm}}/c^2\right)}{c^2 r} \tag{1.4}$$

with G the gravitational constant and $E_{\text{kin}}^{\text{non-simm}}$ the non symmetrict part of the kinetic energy. If one sets the non-symmetric kinetic energy equal to one solar mass

$$E_{\text{kin}}^{\text{non-simm}}/c^2 \sim M_\odot \tag{1.5}$$

and if one assumes the source is located at inter-galactic or cosmological distance, respectively, one obtains a strain estimate of order

$$h \lesssim 10^{-21} \qquad \text{Virgo cluster} \tag{1.6}$$

$$h \lesssim 10^{-23} \qquad \text{Hubble distance.} \tag{1.7}$$

By using a detector with a baseline of 10^4 m the relative length changes become of order:

$$\Delta L = hL \lesssim 10^{-19}\ \text{m to} 10^{-17}\ \text{m} \tag{1.8}$$

This is a rather optimistic estimate. Most sources will radiate significantly less energy in gravitational waves.

Similarly, one can estimate the upper bound for the frequencies of gravitational waves. A gravitational wave source can not be much smaller than its Schwarzshild radius $2GM/c^2$, and cannot emit strongly at periods shorter than the light travel time $4\pi GM/c^3$ around its circumference. This yields a maximum frequency of

$$f \leq \frac{c^3}{4\pi GM} \sim 10^4 \text{ Hz} \frac{M_\odot}{M} \tag{1.9}$$

From the above equation one can see that the expected frequencies of emitted gravitational waves is the highest for massive compact objects, such as neutron stars or solar mass black holes.

Gravitational waves are quite different from electro-magnetic waves. Most electro-magnetic waves originate from excited atoms and molecules, whereas observable gravitational waves are emitted by accelerated massive objects. Also, electro-magnetic waves are easily scattered and absorbed by dust clouds between the object and the observer, whereas gravitational waves will pass through them almost unaffected. This gives rise to the expectation that the detection of gravitational waves will reveal a new and different view of the universe. In particular, it might lead to new insights in strong field gravity by observing black hole signatures, large scale nuclear matter (neutron stars) and the inner processes of supernova explosions. Of course, stepping into a new territory also carries the possibility to encounter the unexpected and to discover new kinds of astrophysical objects.

1.2 Interferometric Detectors

An interferometer uses the interference of light beams typically to measure displace ments. An incoming beam is split so that one component may be used as a reference while another part is used to probe the element under test The change in interference pattern results in a change in intensity of the output beam which is detected by a photodiode. By using the wavelength of light as a metric interferometers can easily measure distances on the scales of nanometers and with care much more sensitive measurements may be made. The light source used is a laser, a highly collimated single frequency light making possible very sensitive interference fringes.

In a Michelson interferometer the laser beam is split at the surface of the beam splitter (BS) into two orthogonal directions. At the end of each arm a suspended mirror reflects the beam back to the BS. The beams reflected from the arms recombine on the BS surface. A fraction of the recombined beam transmits through

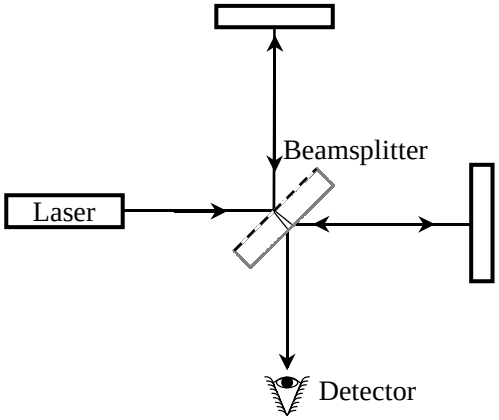

Figure 1.1: Scheme of a basic Michelson interferometer.

the BS and the rest is reflected from it. The intensity of each recombined beam is determined by the interferometer conditions and is detected by a photo detector (PD) that gives the differential position signal from the apparatus.

A Michelson interferometer can detect gravitational waves from the tidal action on the two end mirrors. The change of the metric between the two mirror because of a gravitational wave causes a phase shift detectable by the interferometer.

The optimal solution would be to build Michelson interferometers with arms as long as 1/2 of the GW wavelength, which would require hundreds or thousands of km. Folding the light path into an optical cavity (Fabry-Perot) is the solution applied to solve the problem.

The interferometric signal can be detected most sensitively by operating the interferometer on a dark fringe, when the resulting intensity at the photodetector is a minimum. Since power is conserved, and very little light power is lost in passing through the interferometer, most of the input laser power is reflected from the interferometer back towards the input laser. Since increasing laser power results in better sensitivity rather than 'waste' this reflected power, a partially transmitting mirror can be placed between the input laser and the beam splitter. This allows the entire interferometer to form an optically resonant cavity with a potentially large increase in power in the interferometer. This is called power recycling and is shown schematically by the mirror labeled PR in fig.1.2.

Based on this idea several interferometric detectors have been built in the world: a 3 Km detector in Italy (VIRGO) [40], a 600 m in Germany (GEO600) [41], a 300 m in Japan (TAMA) [42] and two twin 4 Km and a 2 Km in USA

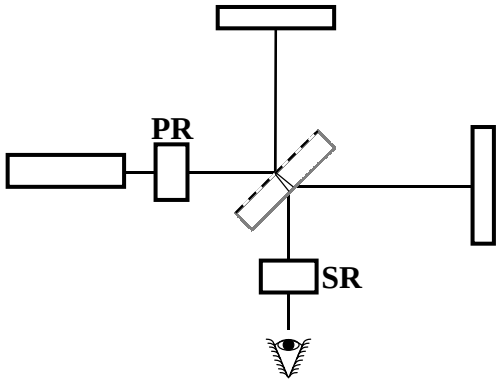

Figure 1.2: Power and signal recycling in a simple Michelson interferometer. Mirror PR reflects any exiting laser power back into the interferometer, while mirror SR reflects the output signal back into the system.

(LIGO) [17]. Virgo e LIGO are fully active, LIGO at nominal sensitivity and Virgo approaching it. All four observatories Virgo, LIGO and GEO are taking data as an unified network since May 2007.

1.2.1 The LIGO Interferometers

The LIGO Project consists of two observatories, one in Hanford, Washington, and the other in Livingston, Louisiana, 3000 Km far away from each other (fig.1.5) [47]. The Virgo interferometer, Located in Cascina, Italy, has 3 km long arms, while the smaller GEO in Hanover, Germany, has 800 m arms and no FP cavities. The four interferometers operate together and share data to maximize the effort to detect gravitational waves.

The two LIGO interferometers, with 4 Km long arms, operate in coincidence to reject local noise sources. Gradual improvement of the different parts of the detector are planned in forthcoming years; in LIGO the currently considered upgrades concern the laser (higher power), the mirror substrate, the mirror suspension (fused silica) and the seismic isolation system (this thesis is a contribution to the new seismic isolation system development). The spectral sensitivity curve of LIGO I is shown in fig.1.3 along with the contribution of the different sources of noise.

The low frequency limit of the detector is set by the cut-off of the "seismic wall", located for LIGO I above 40 Hz. At higher frequencies the sensitivity of the interferometer is limited from 40 to 120 Hz by the thermal noise of the mirror suspension. Above 120 Hz the shot noise dominates. Figure 1.4 shows the sensitivity improvement expected from LIGO II, whose start-up is scheduled for

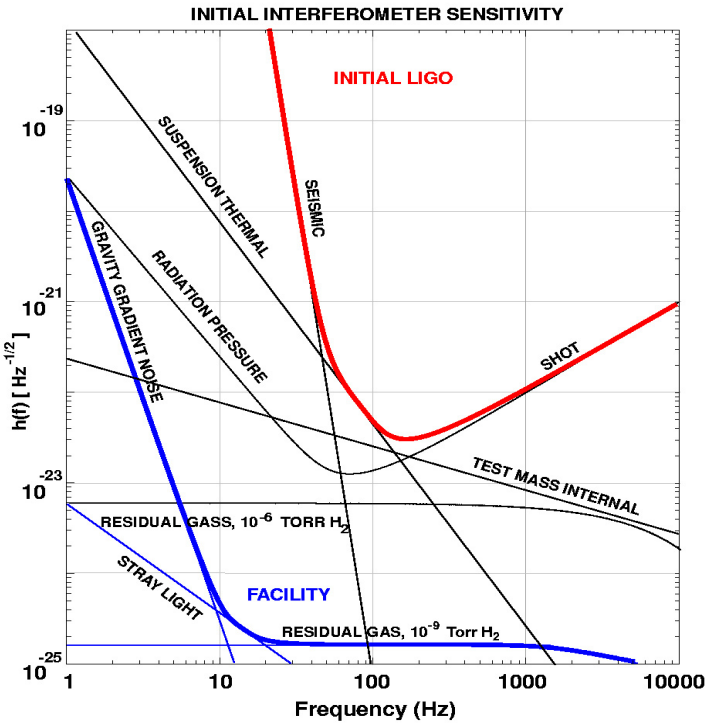

Figure 1.3: Initial LIGO strain sensitivity curve.

2011. [43].

1.3 Seismic Noise

Seismic motion is an inevitable noise source for interferometers built on the Earth's crust. The signal of an interferometer caused by the continuous and random ground motion is called seismic noise. The ground motion transmitted through the mechanical connection between the ground and the test masses results in perturbations of the test masses separation.

Since the ground motion is of the order of 10^{-6} m at 1 Hz and the expected GW signal is less than 10^{-18} m, we need attenuation factors of the order of 10^{-12}.

As the amplitude of the horizontal ground motion in general is larger at lower frequencies, the seismic motion will primarily limit the sensitivity of an interferometer in the low frequency band, usually below several tens of Hertz[1].

[1]Below 10 Hz the seismically induced variations of rock density produce fluctuations of the Newtonian attraction to the test mass that bypass any seismic attenuation system (Newtonian noise) and overwhelm any possible GW signal.

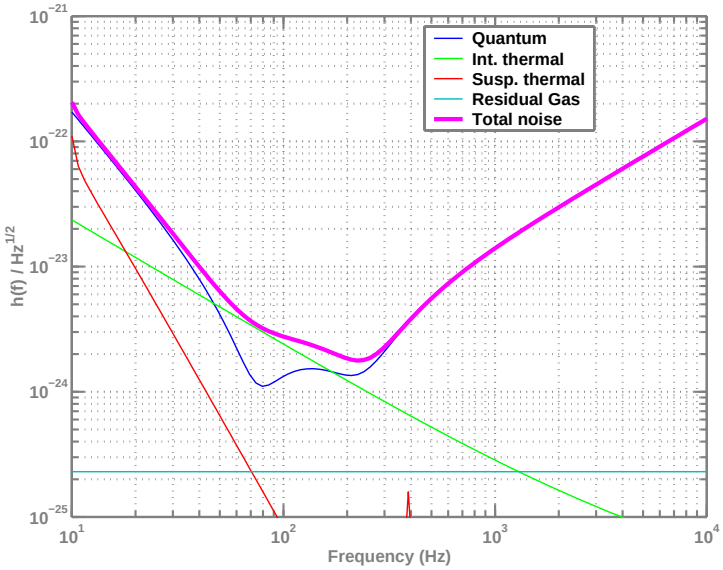

Figure 1.4: Advanced LIGO strain sensitivity curve.

A typical model for the power spectrum of the ground motion for above 100 mHz is given by

$$x = a/f^2 \quad [m/\sqrt{Hz}] \tag{1.10}$$

where a is a constant dependent on the site and varies from 10^{-7} to 10^{-9}. The model assumes the motion to be isotropic in the vertical and horizontal directions.

The surface waves that originate the seismic ground motion are a composed of Rayleigh waves (a mix of longitudinal and transversal waves that originate the horizontal displacement) and Lowes waves (transverse waves that originate the vertical motion). The ground can also have an angular mode of motion, with no translation. There is no direct measurement of the power spectrum associated to this kind of seismic motions, so a typical way to have an estimation is to consider the only contributions given by the vertical component of Rayleigh waves:

$$\theta = \frac{2\pi f}{c} S_v. \tag{1.11}$$

θ and S_v are the angular power spectrum ([rad/ $\sqrt{\text{Hz}}$]) and the vertical power spectrum ([m/ $\sqrt{\text{Hz}}$]), c is the local speed of the seismic waves. This depends mainly on the composition of the crust and it is also a function of the frequency. Lower speeds correspond to larger amplitude of the ground tilt, then the lowest values can be used to set an upper limit [23].

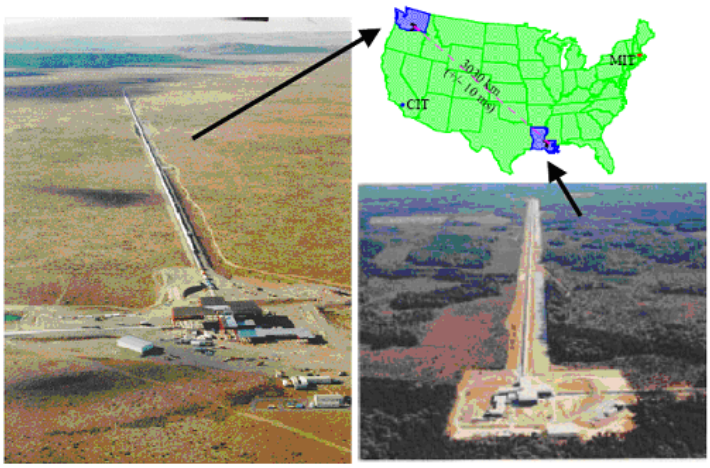

Figure 1.5: The LIGO interferometers are located in Louisiana (LLO) and in Washington (LHO).

1.3.1 Passive Attenuation

Large amounts of isolation can be achieved by cascading passive isolators. Passive isolators are fundamentally any supporting structure with a resonance Mechanically it is typically something heavy mounted on a soft support.

Consider the simple harmonic oscillator shown in fig.1.7 and compare the motion of the input x_0 with the motion of the output, x The restoring force on the mass m is supplied by the spring with spring constant k. Thus the equation of motion is

$$m\ddot{x} = -k\left(x\left(t\right) - x_0\left(t\right)\right). \tag{1.12}$$

This equation can be solved in the frequency domain by taking the Laplace transform (with Laplace variable $s = i\omega$ solving for the ratio of x to x_0. Defining the resonant frequency of the system as $\omega_0 = k/m$, the response of the isolated object to input motion is

$$\frac{x(s)}{x_0(s)} = \frac{1}{(s/\omega)^2 + 1}. \tag{1.13}$$

At low frequencies $\omega \to 0$ the expression approaches one and the output of the system matches closely the input. However, important for isolation, at high frequencies ($\omega \gg \omega_0$), the response of the output is $(\omega_0/\omega)^2$. Thus, at frequencies an order of magnitude or more above the resonant frequency of the stage a great deal of isolation can be achieved.

In any real system there is some loss in the system whether this is due to friction viscous damping or other mechanisms. For the simple oscillator described above some viscous damping may be introduced as a force proportional to the

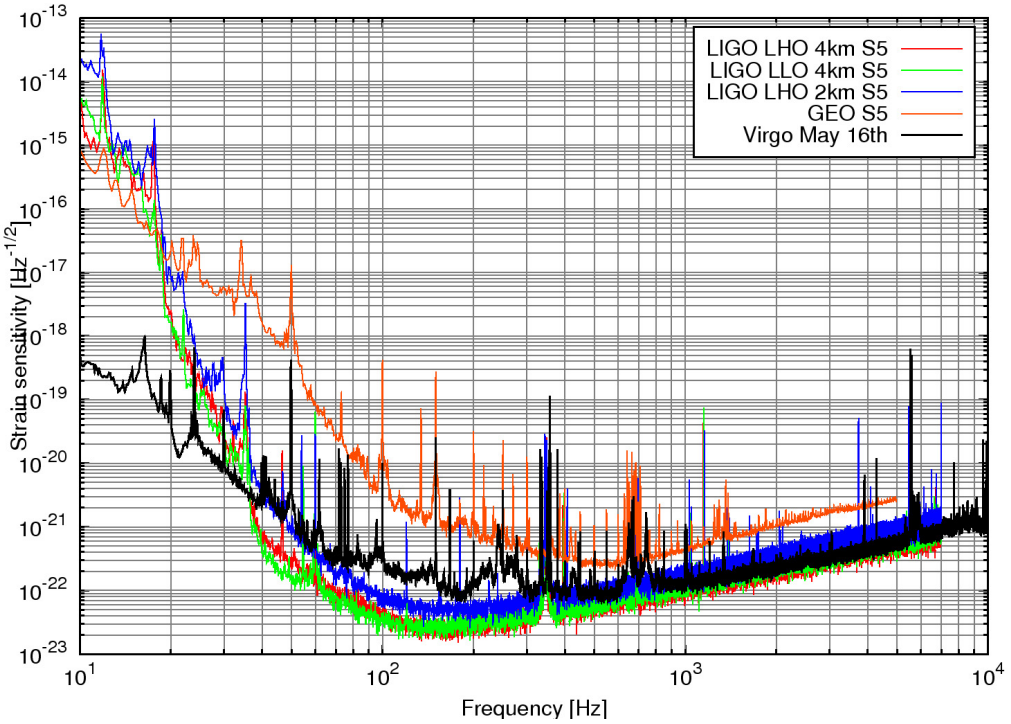

Figure 1.6: Recent sensitivity curve of the main operating GW interferometrs: GEO, LIGO (LLO and LHO), Virgo.

relative velocity, $F_v = -\gamma\,(\dot{x} - \dot{x_0})$. This represents for example the motion of this oscillator in air. Then the transfer function from ground input to mass output is

$$\frac{x(s)}{x_0(s)} = \frac{2\eta(s/\omega_0) + 1}{(s/\omega)^2 + 2\eta(s/\omega_0) + 1} \tag{1.14}$$

where the damping ratio η is given for this viscously damped case by $\eta = \gamma/2m\omega_0$. Particularly for systems with very little damping the system is often parametrized with the quality factor of the resonance, the Q rather than the damping ratio η, where

$$Q = \frac{1}{2\eta}. \tag{1.15}$$

The response of a system with $Q \approx 10$ is shown in fig.1.8. There are two important characteristics of the magnitude of the frequency response in contrast to a system with infinite Q. First, the height of the resonant peak at ω_0 is roughly Q times the low frequency response. Second, the response of the system is proportional to $(\omega_0/\omega)^2$ above the resonant frequency up to about a frequency $Q\omega_0$. Above this point the system response falls only as $1/\omega$. These conclusions are drawn for viscously damped systems. For low loss systems for any form of loss,

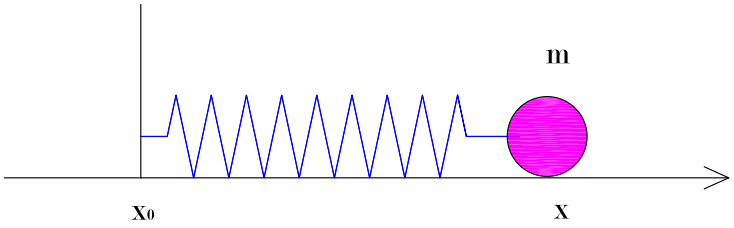

Figure 1.7: A one dimensional simple harmonic oscillator with spring constant k and mass m The mass is constrained to move frictionlessly in one direction horizontal

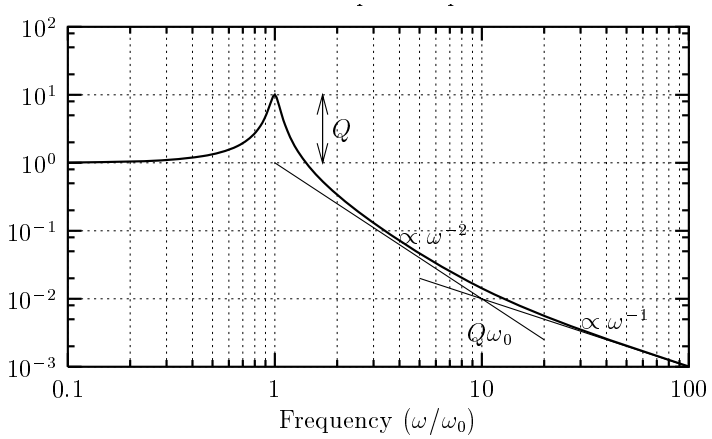

Figure 1.8: Response of a simple harmonic isolator with finite Q.

the system response will fall proportionally to $1/\omega^2$ for frequencies a decade or more above the resonant frequency.

Passive isolation has a number of advantages. A system is passive in that it supplies no energy to the system and thus requires no energy source as opposed to an active system, which senses the mechanical energy fed into the system and counter it with external forces. Because it adds no energy to the system, it is guaranteed to be stable. As it has fewer components than an active system, it can be considered more mechanically and electrically reliable. Its performance is not sensor or actuator limited.

The required seismic attenuation is obtained using a chain of mechanical oscillators of resonant frequency lower than the frequency region of interest. In the horizontal direction the simple pendulum is the most straightforward and effective solution: the suspension wire has a negligible mass and the attenuation factor behaves like $1/f^2$ till the first violin mode of the wire (tens or hundreds of Hertz). Thus, with reasonable pendulum lengths (tens of cm), good attenuation factors can be easily achieved in the frequency band of interest (above 10 Hz) for the x

and y directions. A simple pendulum is even more effective for the yaw mode; torsional frequencies of few tens of millihertz are easy to be obtained. A mass suspended by a wire has also two independent degrees of freedom of tilt, the pitch and the roll; low resonant frequencies (<0.5 Hz) and high attenuation factors for these modes are obtained by attaching the wire as close as possible to the center of mass of the individual filters.

The difficult part in achieving high isolation in all the 6 d.o.f.s is to generate good vertical attenuation. The vertical noise is, in principle, orthogonal to the sensitivity of the interferometer. Actually the 0.1-1% of the vertical motion is transferred to the horizontal direction at each attenuation stage by mechanical imperfections, misalignments and, ultimately (at the 10^{-4} level), by the non parallelism of verticality (the Earth curvature effects) on locations kilometers apart. The vertical attenuation then becomes practically as important as the others.

In the gravitational wave detectors, every test mass is suspended by a pendulum to behave as a free particle in the sensitive direction of the interferometer. The typical resonant frequency of the pendulum is 1 Hz. In such a case, at 100 Hz, the lowest frequency of the GW detection band, the attenuation factor provided in the pendulum is about 10^{-4}. From the simple model of the seismic motion (eq.1.10), neglecting the vertical to horizontal cross-couplings, and assuming a quiet site $a = 10^{-9}$, the motion of the test mass induced by the seismic motion reaches the order of $10^{-13}\mathrm{m}/\sqrt{\mathrm{Hz}}$, corresponding to a strain $h \sim 10^{-16}$ to 10^{-15} depending n the scale of the detector. This is far above the required level (typically at least 10^{-21} in strain), and the attenuation performance needs to be improved. This improvement can be easily achieved by connecting the mechanical filters in series. In the high frequency approximation, the asymptotic trend of the attenuation factor improves as $1/\omega^n$ where n is the number of the cascaded filters. Thence by adding a few more stages above the mirror suspension, one can realize the required attenuation performance by simply using the passive mechanics. An example of this strategy are the stack system composed by layers of rubber springs and heavy stainless steel blocks interposed between the mirror suspension system and the ground in LIGO, TAMA300 and GEO600.

Another way to improve the isolation performance is to lower the resonant frequency of the mechanics. By shifting lower the resonant frequencies, one can greatly improve the attenuation performance at higher frequency. Virgo utilized this approach and realized extremely high attenuation performance starting at low frequency (4 to 6 Hz) with the a low frequency isolation system coupled to a multi-stage suspension system called Supper Attenuator (SA) [31].

Chapter 2

HAM Seismic Attenuation System

The configuration of advanced LIGO is a power-recycled and signal-recycled Michelson interferometer with Fabry-Perot cavities in the arms - i.e., initial LIGO, plus signal recycling. The principal benefit of signal recycling is the ability to reduce the optical power in the substrates of the beamsplitter and arm input mirrors, thus reducing thermal distortions due to absorption in the material. To illustrate this advantage, the baseline design can be compared with a non-signalrecycled version, using the same input laser power but with mirror reflectivities re-optimized. The signal recycled design has a (single interferometer) NBI (Neutron Binary Inspiral) range of 200 Mpc, with a beamsplitter power of 2.1 kW; the non-SR design has a NBI range of 180 Mpc, but with a beamsplitter power of 36 kW. Alternatively, if the beamsplitter power is limited to 2.1 kW, the non-SR design would have a NBI range of about 140 Mpc.

An important new component in the design is an output mode cleaner. The principal motivation to include this is to limit the power at the output port to a manageable level, given the much higher power levels in the interferometer compared to initial LIGO.

With an output mode cleaner all but the TEM_{00} component of the contrast defect would be rejected by a factor of $\sim$1000, leaving an order 1 mW of carrier power. The OMC will be mounted in-vacuum on a HAM isolation platform, and will have a finesse of order 100 to give high transmission (>99 percent) for the TEM_{00} mode and high rejection (>1000) of higher order modes.

Earlier attempts to implement an external OMC failed because of seismic noise couplings. It was found necessary to implement a seismic attenuated, in-vacuum OMC and detection diodes.

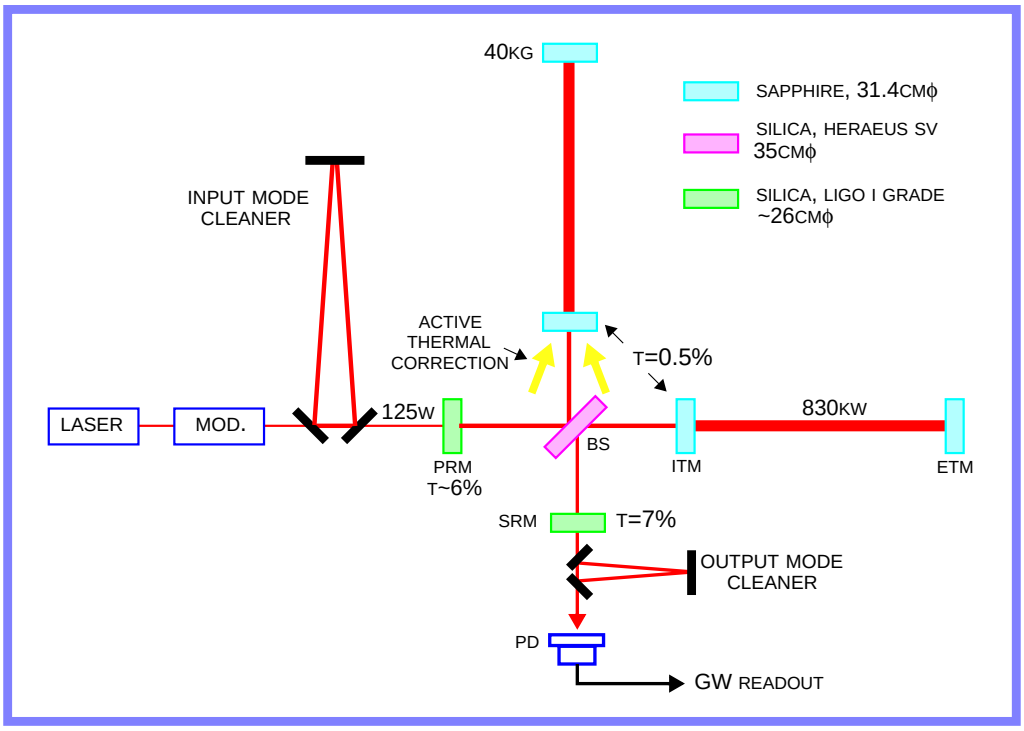

Figure 2.1: Basic layout of an advanced LIGO interferometer.

2.1 Seismic Isolation for the OMC

Isolation of the LIGO II optics from ambient vibration is accomplished by the seismic isolation systems which must provide the following functions:

- provide vibration isolated support for the payload(s)
- provide a mechanical and functional interface for the suspensions
- provide adequate space and flexibility for mounting of components (suspensions and auxiliary optics) and adequate space for access to components
- provide coarse positioning capability for the isolated supports/platforms
- provide external actuation suitable for use by the interferometer's global control system to maintain long-term positioning and alignment
- provide means for the transmission of power and signals from control electronics outside the vacuum chambers to the suspension systems and any other payloads requiring monitoring and/or control

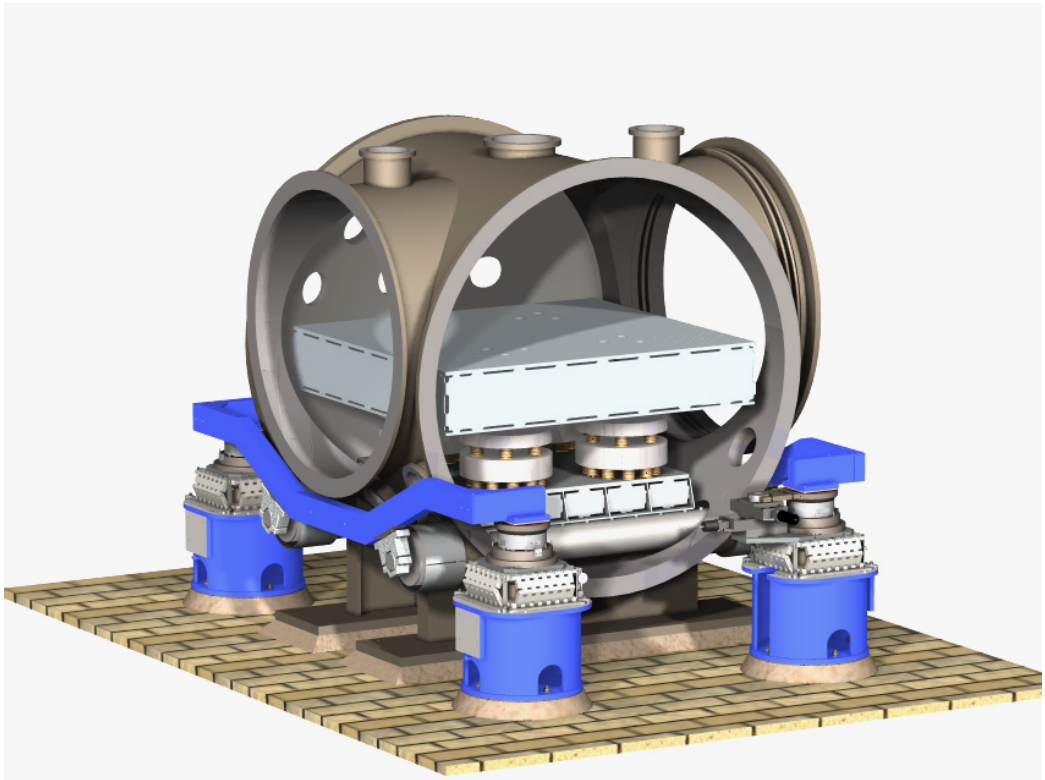

Figure 2.2: LIGO I HAM chamber with seismic attenuation stacks supporting the optics table.

- carry counter-weights to balance the payloads

To meet the requiremts above, the LIGO SAS team designed HAM-SAS, a single stage, passive attenuation unit based on the SAS technology [4]. It can satisfy the Ad-LIGO seismic attenuation specifications for all HAM optical benches by passive isolation and has built-in nanometric precision positioning, tide-tracking and pointing instrumentation. Its sensors and actuators are designed to allow easy upgrade to active attenuation. This upgrade would require the installation of a set of accelerometers and control logic and would add to the passive performance. Since in HAM-SAS the horizontal and vertical degrees-of-freedom (d.o.f.) are mechanically separated and orthogonal, active control loops are simple and easy to maintain. Additionally HAM-SAS brings to LIGO earthquake protection for seismic excursions as large as $\pm 1cm$.

HAM-SAS is designed to be implemented completely inside the present ultra high vacuum HAM chambers , replacing the present LIGO seismic attenuation stacks below the present optical benches (fig. 2.2). Consisting of a single attenuation layer, and re-using the existing optical benches, it is presented as a low

cost and less complex alternative to the Ad-LIGO baseline with three-stage active attenuation system [5, 6].

Also HAM-SAS is based on an technology akin to the multiple pendulum suspensions that it supports, thus offering a coherent seismic attenuation system to the mirror suspension.

Even though the specific design is adapted to the HAM vacuum chambers, the SAS system was designed to satisfy the requirements of the optical benches of the BSC chambers as well. HAM-SAS can be straightforwardly scaled up to isolate the heavier BSC optical benches.

Unlike the baseline Ad-LIGO active system, HAM-SAS does not require instrumentation on the piers [9, 10].

2.2 System Overview

HAM-SAS is composed of three parts:

- a set of four inverted pendulums (IP) for horizontal attenuation supported by a base plate;
- a set of four geometric anti spring (GAS) springs for vertical attenuation , housed in a rigid "spring box";
- eight groups of nm resolution linear variable differential transformers (LVDT), position sensors and non-contacting actuators for positioning and pointing of the optical bench. Micropositioning springs ensure the static alignment of the optical table to micrometric precision even in the case of power loss.

The existing optical bench is supported by a *spring-box* composed by two aluminum plates and the body of four GAS springs (fig. 2.3, 2.4). The GAS springs support the bench on a modified kinematical mount; each filter is provided with coaxial LVDT position sensors and voice coil actuators, and parasitic, micrometrically tuned, springs to control vertical positioning and tilts. The spring box is mounted on IP legs that provide the horizontal isolation and compliance. The movements of the spring-box are also controlled by four groups of co-located LVDT position sensors, voice coil actuators and parasitic springs. The IP legs bolt on a rigid platform which rests on the existing horizontal cross beam tubes.

2.3 Vertical Stage

The vertical stage of HAM-SAS consist of the Spring Box. Inside of it, four GAS filters are held rigidly together to support the load of the optics table and to provide

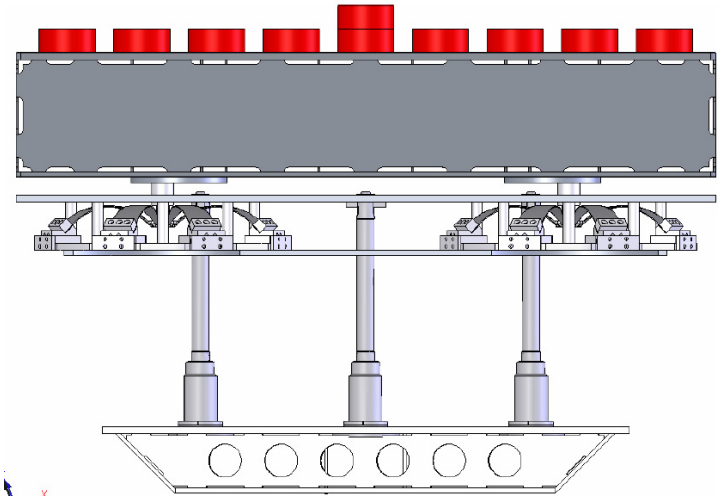

Figure 2.3: HAM-SAS assembly. From bottom to top: base plate, IP legs, spring box with GAS filters, optics table. The red weights on top represent the actual payload.

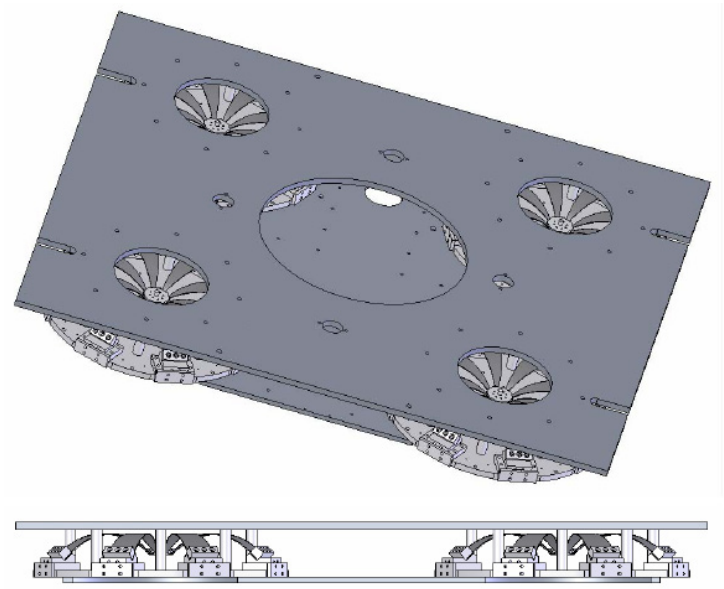

Figure 2.4: Spring Box assembly.

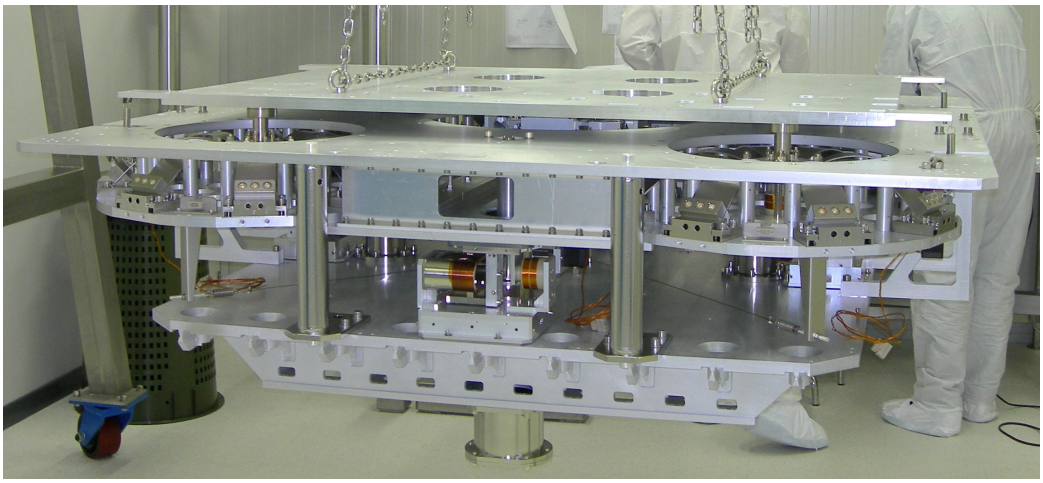

Figure 2.5: HAM-SAS still in the clean romm at the production site before the baking process. The spring box is tight to the base plate by stainless stell columns. The top plate is bolt to the spring box for the transfer.

the vertical seismic isolation. The interface between the optical table and the GAS filters is an aluminum plate with four stainless steel pins sticking down from the corners, each with a particularly shaped bottom mating surface, according to a scheme of the distribution and positioning of the load known as *quasi-kinematic mount*. Two opposite ones are simple cylinders with a flat bottom surface, the other two have one conical hollow and a narrow V-slot respectively. Each of the GAS filter culminates in a threaded rod having a hardened ball bearing sphere embedded at the top. The quasi-kinematic configuration is such that the table's pins mate to the filters' spheres thus precisely positioning the table while avoiding to over-constrain it . The contact point between the spheres and the surfaces let the table free to tilt about the horizontal axis.

2.3.1 The GAS filter

The GAS filter (fig. 2.6) consists of a set of radially-arranged cantilever springs, clamped at the base to a common frame ring and opposing each other via a central disk or keystone. The blades are flat when manufactured and under load bend like a fishing rod. We used modified Monolithic GAS (MGAS) filters [12]. As the MGAS the tips of the crown of blades are rigidly connected to the central disk supporting the payload. Instead of being made by a large, single sheet of bent maraging, we bolted the tips of independent blades to a central "keystone". Being built of different parts the spring is not, strictly speaking, "monolithic", but it shares all the performance improvements of the monolithic spring. For

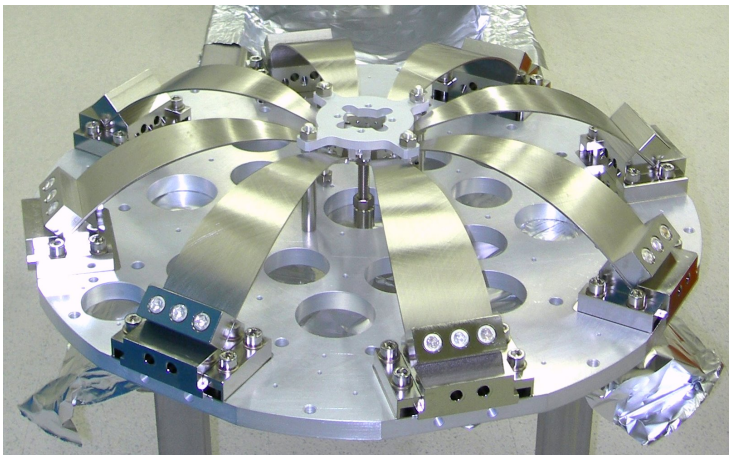

Figure 2.6: HAM-SAS GAS filter.

simplicity, throughout the text, we referred to them as GAS filters even if they would more properly be referred to as MGAS. The modified configuration has several advantages:

- blades can be cut using much more efficiently the sheet of expensive maraging metal.
- the number and width of blades can be changed arbitrarily (as long as 180^o symmetry is maintained) to match the required payload.
- the individual blades are perfectly flat and relatively small, thus their thickness can be easily tuned to the desired value by simply grinding them to thickness.
- for assembly the keystone is simply held at the center of the filter body with a temporary holder disk, then blades can be bent and assembled in pairs, avoiding the awkwardness of bending of, and keeping bent, all blades at the same time.
- the keystone, being a separate mechanical part, can be precision machined to directly host the LVDT and actuator coils, the threaded stud supporting the bench and the magic wand tips.

The blades are made starting from precision ground 3.44 mm thick *maraging steel* [13]. The choice of the material is made to guarantee a high Young modulus, non-deformability and thermal stability. The clamp radial positioning can be-adjusted to change the blades' radial compression by means of removable radial screws.

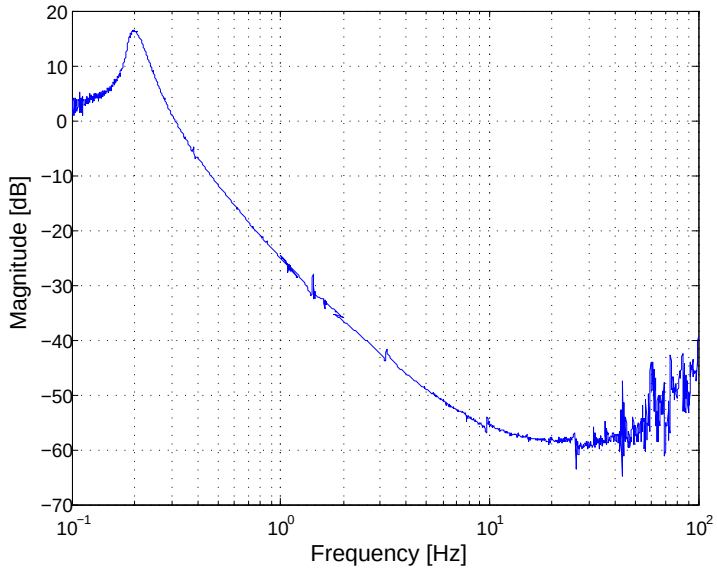

Figure 2.7: GAS filter transmissibility measured at Caltech in 2005 on a three blade, 3mm thick bench prototype [14]

At frequencies lower than a critical value the GAS filter's vertical transmissibility[1] from ground to the payload has the typical shape of a simple second order filter's transfer function (2.7). The amplitude plot is unitary at low frequencies, then has a resonance peak then followed by a trend inversely proportional to the square of the frequency. Above a critical frequency the amplitude stops decreasing and plateaus. This high frequency saturation effect is due to the distributed mass of the blades; the transmissibility of a compound pendulum has the same features.

A typical GAS filter can achieve -60 dB of vertical attenuation in its simple configuration, this performance can be improved to -80 dB with the application of a device called "Magic Wand" (see sec.2.3.6).

An effective low frequency transmissibility for the GAS filter is[2]

$$H_z(\omega) = \frac{\omega_0^2(1 + i\phi) + \beta\omega^2}{\omega_0^2(1 + i\phi) + \omega^2}\,, \tag{2.1}$$

[1] In Linear Time Invariant systems, the so called transfer function $H(s)$ relates the Laplace transform of the input $i(s)$ and the output $o(s)$ of a system, i.e. $o(s) = H(s)i(s)$ or $o(s)/i(s) = H(s)$. The transmissibility, a dimensionless transfer function where the input and the output are the same type of dynamics variables (position, velocity, or acceleration), is therefore the appropriate quantity to use when measuring the attenuation performance of a mechanical filter.

[2] Since the GAS filter is designed to work under vacuum the viscous damping term has been neglected.

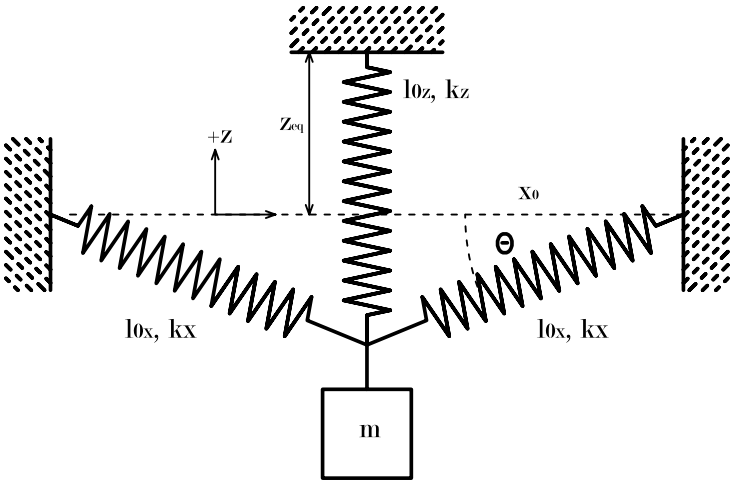

Figure 2.8: GAS Springs Model

where ω_0^2 is the angular frequency of the vertical resonance, ϕ the loss angle accounting for the blades' structural/hysteretic damping and β is a function of the mass distribution of the blades.

A simple way to model the GAS filter is to represent the payload of mass m_0 suspended by a vertical spring of elastic constant k_z and rest length l_{0z} and by two horizontal springs opposing each other of constant k_x and rest length l_{0x} (fig.2.8). The angle made by the horizontal springs is θ and it is zero at the equilibrium point when the elongations of the springs are z_{eq} and x_0 for the vertical and the horizontal respectively. The equation of motion for the system is then:

$$m\ddot{z} = k_z(z_{eq} - z - l_{0z}) - k_x(l_x - l_{0x})\sin\theta - mg \tag{2.2}$$

where $l_x = \sqrt{x_0^2 + z^2}$ is the length of the horizontal spring. Approximating $\sin\theta$ to z/x_0 for small angles (2.2) reduces to

$$m\ddot{z} = k_z(z_{eq} - z - l_{0z}) - k_x\left(1 - \frac{l_{0x}}{x_0}\right)z - mg. \tag{2.3}$$

We can see that at the first order the system behaves like a linear harmonic oscillator with effective spring constant

$$k_{eff} = k_z + k_x - \frac{k_x l_{0x}}{x_0}. \tag{2.4}$$

The last term of (2.4) is referred as the *Geometric Anti-Spring* contribute because it introduces a negative spring constant into the system. As consequence of it the effective stiffness is reduced, and so the resonant frequency, by just compressing

the horizontal springs. The system's response is then that of a second order low pass filter with a very low resonance frequency of the order of 0.1 Hz. Compared with an equivalent spring with the same frequency, it is much more compact and with motion limited to only one direction.

2.3.2 Equilibrium point position to load dependence

According to this model, at the equilibrium point the vertical spring holds alone the payload and we have that

$$z_{eq} = \frac{m_0 g}{k_z} + l_{0z} \tag{2.5}$$

from which the equation of motion becomes

$$m\ddot{z} = k_z\left(\frac{m_0 g}{k_z} - z\right) - k_x z - k_x l_{0x}\frac{z}{\sqrt{x_0^2 + z^2}} - mg. \tag{2.6}$$

We can find how, in the small angle approximation, the position of the equilibrium point changes in correspondence of a variation of the payload's mass when $m = m_0 + \delta m$ in the equation of motion (2.6). We obtain:

$$\delta m = -\frac{k_z + k_x}{g} z + \frac{k_x l_{0x}}{g}\frac{z}{\sqrt{x_0^2 + z^2}}. \tag{2.7}$$

Defining the compression as

$$\frac{l_{0x} - x_0}{l_{0x}} \tag{2.8}$$

we have that the position of the equilibrium point changes for different values of compression as in fig.2.9. As shown in the model, above a critical value of the compression the system has three equilibrium points in correspondence of the same payload, two are stable and one unstable. In this condition we say that the system is bi-stable. This implies that in case of very low frequency tuning of the GAS filter one has to avoid that the dynamic range of the system does not include multiple equilibrium points in order to avoid bi-stability[3].

[3]The optimal tune of the filter is very close to this critical compression value (at the critical point the recalling force of the spring and its mechanical noise transmission is null), but bi-stability cannot be tolerated.

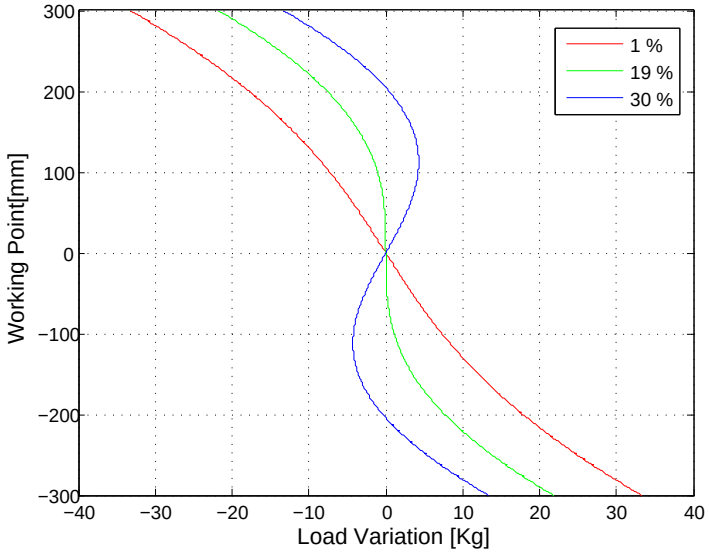

Figure 2.9: Equilibrium Point displacement for a variation of the payload's mass in correspondence of several compressions. The compression ratio in the legend is defined as $(l_{0x} - x_0)/(l_{0x})$.

2.3.3 Resonant frequency to load variation

Linearizing (2.6) it is possible to define the effective spring constant of the system correspondent to a change in the payload's mass as the derivative of the total force applied to it as evaluated at the equilibrium point:

$$k_{eff}(z) = -\left(\frac{\partial f}{\partial z}\right) = k_z + k_x\left(1 - \frac{l_{0x}x_0^2}{(x_0^2 + z^2)^{3/2}}\right) \tag{2.9}$$

where f is equal to the right side of 2.6. The plot on fig.2.10 shows the effect of the bi-stability as negative values of the square of the resonant frequency when the compression exceeds the critical value.

It is possible to extract the relation between resonant frequency and working point position when $m = \delta m + m_0$ is evaluated at the equilibrium point (fig.2.11) obtaining:

$$\omega = \sqrt{\frac{k_{eff}}{m}} = \left[\frac{k_z - k_x\left(\frac{l_{0x}x_0^2}{(x_0^2+z^2)^{3/2}} - 1\right)}{m_0 - \frac{z}{g}\left(k_x + k_z - \frac{k_x l_{0x}}{\sqrt{x_0^2+z^2}}\right)}\right]^{1/2}. \tag{2.10}$$

Plot 2.11 shows the frequency as a function of the equilibrium point. The curves corresponding to different compressions of the blades tend asymptotically to the

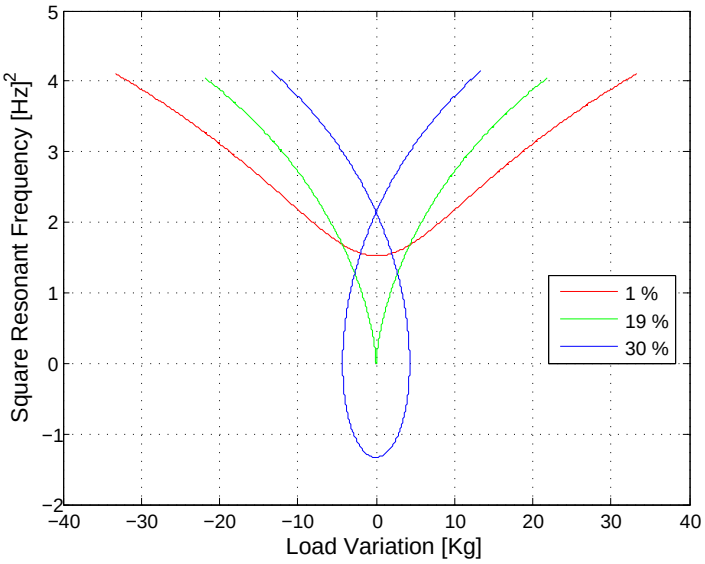

Figure 2.10: Dependence of the squared resonant frequency to the variation of the payload's mass at the equilibrium point.

straight lines forming a sharp V for values of the compression closer to the critical and also the minimum for each compression slowly changes position.

2.3.4 Thermal Stability

Once the compression and the payload is fixed, the system can be regarded as a soft linear spring which supports the payload. The thermal stability of the GAS can be studied under this approximation, valid in a small range around the working position [23]. In the GAS at the equilibrium, the entire vertical force of the system comes from the elasticity of the blade, and the working (equilibrium) position is determined by a balance of the stiffness and the payload weight. From the equation (2.4), the variation of the effective spring for a given perturbation of the temperature ΔT is

$$\Delta k_{eff} = \Delta k_z + \left(1 - \frac{l_{0x}}{x_0}\right)\Delta k_x - \frac{k_x}{x_0}\Delta l_0 + \frac{k_x l_{0x}}{x_0^2}\Delta x_0 \tag{2.11}$$

in which we can separate the contribution of the physical expansion of the blades and the frame ring from the change on the elasticity due to the temperature dependence of the Young modulus E as in the following:

$$\Delta k_{eff} = \left\{\left[k_z + \left(1 - \frac{l_{0x}}{x_0}\right)k_x\right]\frac{\delta E_{blade}}{E} - \frac{k_x}{x_0}l_{0x}\left(\delta L_{blade} - \delta L_{frame}\right)\right\}\Delta T. \tag{2.12}$$

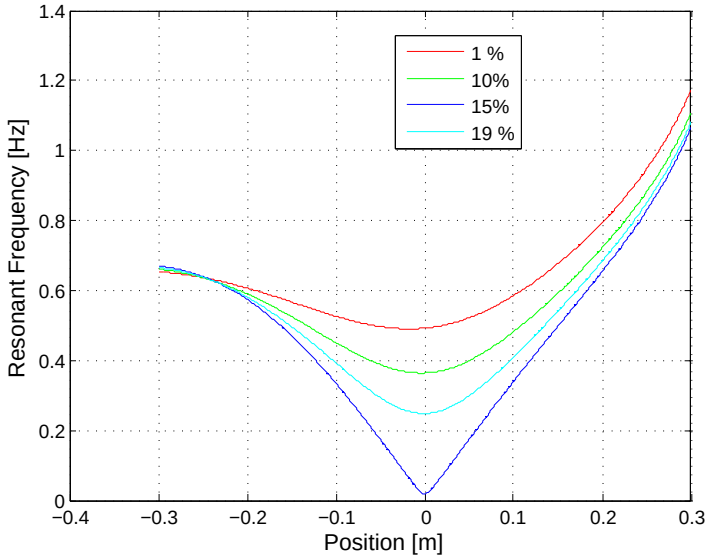

Figure 2.11: Resonant frequency to equilibrium position for several values of compression. The minimum moves from the original position.

The geometrical contribution depends on the differential thermal expansion coefficient of the blade and the frame (filter body). Assuming the use of maraging steel for the blade, and of aluminum for the frame, the difference of their expansion coefficients will be of order of 10^{-6}.

$$\Delta k_{eff} = \left[k_{eff} \left(\frac{\delta E}{E} \right)_{blade} - \frac{k_x}{x_0} l_{0x} \left(\delta L_{blade} - \delta l_{frame} \right) \right] \Delta T. \tag{2.13}$$

In the case of HAM-SAS, the relative variation of the Young modulus of maraging steel for a Kelvin degree is about 3×10^{-4}, the effective elastic constant of the four filters in parallel for a mass of about 1 ton and a resonant frequency of 200 mHz is $1.6 \times 10^3 N/m$. By assuming 9.0% of compression and substituting the parameters used in the plots above and the properties of maraging steel, one obtains the following formula to estimate the variation of the effective spring constant:

$$\Delta k_{eff} = -\left[(0.5)_{elasticity} + \left(10^{-3} \right)_{expansion} \right] \Delta T \quad [N/m]. \tag{2.14}$$

From the previous we can estimate the change in mass necessary to keep at the same height the working point of the GAS filter as:

$$\Delta m = \left(\frac{\Delta k_{eff}}{k_{eff}} \right) M \Delta T \tag{2.15}$$

which turns out to be very useful to evaluate the environmental condition in which the actuators have sufficient authority to compensate for the temperature variations.

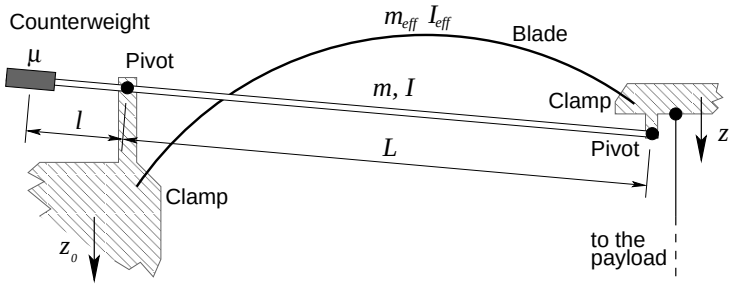

Figure 2.12: Rigid body representation of the GAS filter with a COP compensation wand. For sake of simplicity just one blade and one wand are sketched. Because of its distributed mass, the low frequency blade's dynamics can be approximated with a rigid body with effective mass and moment of inertia rotating about an horizontal axis. A wand with a counterweight connected as shown in the figure, provides a way of properly tune the center of percussion and remove the transmissibility saturation.

It is important to note that although the thermal sensitivity grows rapidly as the resonant frequency is brought near zero, the correction authority requirement is independent of the frequency tune of the filter.

The GAS effect only reduces the elastic return forces, but cannot affect the hysteresis forces. As the critical compression level is approached, the hysteresis takes a progressively dominating role. From the static point of view, just prior to bistability, hysteresis makes the oscillator indifferent. From the dynamical point of view hysteresis can turn the $1/f^2$ GAS filter TF behavior into a less favorable $1/f$ [34].

2.3.5 Quality Factor to Frequency Dependence

From equation 2.4 we can deduce the dependence of the Q factor of the GAS oscillator associating loss angles ϕ to each of the spring constants of our model and to the overall effective constant. We can then write:

$$k_{eff} = \tilde{k}_z\,(1 + i\phi_z)\left(1 - \frac{l_{0x}}{x_0}\right) + \tilde{k}_x\,(1 + i\phi_x) = \tilde{k}_{\text{eff}}\,(1 + i\phi_{\text{eff}}) \tag{2.16}$$

where the tildes mark the real part of the quantities. From the previous it follows that:

$$\phi_{\text{eff}} = \frac{\tilde{k}_z\phi_z\,(1 - l_{0x}/x_0) + \tilde{k}_x\phi_x}{\tilde{k}_{\text{eff}}}. \tag{2.17}$$

Considering that $\tilde{k}_{\text{eff}} = \tilde{k}_z\,(1 - l_{0x}/x_0) + \tilde{k}_x = M\omega^2$ and that $Q = 1/\phi$ we have:

$$Q = \frac{\omega^2}{\omega^2 - c} Q_z. \tag{2.18}$$

From 2.18 it follows that in the low frequency limit for $\omega \to 0$ it is $Q \propto \omega^2$. This implies that for very low frequency of tuning the Q drops naturally for histeretic causes and no damping is necessary [53].

2.3.6 The "Magic Wands"

The term β in (2.1) that limits the attenuation of GAS filters at high frequencies originates by the mass distribution in the blades and can be eliminated by the Center Of Percussion correction. The COP and its effect can be exemplified by a compound pendulum constrained to move in the horizontal direction. When the suspension point is forced to oscillate, in the high frequency limit, the pendulum body pivots around a fixed point, which is the COP. In the same way, if an impulsive force is applied along the COP the suspension point remains fixed.

A solution has been designed [15], [14] and it consists of a device that is mounted in parallel to the GAS springs. It consists essentially of a wand hinged to the filter frame ring and the central keystone. Attached to one end is a counterweight whose function is to move the wand's COP out of the pivot.

A reasonably accurate dynamical description of the system, which accounts for the internal vibrational modes, can be obtained simply by considering the curved blades as an elastic structure. However the low frequency dynamics and the transmissibility saturation of the GAS filter with the wand can be easily and accurately described in the rigid body approximation (see figure 2.12). In this regime, the blade is represented as a vertical spring of spring constant k_z; its distributed mass is an effective rigid body with mass m_{eff}, horizontal principal moment of inertia I_{eff}, with center of mass at distance l_{eff} from the wand's pivot. The wand is modeled as a hollow cylinder of lenght d, moment of inertia I and mass m, with a point-like counterweight of mass μ at one end. The distances along the wand from the pivot to the counterweight and to the wand's tip are respectively l and L. The payload can be simply modeled with a point-like mass M. Under these assumptions, the Lagrangian for small oscillations of the system is

$$\begin{aligned} \mathcal{L} \;=\; & \frac{1}{2}M\dot{z}^2 + \frac{1}{2}\mu\left(\frac{l}{L}\dot{z} - \frac{L+l}{L}\dot{z}_0\right)^2 + \\ & \frac{1}{2}m_{eff}\left(\frac{l_{eff}}{L}\dot{z} - \frac{L-l_{eff}}{L}\dot{z}_0\right)^2 + \frac{I_{eff}}{2L^2}(\dot{z}-\dot{z}_0)^2 + \\ & \frac{1}{2}m\left(\frac{2L-d}{2L}\dot{z} + \frac{d}{2L}\dot{z}_0\right)^2 + \frac{I}{2L^2}(\dot{z}-\dot{z}_0)^2 - \\ & \frac{1}{2}k(z-z_0)^2 \end{aligned} \tag{2.19}$$

where z is the generalized coordinate orthogonal to the constraints necessary to

describe the system's dynamics, and z_0 is the coordinate of the suspension point. The spring constant k is complex and can be rewritten as $k = k_z(1 + i\phi)$ where the term ϕ and k are both real and have been introduced ad hoc to account for the structural damping, which is the dominant dissipation mechanism of the blades. The gravitational potentials have not been included because they only fix the equilibrium position of the system and do not affect the dynamical solution.

Computing the Euler-Lagrange equation and solving it in the frequency domain, we obtain the vertical transmissibility $H_z(\omega)$ of the mechanical system:

$$H_z(\omega) = \frac{\tilde{z}(\omega)}{\tilde{z}_0(\omega)} = \frac{\omega_0^2 - A\omega^2}{\omega_0^2 - B\omega^2}$$

in which:

$$\begin{aligned}
A &= \frac{d^2}{4L^2} - \frac{d}{2L} + \frac{I_{eff}}{mL^2} + \frac{I}{mL^2} - \frac{m_{eff} l_{eff}}{mL} + \frac{m_{eff} l_{eff}^2}{mL^2} + \frac{\mu l^2}{mL^2} + \frac{\mu l}{mL} \\
B &= 1 + \frac{M}{m} + \frac{d^2}{4L^2} - \frac{d}{L} + \frac{I_{eff}}{mL^2} + \frac{I}{mL^2} + \frac{m_{eff} l_{eff}^2}{mL^2} + \frac{\mu l^2}{mL^2} \\
\omega_0^2 &= \frac{k_z\,(1 + i\phi)}{m}
\end{aligned}$$

From (2.20) it follows that, in the limit $\omega \to \infty$, $H(w) \to A/B$ and a plateau appears in the transmissibility at high frequency. In principle it can be canceled reducing A to zero by tuning the counterweight's moment of inertia μl^2. When $A \neq 0$, because μl^2 is either too small or too large, a complex conjugate zero pair appears in the transfer function and we say the system is under- or over-compensated respectively. Ideally neglecting the internal modes and setting the system at the transition between under-compensation and overcompensation, a well-tuned wand should be able to restore the theoretical $1/\omega^2$ trend at the high frequencies [15].

2.3.7 Vertical Modes of the System

The HAM-SAS' vertical degrees of freedom can be simply modeled by a table held by four vertical springs. Each of them represents a GAS filter with an equal effective spring constant k_1, k_2, k_3, k_4 and has null rest lengths. Let the tern (z, θ, ϕ) represent the coordinates of the system, M the total mass of the table, I_θ and I_ϕ the momentums of inertia of the table along the x axis and the y axis respectively, and l the table's half length. We can deduce the equation of motion from the Lagrangian of the system $\mathcal{L} = T - U$ in which the kinetic and the potential energy

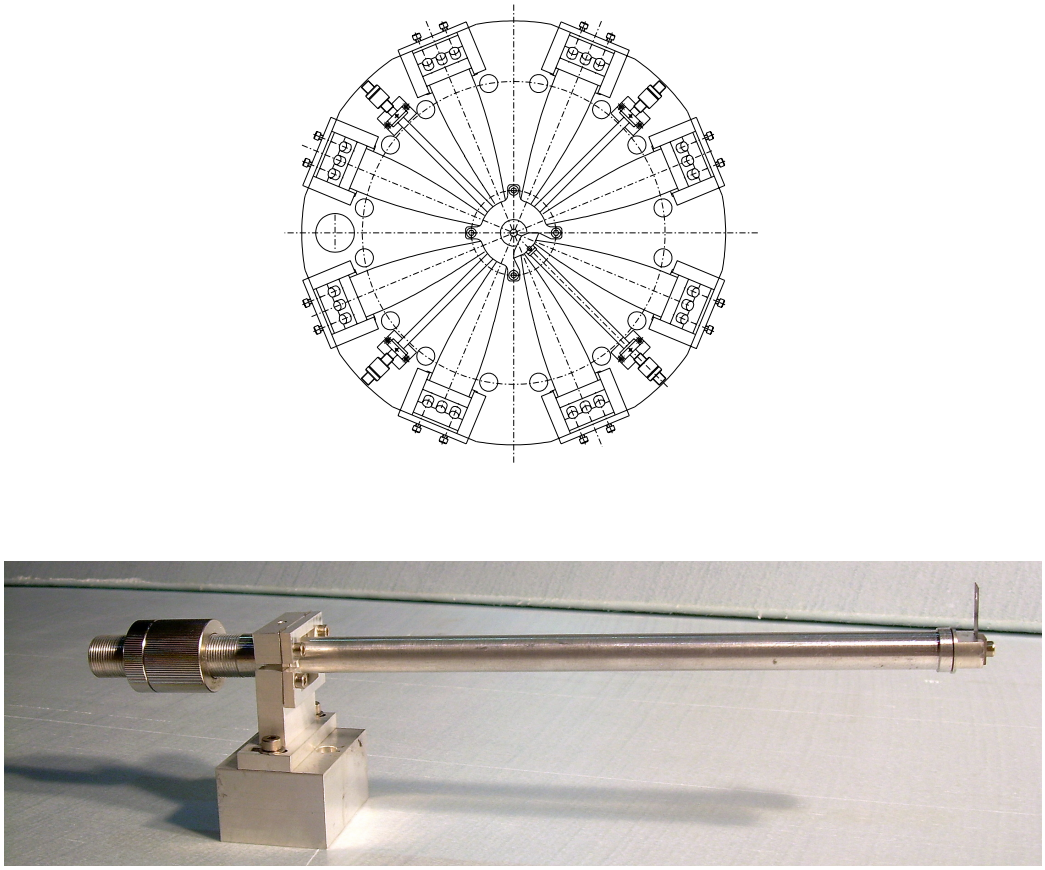

Figure 2.13: "Magic Wand" designed for HAM-SAS. Presently not yet installed in the system. They can provide an additional order of magnitude in vertical attenuation.

can be written as:

$$2T = M\dot{z}^2 + I_x\dot{\theta}^2 + I_y\dot{\phi}^2 \tag{2.20}$$

$$2U = k_1 z_1^2 + k_2 z_2^2 + k_3 z_3^2 + k_4 z_4^2. \tag{2.21}$$

z_i are the elongations of the springs and can be written in terms of the coordinate of the system as:

$$z_1 = z - l\theta - l\phi \tag{2.22}$$

$$z_2 = z + l\theta - l\phi \tag{2.23}$$

$$z_3 = z + l\theta + l\phi \tag{2.24}$$

$$z_4 = z - l\theta + l\phi. \tag{2.25}$$

Solving the equations of Eulero-Lagrange for the system we can write:

$$[M]\,\ddot{\mathbf{x}} = \mathbf{K}\mathbf{x} \tag{2.26}$$

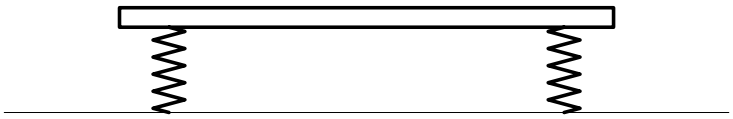

Figure 2.14: Dynamical model of the optics table.

where **x** represents the vector of the coordinates, $[M]$ represents the inertia and **K** is the stiffness matrix of the system:

$$K = \begin{pmatrix} k_1 + k_2 + k_3 + k_4 & \frac{l}{2}(-k_1 + k_2 + k_3 - k_4) & \frac{l}{2}(-k_1 + k_2 + k_3 + k_4) \\ \frac{l}{2}(-k_1 + k_2 + k_3 - k_4) & l^2(k_1 + k_2 + k_3 + k_4) & \frac{l}{2}(k_1 - k_2 + k_3 - k_4) \\ \frac{l}{2}(-k_1 + k_2 + k_3 + k_4) & \frac{l}{2}(k_1 - k_2 + k_3 - k_4) & l^2(k_1 + k_2 + k_3 + k_4) \end{pmatrix}. \tag{2.27}$$

From 2.27 the modes of the system correspond to the eigenvectors of K:

$$K\xi = \lambda\xi \tag{2.28}$$

and the correspondent frequencies can be obtained from the relative eigenvalues:

$$\omega_{0i}^2 = \frac{\lambda_i}{M_i}. \tag{2.29}$$

In the simple case in which the four spring constants are equal to each other the eigenfrequencies are:

$$\omega_z = \left(\frac{4k}{M}\right)^{1/2}; \quad \omega_x = \left(\frac{2kl^2}{I_x}\right)^{1/2}; \quad \omega_y = \left(\frac{2kl^2}{I_y}\right)^{1/2}. \tag{2.30}$$

From (2.30) we can see that the two angular frequencies depend on the system's momentums of inertia and the two modes are degenerate in case of symmetry.

2.3.8 Tilt stabilizing springs

In general the table will not rest horizontally because of torques originated by the weight distributions and differences in the spring constants. Unlike the BSC case, in the HAM chambers the load is located above the seismic attenuation stage and the effective tilt rotation axis. This torque is in competition with the stabilizing component of the GAS springs. The GAS springs, though, are tuned to be very weak, therefore the destabilizing torque eventually dominates and would result in an unstable equilibrium. This problem was overseen in the initial design and simulations, and discovered during initial tests. To solve this problem a system of correcting springs has been introduced in the design of HAM-SAS in order to add stiffness on the angular DOFs (see fig. 2.15). A vertical shaft was connected

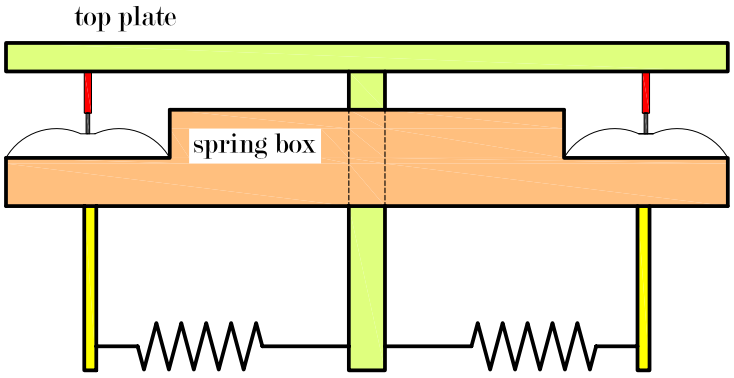

Figure 2.15: Scheme of the tilt correcting springs added between the top plate and the spring box.

to the underside of the top plate, attaching a cross of four springs connected to the four corners of the spring box. The four springs hook to four wires and four tuning screws to reach the spring box corners and allow fine tilt tuning.

The four tilt correcting springs work inevitably as a spring in parallel to the GAS springs and add stiffness in the vertical degree of freedom as well. The spring constant of this effective vertical parallel spring is

$$k_{tilt}^{(z)} = 4\left(1 - \frac{l_0}{x_0}\right)k \tag{2.31}$$

where l_0 is the springs' rest length, x_0 the spring elongation at the working point and k their spring constant. $k_{tilt}^{(z)}$ can be made small keeping the working point length close to the rest length. Since the springs work in tension, x_0 cannot be reduced arbitrarily but has to be always greater than l_0 in all the dynamical range of the system.

The additional,and unwanted vertical stiffness can be cancelled by a small, in situ, correction compression of the GAS springs[4].

2.4 Horizontal Stage

The horizontal stage of HAM-SAS is based on four inverted pendulums that support the spring box. Each of them is constituted by an aluminum hollow cylinder, 448 mm long, 50 mm diameter and walls 1 mm thick hinged to the base plate by a maraging steel flex joint with diameter of 95 mm over the length of 50 mm[5]. This

[4] At this time, there has not been occasion for this fine adjustment yet.

[5] The angular elasticity of this flex joint was calculated to balance the inverted pendulum destabilization stiffness ($-Mgh$) for a mass of 250 kg per leg (1 ton total) over the 491 mm effective IP leg.

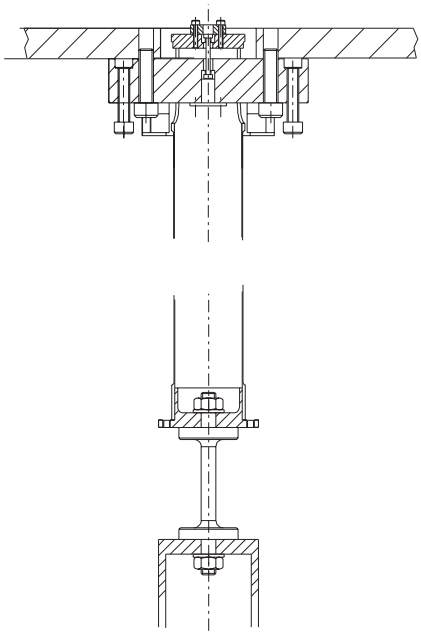

Figure 2.16: Supporting system for the spring box.

flex joint works in compression. The connection to of the Spring Box is obtained by mean of a particular mechanical system (fig.2.16). In correspondence of each attachment point the spring box is provided with a small steel bridge that hangs from a tensional flex joint made of a short maraging steel wire 30 mm long and 3 mm diameter. The wire hangs from the IP's leg cap. The bridge is provided with 4 screws, two pushing and two pulling from the spring box plate. This arrangement permits to tune the height of the attachment point of the leg and thus to compensate for spring box warping or differences on the leg's length and equally distribute the load between them (see section 3.3.1 for the process of tuning).

2.4.1 Inverted Pendulums

The inverted pendulums (IP) are designed to provide the seismic isolation along the horizontal directions. An IP is a compound pendulum hinged to the ground by a flex joint in such a way that the center of mass is above the pivot. The model represented in fig.2.17 illustrates how it works. M is the mass that has to be isolated from the ground and it is connected to a rigid leg with momentum of inertia I, mass m and length l by a flex joint producing an elastic force to which corresponds a complex spring constant $\kappa = \kappa_0(1 + i\phi)$, where the imaginary term is introduced to take into account the structural damping. With these parameters

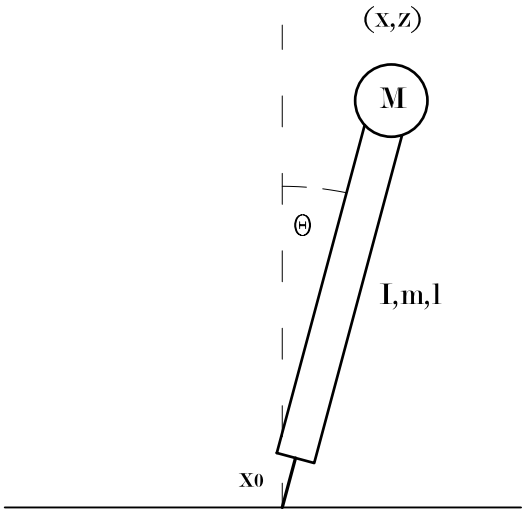

Figure 2.17: Inverted Pendulum Model

the equation of motion for the mass along the θ axis is then:

$$I\ddot{\theta} = -\kappa\theta + Mgl\sin\theta \tag{2.32}$$

which describes an harmonic oscillator with effective spring constant

$$\kappa_{eff} = \kappa - Mgl. \tag{2.33}$$

From (2.33) we can see that the gravitation term Mgl acts like an anti-spring and reduces the overall stiffness and thus the resonant frequency.

The physics of the system is well described by the potential energy:

$$U = \frac{1}{2}\kappa\theta^2 + Mgl(\cos\theta - 1) \backsimeq \frac{1}{-}\kappa_{eff}\theta^2 + Mgl\frac{\theta^4}{4!}O(\theta^6). \tag{2.34}$$

In the small angle approximation and for $\kappa > 0$ the quadratic term of the potential dominates and the system is a simple oscillator. By reducing the value of κ the potential "flattens" around $\theta = 0$ and this corresponds to small restoring forces and small resonant frequency. When $\kappa_{eff} \approx 0$ the quartic term dominates at small angles. When gravity begin dominate ($\kappa_{eff} \lesssim 0$, $\theta = 0$ is no more a point of stable equilibrium. $U(\theta)$ has two minima at

$$\theta = \pm\sqrt{12\frac{-\kappa_{eff}}{Mgl}}. \tag{2.35}$$

When $\kappa_{eff} \ll 0$ the potential is always negative and the system is unstable.

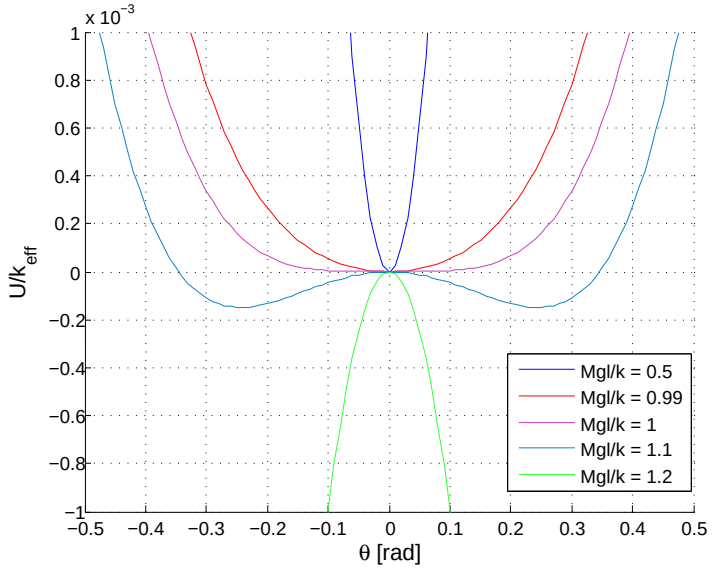

Figure 2.18: The reduced potential energy U_{pot}/κ is plotted for different values of the gravity elastic ratio $R_{ge} = Mgl/\kappa$. For $R \ll 1$ the system is far from instability; or $R \gtrsim 1$ the system becomes bi-stable; for $R \gg 1$ there is no stable equilibrium point and the system collapses.

Referring to the IP linear displacement x measured at its top ($x = l\theta$) and to the linear stiffness $k = \kappa/l^2$, the equation of motion for the variable x and in case of small displacements is:

$$M\ddot{x} = -\left(k - \frac{Mg}{l}\right)x + O(x^3) = k_{eff}x + O(x^3). \tag{2.36}$$

When $k_{eff} > 0$, the system is an oscillator resonating at frequency:

$$f_0 = \frac{1}{2\pi}\sqrt{\frac{k}{M} - \frac{g}{l}}. \tag{2.37}$$

In principle, by properly tuning the spring stiffness and the suspended load one can obtain arbitrarily resonant frequency.

We can describe the dynamical behavior of the IP in the frequency domain by the Lagrangian of the system:

$$\mathcal{L} = \frac{1}{2}Mv^2 + \frac{1}{2}I\dot{\theta}^2 + \frac{1}{2}mv_{cm}^2 - \frac{1}{2}kl^2\theta^2 - mhz_{cm} - Mgz \tag{2.38}$$

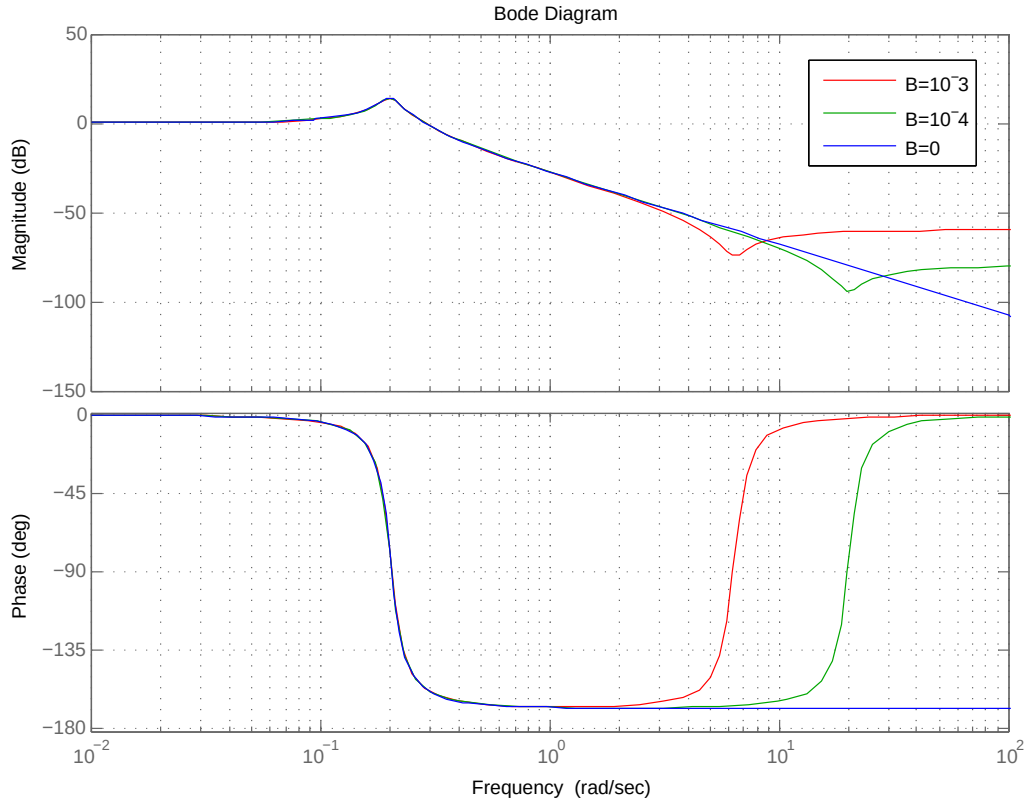

Figure 2.19: IP Transmissibility for different values of B/C.

from which we can obtain the transmissibility as following:

$$\frac{\tilde{x}(\omega)}{\tilde{x}_0(\omega)} = \frac{A + B\omega^2}{A - C\omega^2} \tag{2.39}$$

$$A = \left[4\omega_0^2 - 1 - \frac{2g}{l} - 4M - \frac{4M}{m} - \frac{4gM}{ml}\right] \tag{2.40}$$

$$B = \left[1 - 4\frac{I}{ml^2}\right] \tag{2.41}$$

$$C = \left[1 + 4\frac{I}{ml^2} + 4\frac{M}{m}\right]. \tag{2.42}$$

It is clear from (2.39) that the inverted pendulum acts as a second order low pass filter respect to the ground motion.

Similarly to the GAS filter case (see sec.2.3.6) the presence of the ω^2 term in the numerator of (2.39) introduces a plateau of the transmissibility at high frequencies and thus a saturation in the isolation performance. The effect arises because of the mismatch of the center of percussion with the hinging point. The way to

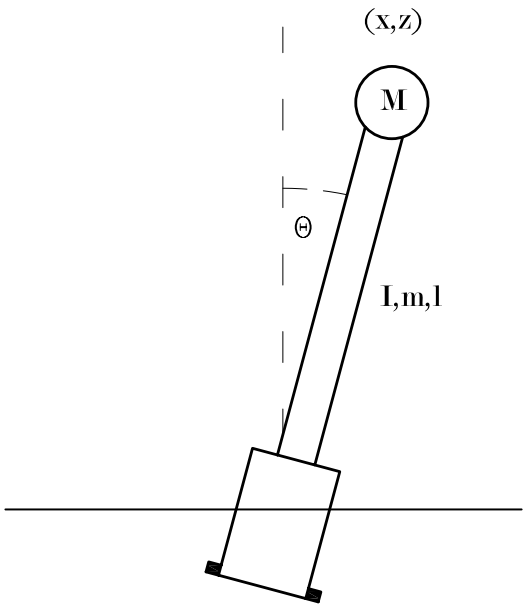

Figure 2.20: IP counterweight to compensate the COP effect.

overcome the limitation consists then in adding a counterweight to bring the COP to the ground level, that is to say canceling the term B in (2.39) [31].

The plateau level expected with the unbalanced 200 g legs is calculated to be at -80 dB. The implementation of the counterweight is expected to increase the attenuation power by 20 dB with just 90% compensation of the COP effect, a very simple balancing to obtain[6].

2.4.2 Response to Ground Tilt

When the ground tilts by and angle Θ with respect to the vertical axis, it simply introduces an additional external force $-k_\theta\Theta$ to the system. If this contribution is included by the equation of motion 2.39 we have:

$$x = \frac{A + B\omega^2}{A - C\omega^2}x_0 + \frac{k_\theta/l^2}{A - C\omega^2}\Theta \tag{2.43}$$

where k_θ/l^2 is the equivalent spring constant for the translational motion x.

With an IP perfectly tuned so that $\kappa_{\text{eff}} = 0$ ($\kappa = Mgl$), the spring box would respond like a mass on a perfectly friction-less flat table.

[6]For the HAM-SAS prototype a suitable counterweight was designed and built, but never put in operation for lack of time.

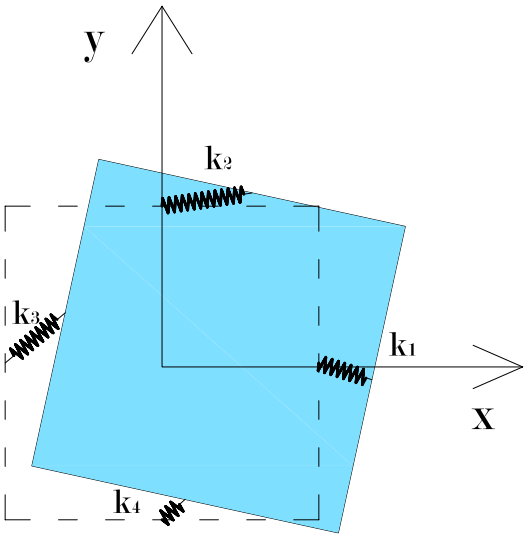

Figure 2.21: Dynamical model for the horizontal degrees of freedoom

2.4.3 Horizontal Normal Modes of the System

We can study the horizontal degrees of freedom with a simple model. The ensemble spring box plus optics table is regarded as a rigid body on the horizontal plane supported by four soft springs with constant $k_1, \ldots, k_4$ and null rest lengths (fig.2.21). According to this model the system has three normal modes resulting from the overimposition of two translations along the horizontal plane and one rotation around the vertical axis.

The motion of the rigid mody is defined by a vector containing the positions (x,y,ϕ) in a Cartesian system of coordinates. Considering the elementary displacements, one obtains the stiffness matrix of the system:

$$K = \begin{bmatrix} -k_1 - k_2 - k_3 - k_4 & 0 & -k_2 + k_4 \\ 0 & -k_1 - k_2 - k_3 - k_4 & -k_1 + k_3 \\ -k_2 + k_4 & -k_1 + k_3 & \text{-}k_1 - k_2 - k_3 - k_4 \end{bmatrix} \quad (2.44)$$

where the mass, the momentum of inertia and the radius of the rigid body are assumed as unity for simplicity. In the case in which $k_1 = k_3$ and $k_2 = k_4$ the normal modes coincide with two pure translations and a rotation.

2.5 Sensors and actuators

In HAM-SAS the spring box is mechanically constrained to movements in the horizontal plane (x-y and yaw) while the optical bench only moves in the remaining three degrees of freedom (z, pitch and roll) with respect to the spring box.

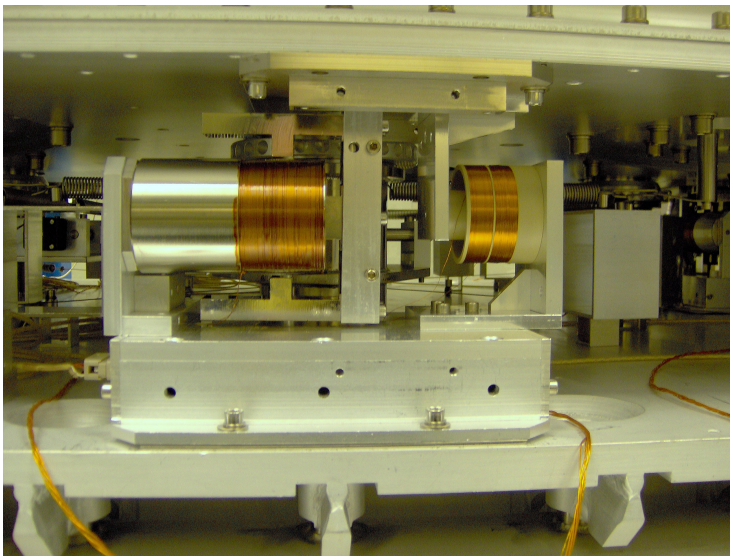

Figure 2.22: Horizontal coil actuator and LVDT.

The 6 by 6 positioning and control matrix then naturally and conveniently splits into two independent three degree-of-freedom matrices. Sensors and actuators are co-located to roughly diagonalize the controls within each of the three degree-of-freedom matrices.

Instrumentation for sensing and actuation is applied in groups of four, even if each system has only three degrees-of-freedom. This arrangement was chosen because of the rectangular symmetry of the vacuum chamber support feed-throughs and of the optical bench. Four instruments for three degrees of freedom form a redundant system, one of the instruments can be ignored, or three diagonalized virtual sensors can be synthesized from the four actual ones. The redundancy of the sensor/actuators also makes that if one of the instruments fails, the SAS can still operate normally, by simply changing the diagonalization matrix (The subject is extensively discussed in sec. 5.2).

An LVDT [33] (Linear Variable Differential Transformer) is constituted by three coaxial coils, two large ones wire in series, coiled in opposite direction, which are mounted on a reference structure and act as receiver and a smaller coil, which is the emitting coil, positioned between the larger two and fastened to the moving mechanical component. The central emitting coil is driven by a sinusoidal signal with frequency between 10 kHz and 20 kHz. The coils are made in Kapton-coated copper wire wound around a peek support. The clearance between the large coils was sufficient to allow 10 mm movements in all directions. The position measurement is obtained by measuring in a lock-in amplifier the amplitude and sign of the voltage generated in the receiving coils by the emitting coil. Ob-

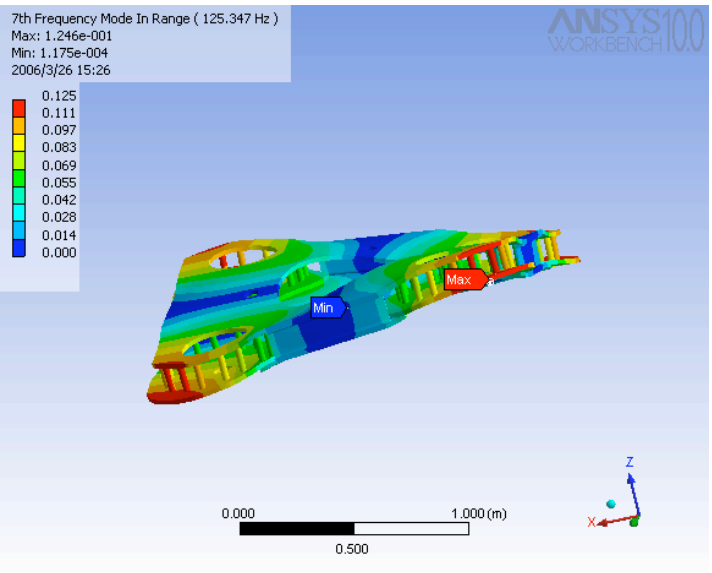

Figure 2.23: Simulations of the internal modes of the spring box brought to the introduction of later stiffenere into the structure.

viously the measured voltage depends on the magnetic coupling of the two coils and the right choice of the geometry permits a 1 percent linearity over a region of more than a few centimeters at low gain. At high gain the readout range is strongly reduced to improve the sensitivity to a nm. This resolution exceeds the stability of the floor and is deemed sufficient to satisfy the Ad-LIGO specs. Another important function of the LVDTs is to provide the position memory needed to bring the table back into the original alignment after interventions on the optics.

The horizontal-direction dynamic actuators are specially designed, noncontacting, "racetrack" voice coils (fig.2.22). The choice of wire diameter and of materials (kapton and peek) is made so that the coils can, in non condition, (included a railed power supply) over-heat and get damaged or, worse, pollute the vacuum system. The geometry of the "racetrack" and of the magnetic yoke are designed to deliver constant force within better than a percent over a field of movements of 10 mm in diameter in the horizontal plane. They deliver force sufficient to deal with tidal movements and thermal excursions of 10 K with less than a mW of maximum power dissipation. They are capable of positioning the table within the resolution of the LVDT position sensors.

The vertical direction dynamic actuators have similar performance, but more traditional design, non-contacting voice coils.

Micrometrically and remotely controlled stepper motors are used to null the static current of the dynamic actuators. This solution has multiple advantages. It

maintains alignment within a few microns even in the event of complete power loss, it makes in-vacuum power consumption practically negligible, and, by reducing the force requirements on the actuators to mN levels, it allows the use of very low authority drivers, thus minimizing their actuation noise.

2.6 Spring Box Stiffeners

Early simulations of the HAM SAS spring box showed that the spring box has undesirable low frequency resonances [11]. A study was carried out to find easy solutions to stiffen the table and mitigate the possible problem (fig.2.23).

It was noted how some modes had relatively large relative movements between the IP support points of the spring box and the GAS support points of the optical table. Two kinds of stiffeners, C-profile plates mounted at the periphery of the spring box, where they can be installed easily were tried. The result was that some frequencies actually decrease because of the added mass and some increase. The stiffeners were included in the design because it caused the most worrisome resonances to increase in frequency.

Chapter 3

Mechanical Setup and Systems Characterization

The two main subsystems of HAM-SAS are the GAS filters and the Inverted Pendulums. As discussed in the previous chapter, the firsts are responsible for the vertical degrees of freedom, the seconds control the horizontal ones. The overall performance of the system depends equally on the performance of each of the two parts, and on their mutual interactions. During the mechanical setup, we set each of them in its optimal configuration and then integrated the whole system. We assembled the GAS filters with the appropriate compression of the blades, tuned and equalized their resonant frequencies and working points. For the inverted pendulums we measured the spring constant of the flex joints and found the optimal load for the best horizontal seismic attenuation performance. We then installed the spring box with the GAS filters on the IPs, taking care of equally distributing the load on each leg. The mechanical setup continued with the system installed inside the HAM chamber at LASTI with the leveling of the optics table, the stabilization of the tilts and the final tunings.

3.1 GAS Filter Tuning

The GAS filters performs at best if tuned to the lowest possible frequency which still prevents them from becoming bi-stable[1]. As shown in 2.11, the resonant fre-

[1]This bench tuning is made mechanically, exciting the oscillations and measuring their ring-down. Because of damping approaching critical levels and hysteresis, it is impossible in this configuration to read the filter resonance at the lowest frequencies and tune the filters to lower levels. Also the tune may be slightly changed by the bake-out procedures, and the overall vertical stiffness may change when the four filters are assembled into the spring box and the tilt stabilization mechanism is implemented. Once fully installed, with full fledged sensing and actuation capabilities, a much more precise mechanical tune of the filters and the overall system is possible.

Frequency [mHz]	Height [mm]	Mass [Kg]
A	191	276.2
B	180	275.42
C	192	276.34
D	183	276.5

Table 3.1: GAS filter bench tuning.

quency of a stable filter has approximately a quadratic dependence on the height of the blades' tip and there is a point in which, fixed the compression, the frequency reaches a minimum. This is the vertical working point at which the GAS filter has to be set. The radial compression is varied seeking the minimum frequency achievable. The process of tuning consists in finding the critical compression and the appropriate mass to set the filter at the working point with the lowest frequency. The four filters must also be equalized. Figure 3.1 and table 3.1 show the results.

3.2 Tilt Correcting Springs

After the optics table had been installed on HAM-SAS, the mechanical setup continued with the solution of the tilt stability problem.

As explained in sec. 2.3.8, a tilt stabilization rod and auxiliary springs were included between the optical bench and the spring box to stabilize the tilt modes of the optics table. We have made a simplified calculation of the tilt-correction springs stiffness k required for the HAM-SAS optics table to float and make the tilt unconditionally stable considering the GAS springs as normal vertical springs[2].

In the small angle approximation we can write the destabilizing torque due to the optics table load as

$$\tau_{load} = \theta g \sum_i m_i z_i \simeq \theta \times 5466\ Nm \tag{3.1}$$

where θ is the angle between the table plane and the horizontal plane and m_i and z_i are the mass and the height of the i-th mass element with respect to the top edge of the springs, including the optics table. Z_i is calculated starting from the plane of the spherical joints on which the tilt movement hinges, just over the GAS spring keystones. Load moment calculations have been carried out with the Solid Work model of the system (fig.3.3).

[2]In a complete simulation the GAS should be considered as nonlinear spring to take into consideration the whole effect

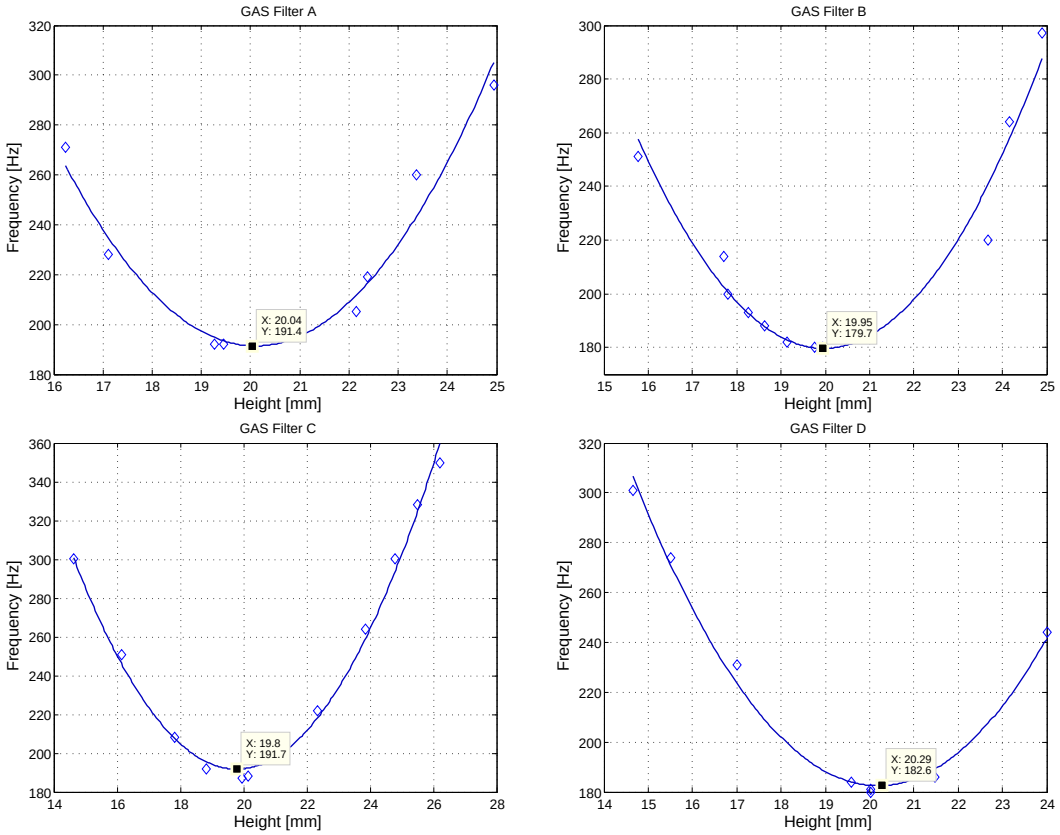

Figure 3.1: GAS filters Frequency vs Height experimental curves.

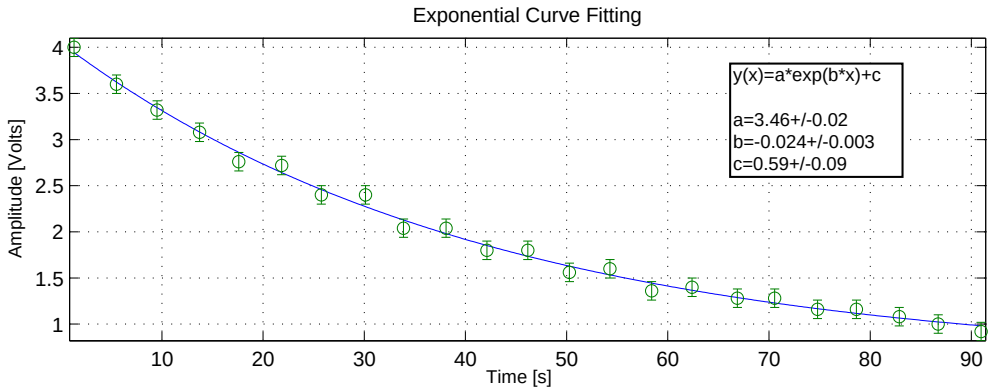

Figure 3.2: The plot shows the fit with an exponential decay for the oscillation amplitude of the GAS filter A of HAM-SAS tuned at 245 Hz. The result is a quality factor of about 42. It was believed to be quite an high value,after that measurement the compression was increased to reduce the frequency.

A compensating torque is introduced by the GAS and it is approximately equal to

$$\tau_{GAS} = 2k_{GAS}\theta l^2 \simeq \theta \times 464\ Nm \tag{3.2}$$

where

$$l^2 = \sqrt{Dx^2 + Dy^2}, \qquad k_{GAS} = \frac{16\pi^2 f_0^2}{M_{LOAD}}. \tag{3.3}$$

In the calculations we have assumed a resonance frequency $f_0 = 0.2$ Hz[3]. This stabilization force is negligible, and will tend to zero as the GAS resonance frequency is tuned towards zero. The force applied by the tilt-stabilizing springs is $F = kx$ with $x = \theta h$. The tilt stabilizing torque that it provides is proportional to h, the height of the tilt stabilization rod. The effect of the tilt-stabilizing springs can be written as

$$\tau = 2k\theta h^2 \simeq k\theta \times 0.151 Nm \tag{3.4}$$

where $h = 0.275$ m is the distance between the plane of tilt-correction springs and the assembly hinging point and k is the stiffness of the used springs[4].

In order to have a stable equilibrium position we need to have

$$\tau + \tau_{GAS} = \tau_{LOAD}. \tag{3.5}$$

Substituting in the expression we get

$$k \simeq 33100 N/m. \tag{3.6}$$

[3]This was the initial tune of the GAS filters, before bakeout.

[4]This is not necessarily the actual distance from the center of rotation.

Element	Mass (Pounds)	Mass (Kg)	Z (Inches)	Z (m)	Vertical Moment (kg m)	Dominant Material	Density (kg)	Volume (m^3)	Bouyant Mass (Kg)
Optical Table	841.00	378.45	0.00	0.00	0.00	Aluminium	2700.00	0.1402	0.1682
				0.00	0.00				0.0000
H1 Geophone	25.00	11.25	4.00	0.10	1.14	Mixed		0.0030	0.0036
H2 Geophone	25.00	11.25	4.00	0.10	1.14	Mixed		0.0030	0.0036
H3 Geophone	25.00	11.25	4.00	0.10	1.14	Mixed		0.0030	0.0036
V1 Geophone	25.00	11.25	5.00	0.13	1.43	Mixed		0.0031	0.0037
V2 Geophone	25.00	11.25	5.00	0.13	1.43	Mixed		0.0031	0.0037
V3 Geophone	25.00	11.25	5.00	0.13	1.43	Mixed		0.0031	0.0037
				0.00	0.00				0.0000
Triple_Suspended		9.00	32.52	0.83	7.43	Aluminium	2200.00	0.0041	0.0049
Triple_Non_Suspended		36.00	15.28	0.39	13.97	Aluminium	2700.00	0.0133	0.0160
									0.0000
Raised_Mass (Leg Element #1)	610.00	274.50	18.50	0.47	128.99	Stainless	8000.00	0.0343	0.0412
Mass_Riser		22.00	7.75	0.20	4.33	Stainless	8000.00	0.0028	0.0033
Leg Element #3	233.50	105.08	1.35	0.03	3.60	Stainless	8000.00	0.0131	0.0158
Clamp Risers		13.64		0.00	0.00	Stainless	8000.00	0.0017	0.0020
Counterweight		45.45		0.00	0.00	Stainless	8000.00	0.0057	0.0068
Optics Table Adaption Plate		112.00		0.00	0.00	Aluminium	2700.00	0.0415	0.0498
TOTAL		**1063.62**			**166.04**			**0.2748**	**0.3298**

Worst Case Table

Mass Element	Susp. Type	Susp. Mass	Sus. Height	Non Susp. Mass	Non Susp. Mass Height	Total Mass	Mass Moment
MC1	MC Triple	9	0.826	36	0.388	45	21.402
MC2	MC Triple	9	0.826	36	0.388	45	21.402
MMT3	RM Triple	38.3	0.796	40.4	0.537	78.7	52.1816
RM	MC Triple	9	0.826	36	0.388	45	21.402
Totals		65.3				213.7	116.3876
HAM SAS Initial							
BSC Leg Element 1				277	0.4699	277	130.1623
LOS Cage				22	0.19685	22	4.3307
Total					0.66675	299	134.493
HAM SAS Triple							
BSC Leg Element 1				277	0.4699	277	130.1623
LOS Cage				22	0.19685	22	4.3307
MC Triple	MC Triple	9	0.826	36	0.388	45	21.402
Total						344	155.895

Figure 3.3: Mass Properties of the HAM Table load as extracted from the Solid Works model. One shows the effective buoyant mass of the load on the GAS springs. The effective buoyant mass of the system is 0.32 kg. The second shows vertical moments in the worst case scenario for Advanced LIGO (i.e. HAM 2 with a stable signal recycling geometry).

Assuming an ideal zero GAS resonance frequency ($\tau_{GAS} = 0$) we get a slightly higher required stiffness

$$k \simeq 36150 N/m. \tag{3.7}$$

Note that four springs are mounted in a cross configuration. By symmetry two springs can always be considered orthogonal to any considered tilt, while the other two can be considered along the tilt. Therefore the effective stiffness in the tilt stabilization is twice the stiffness of a single spring, as long as the springs are under some tension.

The effect of the angular stiffness of the GAS springs was not considered in this initial calculation because the GAS springs support the optical table via spheres in groves that nominally do not transmit torque. This effect was then

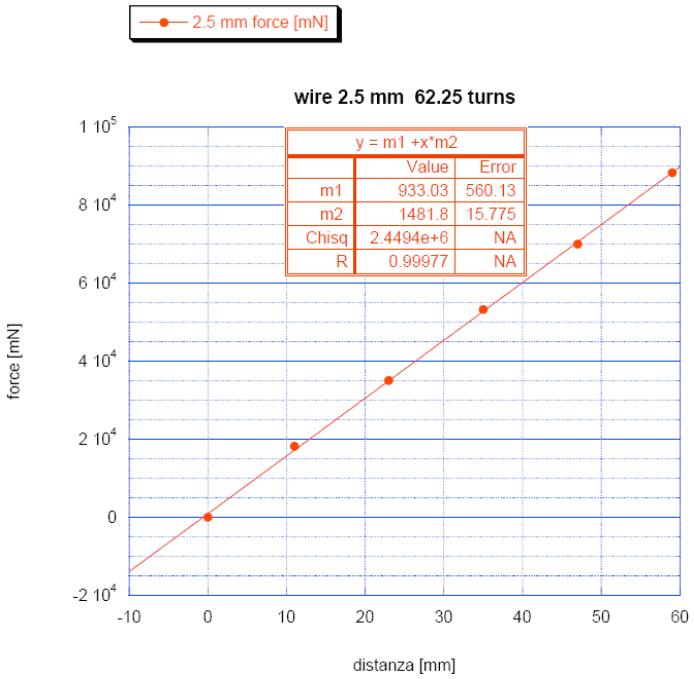

Figure 3.4: 2.5 mm wire spring stiffness measurement

calculated and added and resulted being non negligible [5].

To calculate the stiffness of a generic helical spring we can use the relation

$$k = \frac{Gd^4}{nD^3} \tag{3.8}$$

where d is the wire diameter, D is the average spring diameter, n is the winding number and G is a constant proportional to the material shear modulus. G was determined experimentally from a measurement of a spring.

Figures 3.4 and 3.5 show respectively the stiffness measurements for a spring, with $d = 2.5$ mm, $n = 20.75$ windings and for a spring with $d = 3$ mm and $n = 18$ windings. The average winding diameter was $D = 16.8$ mm for both springs. From the two measurements we get

$$G \simeq 1.26 \cdot 10^{10}\ N/m^2 \tag{3.9}$$

[5]The real problem came because when ordering the correction springs, we accidentally dropped a factor of ten from the calculation above and ordered softer springs. When we started the tuning we had available several sets of springs between 6,600 N/m (each) and 23,000 N/m. This mistake, composed with an unfortunate loose screw in the assembly of the tilt stabilization rod caused a lot of confusion.

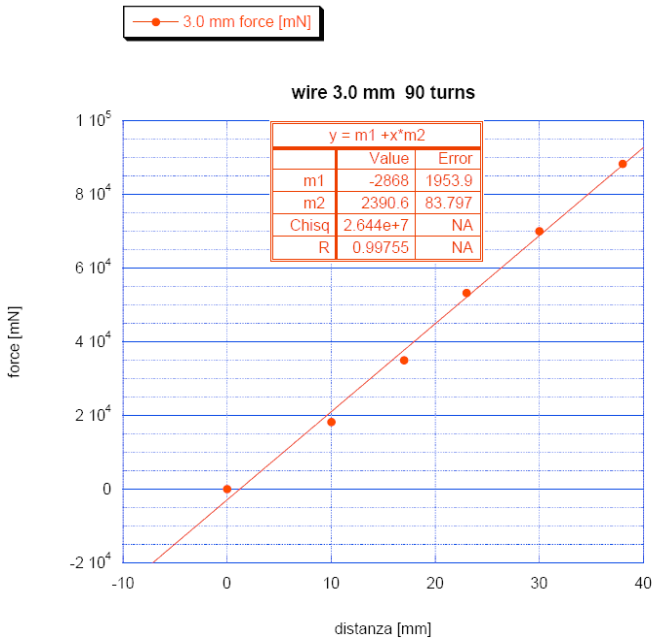

Figure 3.5: 3 mm wire spring stiffness measurement

In order to stabilize the table we initially used springs with d = 3.5 mm, n = 12 windings and D = 16.8 mm (k = 6600 N/m) which are clearly insufficient according to the calculation above and the bench was unstable. We then installed springs with d = 3.5 mm, n=8 windings, D = 16.8 mm (k = 10000 N/m), which was still insufficient to unconditionally stabilize the table. We had, in order

- springs with d = 4 mm and n = 12 windings, D = 16.8 mm (k = 11300 N/m)
- springs with d = 4 mm and n = 8 windings, D = 16.8 mm (k = 17000 N/m)
- springs with d = 4 mm and n = 6 windings, D = 16.8 mm (k = 23000 N/m).

Each of these is insufficient to guarantee unconditionate stability, but some intermittent stability was observed with the high spring value. The stability was due to the angular stiffness of the GAS filters neglected in the calculations, while the intermittent character of the stability was due to the loose tilt stabilization bar to which the stabilization springs are connected. This trivial problem motivated us to consider several possible causes of angular stability (or instability), discussed below. Only after wasting several days of time we found the source of the problem and fixed it by tightening the retaining screw. The system then became angularly stable, as expected. The reasoning has some importance and is reported below.

By this time we had remade the stiffness calculations and we knew that even the stiffest springs available were not sufficient. We conjectured correctly that the missing angular stiffness was contributed by the GAS springs angular stiffness, but the reason why we encountered only some angular stability at all might be in the friction in the spherical joints that couples in part of the GAS angular stiffness. We also considered the fact that the GAS springs are not linear and become stiffer as they stray away from the equilibrium point. This contribution turned out to be non relevant.

Simulations made with linear springs showed that if the spherical joints are eliminated, the table is perfectly stable with softer tilt correction springs, while if frictionless spherical joints are introduced, the table becomes angularly unstable[6].

Sufficient friction of the spherical joints but only as long as the sphere of the joint sticks to it siege. Evidently the that stick and slip in the joint this gave us the observed stability.

In order to answer the question, we went back to the lab and measured the torsional rigidity of GAS springs. We mounted a rigid lightweight carbon fiber shaft to a two blade GAS spring keystone. The blade is a close relative to the HAM-SAS'(a two blade version, in which we could measure independently the stiffness along and across the blades, with equal length blades, but 10% narrower and a few percents thinner than in HAM-SAS). The torque is applied at 600 mm from the keystone with a string, a pulley, and approximately 156 g masses. The torsional angle was measured on photos comparing the angle between the shaft and a ruler marks on the wall in the background. The measurement was made first along the blades, and then repeated transversally.

We found a longitudinal angular elastic constant for a pair of GAS blades equal to

$$k_\theta^l = (53 \pm 5) \text{ N/rad} \tag{3.10}$$

$$k_\theta^t = (72 \pm 5) \text{ N/rad.} \tag{3.11}$$

A GAS filter has four pairs of blades spaced at 45 degrees, therefore the angular elastic constant of a filter is

$$k_\theta = 2(53 + 72) = (394 \pm 10) \text{ N/rad} \tag{3.12}$$

that is for the whole spring box it would be $k_\theta = (1572 \pm 40)$Nm/rad. These numbers have to include a factor of *1.25* accounting for the different blade thickness (2.22 mm thick in the bench prototype, 2.39 mm in HAM-SAS) and *1.16* for the

[6]In the simulation the system is described with two bodies, the optics table and a massive base, and four springs with a diagonal stiffness matrix (10^8, 10^8, k_{GAS}) that connects the two bodies. The motion of the base respect to a generic inertial frame (ground) is not constrained.

blades width (80 instead of 69 mm). We also had to account for the number of blades in the filters. Then we have for the LASTI case:

$$\tilde{k}_\theta = (2280 \pm 40) \text{ N/rad.} \tag{3.13}$$

This torque represents roughly 40% of the torque necessary to stabilize the optics table tilt. The second possible source of stability may be that in GAS springs the resonant frequency is function of the distance x from the spring optimal working point (see fig.3.1):

$$f = a + bx^2. \tag{3.14}$$

We can write the elastic constant of an oscillator as $k = cf^2$, equating we get:

$$k = c_1^2 + 2c_1c_2x^2 + c_2^2x^4. \tag{3.15}$$

Then the potential energy of a GAS spring would lead also to higher than quadratic terms

$$U_{GAS} = k_{GAS}x^2 = c_1^2x^2 + 2c_1c_2x^4 + c_2^2x^6 \tag{3.16}$$

which may contribute to the stability. This contribution will not eliminate the need for the stabilization bar.

3.3 IP setup

The IPs are made of four allow aluminum tubes 0.491 mm long and 1 mm thick. They are supported by 8 mm thick, 50 mm long maraging steel cylindrical flex joints through an apposite holding cup. This flex joint (working under compression) provides the mechanical angular stiffness of the IP mechanism. A thin, negligible stiffness flex joint, working under tension, connects the head of each IP leg to the spring box. The IP setup required: the equalization of the load between the four legs;; the measurement of the resonant frequencies of the horizontal translational modes of the spring box and the correspondent load curve; the choice of the center of percussion correcting counterweight.

3.3.1 Load equalization on legs

Even though the parts involved in the IPs are machined to a high precision the UHV baking processing inevitably introduces some warping. We found the spring box to be more warped than the height tolerancies of the four legs. A new adjustable support system was then introduced to solve that problem.

The way we measured the individual leg load was measuring the frequency of the lowest rigid body mode of the legs. This corresponds to the “banana”

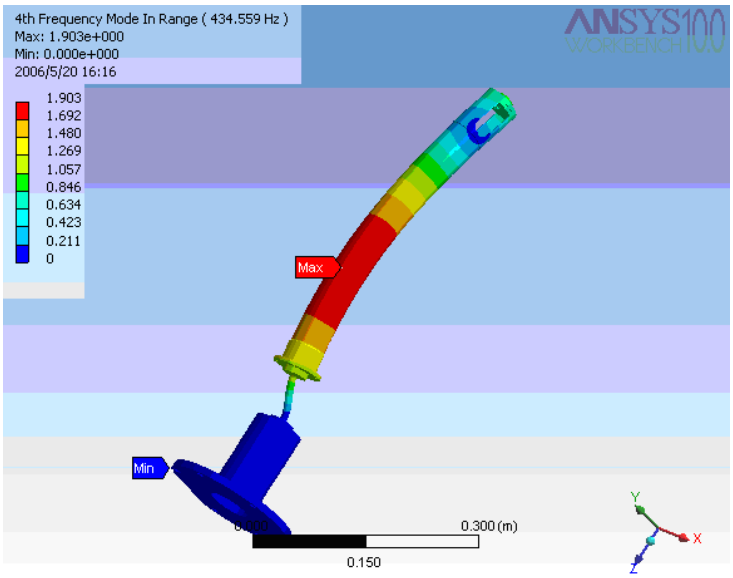

Figure 3.6: IP Leg First Banana Mode

mode of the main flex joint and leg's body together with the upper and lower flex joint deforming in an "S" shape. Because it works in tension, the small flex joint acquires a transversal stiffness Mg/l (where m is the applied load and l is the 30 mm joint's length; see fig. 3.6). The varying transversal stiffness affects the leg's resonance frequency, therefore we can make sure that the load is equalized on the four legs by making sure that the four legs have the same banana mode resonant frequency.

The frequency measurement was performed as shown in fig.3.7. A magnet was attached at some point on the leg (i.e. the support upper cup, see fig. 3.7) and a coil cut from by a small commercial voice speaker was held in front of it from the spring box frame. The measurement was made analyzing the spectrum of the induced current on the coils after hitting the leg. The current passed through a cushy amplifier and low pass filter as well. Under the load of the spring box, the legs were equalized to the frequencies showed in tab.3.2.

leg	1st frequency
0	221
1	218
2	220
3	218

Table 3.2: Legs first banana mode frequency.

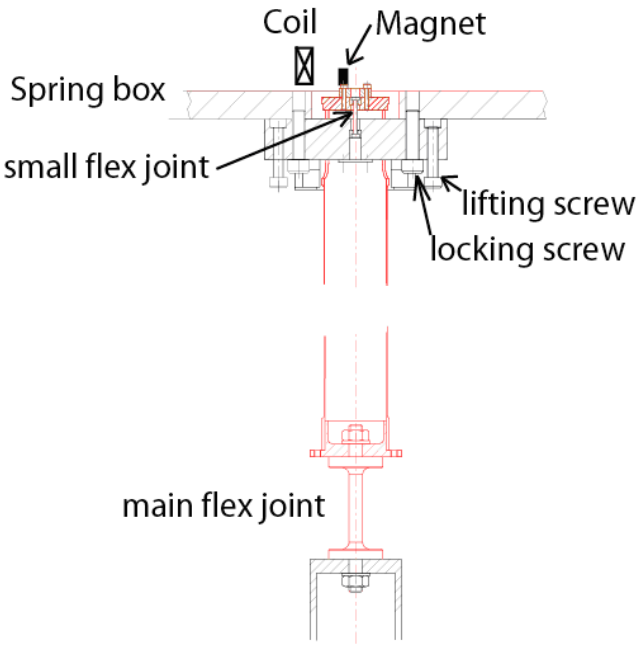

Figure 3.7: Scheme of the IP cup support for the the Spring Box and of the sensor used for the measurement of the frequency.

3.3.2 IP Load Curve

The IP load curve represents an important characterization of the IP. It shows the dependence of the resonant frequency on the mass of the load and permits to estimate the optimal load in order to have the lowest resonant frequency before the IP becomes unstable. It is very important to lower the IP resonant frequency because the attenuation low frequency performance depends on it and because the resonance quality factor also decreases with the square of the resonant frequency. The measurement gives also an estimation of the spring constant of the flex joints.

We measured the curve at the constructor's site, before the overall baking process of the system, obtaining the data shown in fig. 3.9. An induced current sensor referred to the base plate was attached to the spring box bottom plate (similar to that in fig. 3.7). The spring box was excited by pushing it toward one of the directions between two legs. As explained in sec. 2.4.3 - the system tends to have two translational degenerate modes in condition of symmetry of the momentums of inertia along the plane and one rotational mode around the vertical axis. Also the two translational modes are degenerate as long as the four flex joints are cylindrical and mounted perfectly parallel to each other.

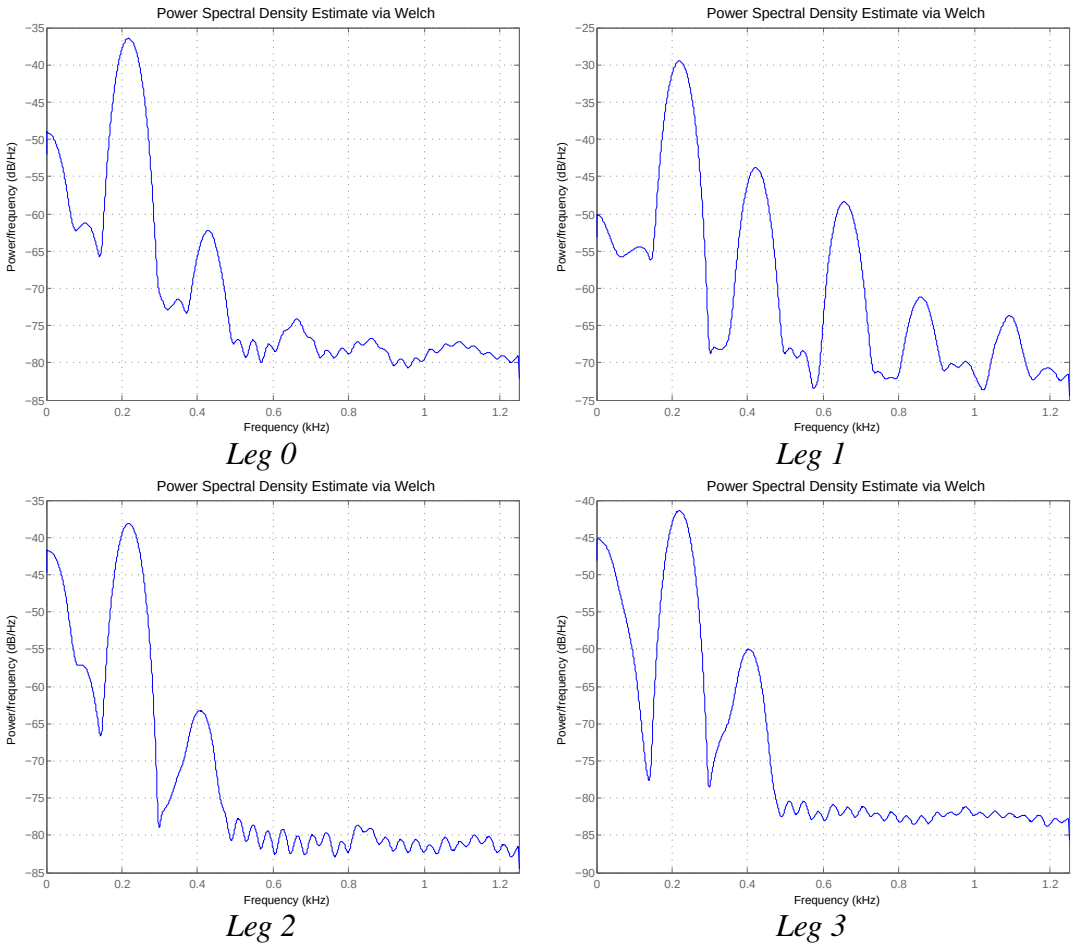

Figure 3.8: PSDs of the four IP legs after the optimization of the load distribuition.

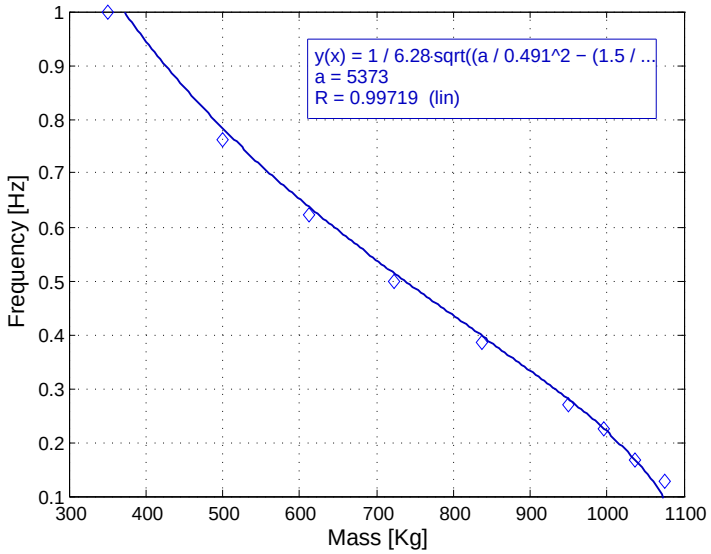

Figure 3.9: IP load curve fit.

Fitting the data with the expression of the frequency

$$f_0 = \frac{1}{2\pi}\sqrt{\frac{\frac{k_\theta}{l^2} - \left(\frac{m}{2} + M\right)\frac{g}{l}}{M}} \tag{3.17}$$

where M is the load mass, $m = 1.5$ Kg is the leg mass of the four legs including its heads and $l = 0.491$ is the IP length, we found $k_\theta = 5373 \pm 25$. The critical mass of about 1100 Kg was found calculating the intersection of the fit at zero frequency

3.3.3 IP Counterweight

The IP conuterweight, designed to bring the theoretical attenuation preformance from 80 dB to 100 dB, were not mounted on the HAM SAS for lack of time.

A mechanical (non numeric) simulation was used for a rough estimation of the counterweight mass and gave a counterweight of ∼150 g.

A specialized sliding table, built to precisely measure the necessary counterweight was built and could never used.

3.4 Optics Table Leveling

Once that the optics table was floating upon the GAS springs it is important to ensure its horizontality.

The first step of the leveling was done with a simple bubble level and adjusting the weights distribution on top of the table. A finer adjustment was made using an optical level and a combination of small mass positioning and the vertical actuators. Four vertical rulers, previously inter-calibrated, were installed on the four corners of the table and the optical level referred to the plumb line. From the MEDM control interface of the ADC (see sec. 4.1) the coil actuators were individually with DC currents until the same height was read on the rulers from the optical level. With the table leveled, the LVDT voltages were acquired as reference point and the values taken into account as offsets to be subtracted out of the four vertical position signals. After this subtraction, zero vertical voltage or four equal voltages in the four LVDTs was then assumed to signal horizontality of the table.

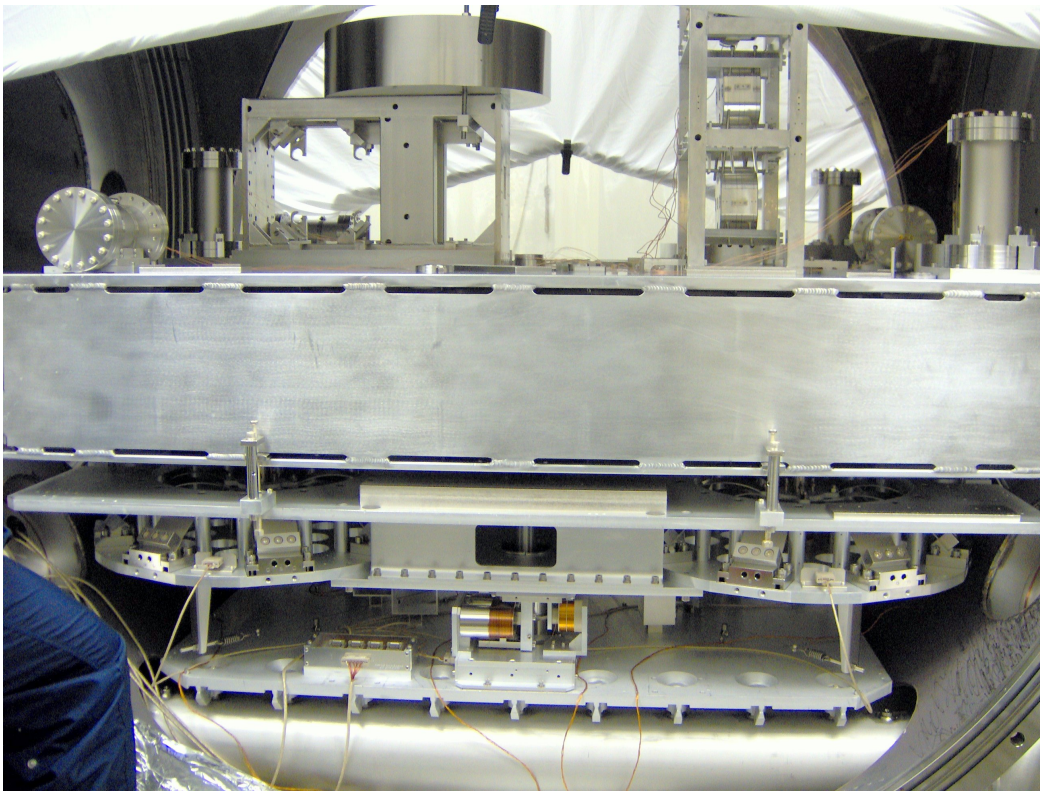

Figure 3.10: HAM-SAS inside the HAM chamber with the optics table and the triple on it.

Chapter 4

Experimental Setup

The particular prototype of HAM-SAS, object of this thesis, was specifically designed to support the optics tables of the output mode cleaner of Enhanced LIGO even though the design of the system is almost the same for all the HAM chambers of the Advanced LIGO interferometers. The tests performed at LASTI were aimed to reproduce those conditions. A triple pendulum, one of the main elements of the Advanced LIGO optics suspensions, was installed on the table (fig.4.2) and several weights were arranged to simulate the same mass distribution and height of the center of mass. Six Mark Products L4-C geophone sensors were placed to monitor the six degrees of freedom of the table and, from outside the chamber, an optical lever to monitor the triple. Guralp CMG-T40 seismometers measured the seismic motion of the ground.

4.1 LIGO Control and Data System (CDS)

The HAM-SAS control and data systems (CDS) are designed according to the LIGO CDS standard and based on the EPICS system[1]. In the front end computer EPICS provides a platform for the execution of the control and monitor programs. The code is written in C by a Matlab Simulink interface in which sensors, actuators and channels have a graphical representation and the controls are implemented in the topology of the connections among the elements (figure.4.13 shows

[1]EPICS is a set of Open Source software tools and applications, written by the Los Alamos and Argonne National laboratories, which provide a software infrastructure for use in building distributed control systems to operate devices such as Particle Accelerators, Large Experiments and major Telescopes. Such distributed control systems typically comprise tens or even hundreds of computers, networked together to allow communication between them and to provide control and feedback of the various parts of the device from a central control room, or even remotely over the internet.

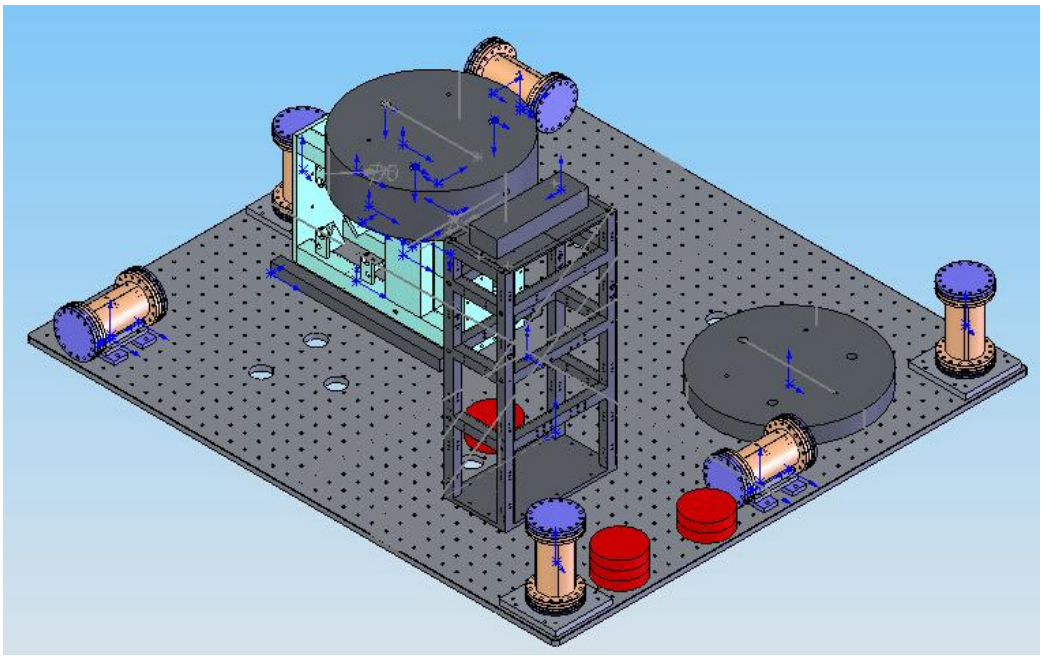

Figure 4.1: Optics table and weight distribution installed on HAM-SAS inside the LASTI HAM vacuum chamber.

the scheme of the Simulink code we wrote for HAM-SAS). The MEDM software provides a graphical command interface (fig.4.3).

4.2 Sensors setup

Several kind of sensors are involved in the HAM-SAS tests : LVDTs, L4C geophones, Guralp seismometers, QPDs. The LVDTs are position sensors while geophones and Guralps are velocity sensors. The LVDT are relative sensors, which means that they measure the position (or velocity) from the relative displacement of a test mass from their reference frame. The sensor frame and the test mass form an harmonic oscillator. The frame follows the system whose position x_0 is the one that has to be measured. In a way that changes depending on the particular kind considered, the sensor measures the relative position $(x - x_0)$ of the mass to the frame. From the equation of motion of the test mass

$$m\ddot{x} = -k(x - x_0), \tag{4.1}$$

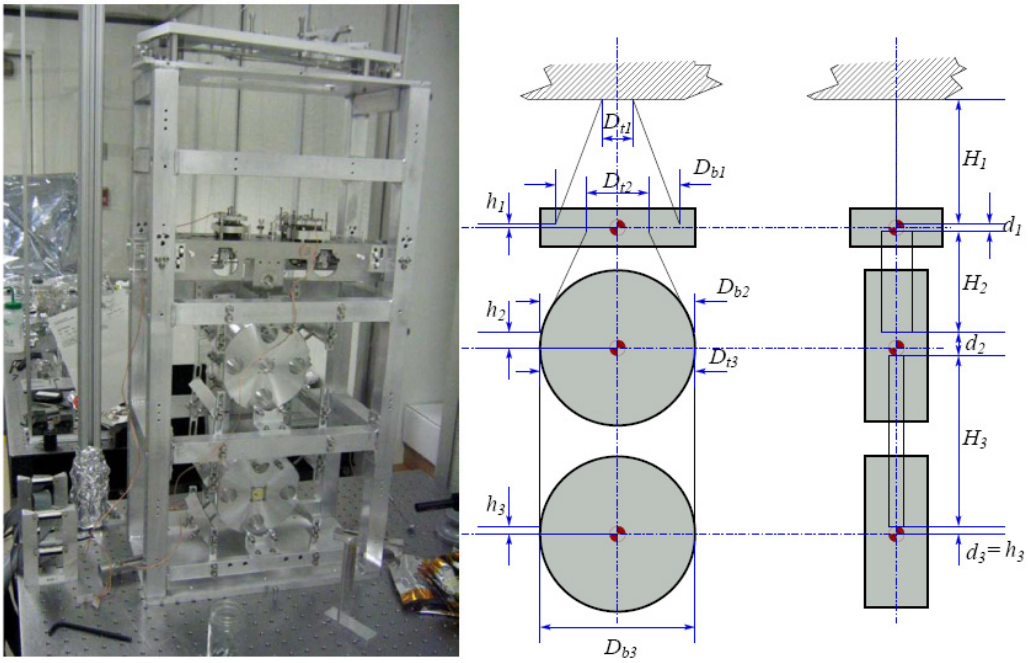

Figure 4.2: Triple pendulum and sketch of a representing model. The triple pendulum is the last stage of the seismic isolation. Its role is to filter the high (>10Hz) frequencies noise using three stages of passive isolation in the horizontal directions and two stages of isolation in the vertical one [44].

neglecting for simplicity any dissipation mechanism, we can obtain the frequency response between the relative displacement and the reference frame:

$$\frac{x_0}{x - x_0} = \frac{\omega_0^2 - \omega^2}{\omega^2}. \tag{4.2}$$

The function in (4.2) depends on the resonant frequency of the system and gives the calibration of the sensor. Multiplying it by the output signal $(x - x_0)$ we obtain the position of the reference[2].

4.2.1 LVDTs

As already mentioned, eight LVDTs are used for position control in HAM-SAS. The LVDTs (Linear Variable Differential Transformers, [33]) are displacement sensors constituted by a primary and two secondary windings. The primary winding is fed with an audio frequency (usually in the range 10-20 kHz) sinusoidal

[2]In the same way all HAM-SAS, together with its LVDTs, could be considered as a big displacement sensors for the ground, that is a seismometer.

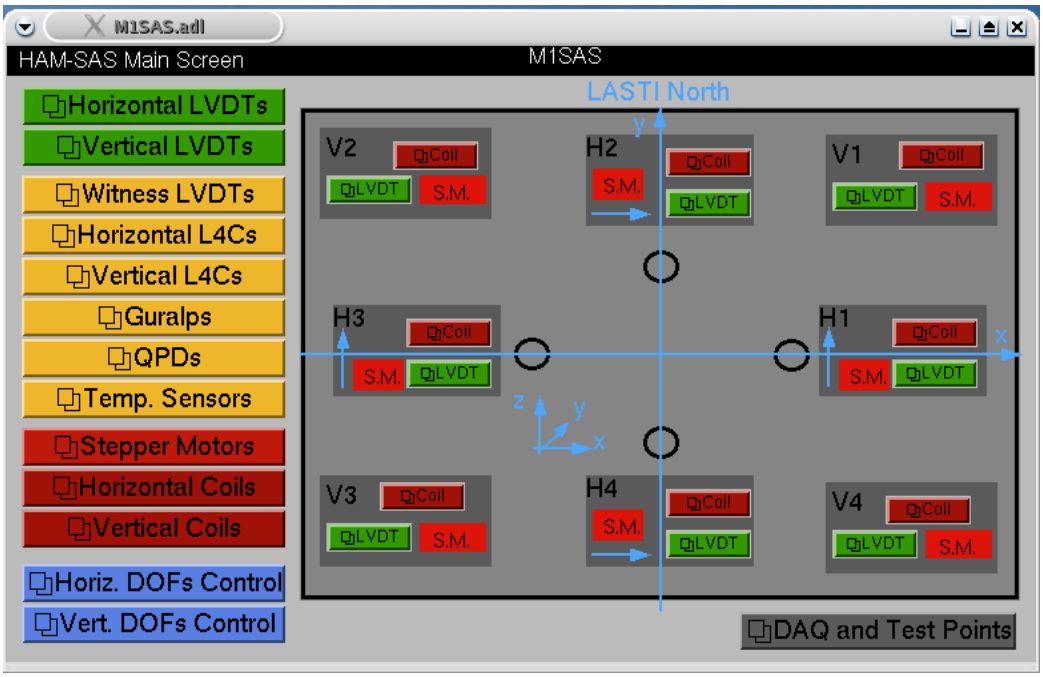

Figure 4.3: HAM-SAS MEDM interface. The platform is represented by the gray rectangle. At the corners, with simbols Vx, are the LVDT sensors, actuators and stepper motors of each GAS filter. The black circles represent the IP legs and have similar sensors and actuators panels.

signal. The secondary winding is composed by two identical coaxial and rigidly interconnected coils, wound in opposite directions. The primary coil general sits in the center between the two secondaries, coaxially oriented. When the primary winding is longitudinally displaced by of an amount Δx, a current with the same frequency of the primary signal and modulated in amplitude proportionally to Δx is induced in the secondary winding. A mixer is then required to demodulate the secondary signal and produce a DC output proportional to Δx. Translations in the other directions, in first approximation, induce no signal.

A VME LVDT driver board is used in HAM-SAS control. The LVDT board specifications are:

- 8 independent channels, first channel set as master in master-slave trigger configurations;
- individually tunable coil excitation levels;
- individually tunable sensor coil read-back amplifier gains;

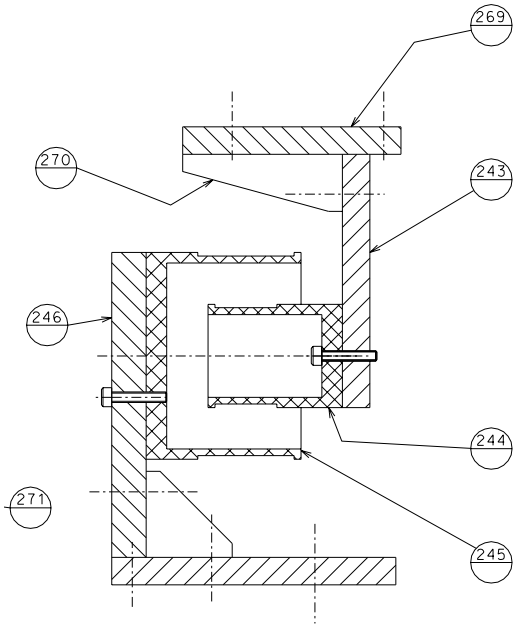

Figure 4.4: Horizontal LVDT scheme. The bracket (269, 270) and (243) supports the primary coil (244) hanging from the springs box. The twin secondary coils are wound on the same cylinder (245) supported by the bracket (246) to the base. The calibration was made measuring the distance between (245) and (246 ,271) with a caliber for several given static position of the spring box.

- One single-ended output per channel for signal monitoring[3];
- One single-ended input, for external oscillator operation;
- One single-ended output, for inter-board synchronization;
- Master-slave/asynchronous operation selectable through onboard jumpers;
- External/internal oscillator operation selectable through onboard jumpers;
- ± 22Vpp primary output voltage;
- ±15V - ±18 V Supply operating voltage;
- 3 24-pin connectors for LVDT primary winding excitations, LVDT secondary winding readbacks, ADC.

[3]The internal oscillator of the first readout circuit can be used as a master for the channel of the boards and to slave all other boards used in the system.

The circuit, shown in fig.4.12, is based on the Analog Devices Universal LVDT Signal Conditioner AD698 chip. The component features are:

- Tunable Internal oscillator from 20 Hz to 20 kHz
- Double channel demodulator: two synchronous demodulator channels are used are used to detect primary and secondary amplitude. The component divides the output of the secondary by the amplitude of the primary and multiplies by a scale factor in order to improve temperature performance and stability. In this way a typical offset drift of 5 ppm/°C and a typical gain drift of 20 ppm/°C are reached;
- Tunable low pass filter for each demodulator;
- Amplifying stage of the output signal.

A phase compensation network is used to add a phase lead or lag to one of the modulator channels in order to compensate for the LVDT primary to secondary phase shift (generated by their inductance). A low noise instrumentation amplifier, INA217, is used for LVDT secondary readbacks differential input. Specifically designed for audio signal amplification, this component has a voltage noise of 1.4 nV/ $\sqrt{\text{Hz}}$ at 1 kHz and a THD[4] of 0.004% at 1kHz for a 100 gain factor. The gain can be adjusted through an external potentiometer. A wide-band fully differential amplifier, THS4131, is used for primary winding excitation output.

Several measurements have been done in order to characterize the performance of the board. An experimental setup, composed by a 50 μm resolution Line Tool micropositioner fixed on an optical table and rigidly connected to the LVDT primary winding, has been used. Several custom made Horizontal LVDT prototypes have been realized in order to determine the optimal ratio between the radii of primary and secondary windings. LVDT spectral density noise measurements (figure 18) has been done after centering the LVDT primary coil to get zero signal output. Several independent measurements have been performed to cover different frequency ranges. Calibration measurements have shown a low level of nonlinearity (less than 1% of the range). Residual displacement noise of 2 nm/ $\sqrt{\text{Hz}}$ at 10 Hz has been measured for both LVDTs. Crosstalks of 1% between the horizontal and longitudinal and between horizontal and vertical degrees of freedom have been obtained. The results obtained in an optimized configuration are summarized in the following table:

[4]The *total harmonic distortion*, or THD, of a signal is a measurement of the harmonic distortion present and is defined as the ratio of the sum of the powers of all harmonic components to the power of the fundamental.

	Horizonta LVDT	Vertical LVDT
Nonlinearity	0.88%	0.26%
Sensitivity	6.49 V/mm	7.85 V/mm
Range	20 mm	20 mm
Displacement Noise	2 nm/ $\sqrt{\text{Hz}}$ 10 Hz	2 nm/ $\sqrt{\text{Hz}}$ 10 Hz

HAM-SAS contains two sets of four LVDTs for the controls and an additional set for monitoring (witness). Each of the control LVDT is co-located with a co-axial voice-coil actuator. Four vertical LVDTs, coaxially located inside the GAS filters, measure the vertical positions of four points of the optics table with respect to the spring box. Four horizontal LVDTs, located in correspondence of the inverted pendulum leg, measure the horizontal displacement of the spring box. The last four are witness LVDTs mounted underneath the top plate supporting the optics table and measure directly the displacement of the table respect to the base, three horizontal and one vertical.

To set up the sensors, we first adjusted the inner offset and gain in the external driver boards in order to adapt the linearity region to the dynamical range of the physical system. (fig. 4.3 shows the map of the LVDTs in the system). Then a first calibration of the horizontal LVDTs had been tried when the system was still out of the HAM chamber. Keeping the optics table mechanically locked in the vertical directions with the apposite stops, we moved the base of the LVDT supporting the primary coil. The procedure turned out to be not practical and the measurements were not clear. Then we repeated the measurement when HAM-SAS was mounted inside the HAM chamber with all the controls active.

The absolute calibration of LVDTs depends on the construction features and tuning of the readout electronics but for equal sensors and electronics the relative calibration is expected to be about the same. To make the actual calibration, we made that initial assumption and applied the geometrical control strategy[5] in order to control the static position of the table along the beam direction, monitored by LVDTs H2 and H4, the only ones accessible by hand. Controls in the other two degrees of freedom also insured that the table remained close to its nominal positions while moving it along the beam. We used the controls to set the table to several positions along x with the controls, measured with a caliber the displacement and read at the same time the correspondent outputs from the ADC. The results of the calibration are shown in fig. 4.5, 4.6 and summarized in tab. 4.2.1. Since it was impossible to get the LVDT H1 and H3 on the sides, we assumed for them the average calibration of H2 and H4.

[5]In the geometrical control strategy the table position is controlled along the main geometrical axis x, y and z aligned with the optics table using the sensing and driving matrices of tab. 5.1 Thanks to the fact that LVDT and actuator are co-axial the driving matrix is simply the transpose of the sensing matrix. (Thzt was the reason underlying the choice in this design of the system.)

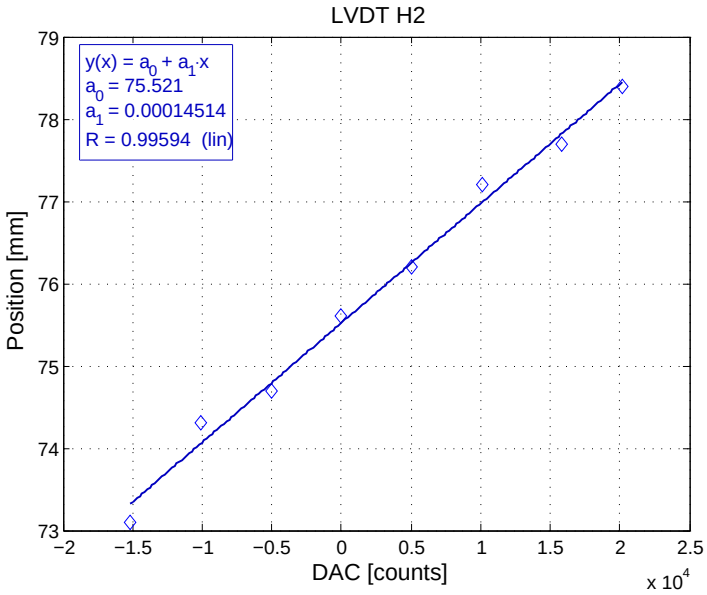

Figure 4.5: H2 LVDT calibration results. The fit gives a coefficient of 0.18 μm/count

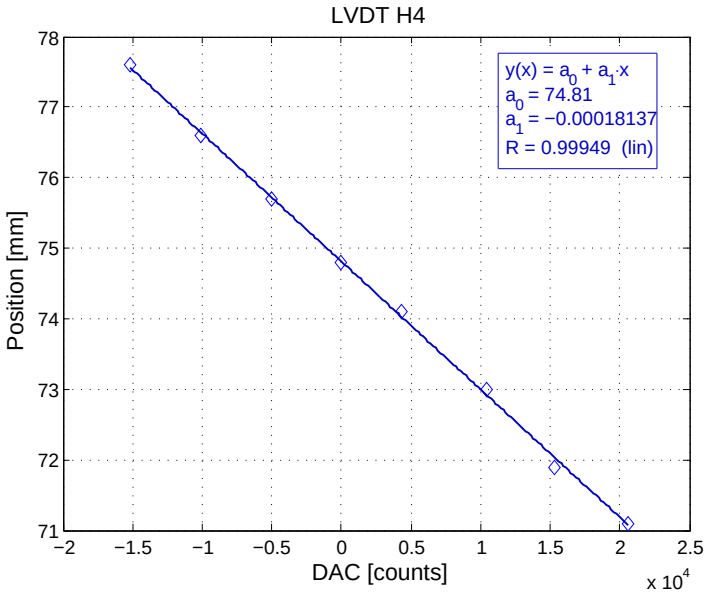

Figure 4.6: H2 LVDT calibration results. The fit gives a coefficient of 0.14 μm/count

LVDT [#]	Slope [Counts/um]	Uncertainty [Counts/um]	Calibration [um/Counts]	Uncertainty [um/Counts]
V1	-4.7281	0.0498	-0.2115	0.0022
V2	4.9162	0.0559	0.2034	0.0023
V3	-4.6772	0.032	-0.2138	0.0015
V4	-5.4043	0.0552	-0.185	0.0019
H1	-6.1255	–	-0.16325	–
H2	6.8898	0.0785	-0.14514	0.0017
H3	-6.1255	–	0.16325	–
H4	-5.5135	0.0628	0.18137	0.0021

Each vertical LVDTs have been calibrated with the system inside the chamber. The vertical LVDT is mounted with two sets of three screws in push-pull mode, to set the electrical zero of the LVDTs at the mechanical working point of the GAS filters. With the optics table and the spring box mechanically locked in all the directions, the support of the LVDT secondary coil was released and moved by a definite number of turns of its holding screws. From the pitch step we measured the displacements and, at the same time, the readouts from the ADC.

Unfortunately, due to their remote positioning, there was no direct way to calibrate the witness LVDTs. They could only be cross calibrated from the control LVDT readout for various position settings.

4.2.2 Geophones

Six geophones are placed on the optics table. As shown in fig. 4.1, three of them, the horizontal, are aligned parallel to the table's plane, in a pinwheel configuration and the other three, the vertical, are orthogonal to the plane, arranged in a triangular configuration. The configuration is such that they can be sensitive to all the six degrees of freedom.

The geophones are relative velocity sensors. The test mass inside is a magnet connected to the sensor's frame by a spring and its velocity is monitored the induced current on a coaxial coil mounted on the frame. In order to pass from velocity to position a calibration filter has to be applied to the signal. The filter is designed on the frequency domain and then implemented on MEDM which provides for the transformation into the time domain. In the frequency domain, the position can be obtained from the velocity simply by dividing by ω, corresponding to the introduction of a pole at zero frequency. The actual calibration we implemented is described in table 4.2.2:

With the geophones calibrated to measure the positions, we can decouple the signals to obtain the coordinates of the system along the six degrees of freedom.

Poles	*Zeroes*	*Gain*
0.50 (3)	0.2847±i*1.0625	0.0129

Table 4.1: Calibration transfer function of the geophones in the zpk format. The three poles at 50 mHz have to be considered like they were poles at zero. The reason for the shift is to avoid the saturation that would happen because of the DC component of the signal from the geophones. Basically the calibration divides by the frequency to obtain from a velocity a signal proportional to the changing position. Then the double pole at zero frequency and the complex zero at about 1 Hz transform the relative displacement of the test mass into absolute position of the reference.

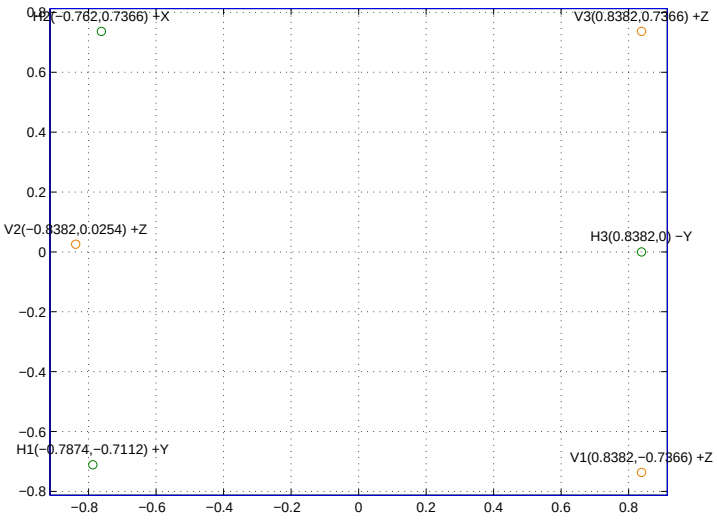

Figure 4.7: Mapping of the geophones on the table

Be $\mathbf{g} = (h_1, h_2, h_3, v_1, v_2, v_3)$ and $\mathbf{r} = (x, y, z, , \theta_y, \theta_z)$ the vectors with the single signals from the geophones and the coordinates of the system respectively. Referring to the mapping of the sensors in fig.4.7 we have that:

$$\begin{pmatrix} h_1 \\ h_2 \\ h_3 \\ v_1 \\ v2 \\ v_3 \end{pmatrix} = \begin{pmatrix} 0 & 1 & 0 & 0 & 0 & H_1^{(x)} \\ 1 & 0 & 0 & 0 & 0 & -H_2^{(y)} \\ 0 & -1 & 0 & 0 & 0 & -H_3^{(x)} \\ 0 & 0 & 1 & V_1^{(y)} & -V_1^{(x)} & 0 \\ 0 & 0 & 1 & V_2^{(y)} & -V_2^{(x)} & 0 \\ 0 & 0 & 1 & V_3^{(y)} & -V_3^{(x)} & 0 \end{pmatrix} \begin{pmatrix} x \\ y \\ z \\ \theta_x \\ \theta_y \\ \theta_z \end{pmatrix}. \tag{4.3}$$

Inverting the matrix in (4.3) and substituting the coordinates of the sensors we find the decoupling matrix.

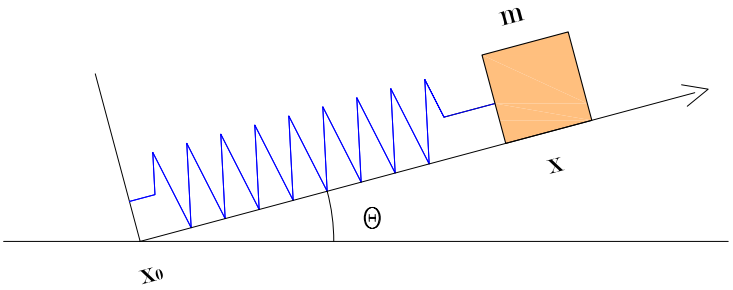

Figure 4.8: Model to explain the tilt to horizontal coupling in the horizontal geophones on the optics table.

4.2.3 Tilt coupling

The horizontal geophones response depends also on the tilt motion of the optics table. As a matter of fact, they measure as horizontal displacement part of what is actually tilt of the optics table. This can be clearly understood if in the model we consider also a rotation of the plane with the geophone as shown in fig.4.8. The overall frequency response include an additional term due to the coupling between of the tilt into the horizontal sensors:

$$\frac{x_0}{x - x_0} = \left(\frac{\omega_0^2 - \omega^2}{\omega^2}\right)_{\text{horizontal}} + \left(\frac{g}{\omega^2}\frac{\theta}{x - x_0}\right)_{\text{tilt coupling}} . \tag{4.4}$$

The term becomes more important at low frequency where it easily dominates over the real horizontal motion. If it were possible to have an independent measure of the tilt, this effect could be taken into account and subtracted out[6].

4.2.4 Optical Lever

An optical lever provides for an independent measurement of yaw and one of the tilt modes of the optics table. A diode laser, positioned on top of a pier just outside the HAM chamber, emits a beam that enters the chamber through a glass porthole and hits the mirror in the middle of the bottom mass of the triple pendulum.[7] The reflected beam reaches the center of a QPD (Quadruple Photo-Detector) sensor placed right next of the laser source. A QPD is made of a four quadrant photodiode in which each quadrant gives a voltage proportional to the inpinging power. The signal share between the four channels depends on the position hit by the beam spot (fig.4.9). The linearity range and sensitivity of this detector depend on the laser spot size.

[6] As is, in certain conditions can dominate the measurement and give an overestimated seismic induced motion.

[7] The triple pendulum is frozen with respect to the optical bench for this measurement.

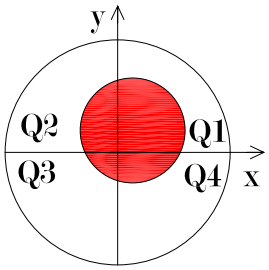

Figure 4.9: QPD sensor. The signal from each quadrant is proportional to the area covered by the beam spot (red). The coordinates of the beam spot's center are given by the differences between the output signals.

The optical lever is set up with the table mechanically locked in all the degrees of freedom. In that condition the beam spot's center is made to coincide with the center of the QPD, equalizing the signal from the quadrants by changing the of the QPD. From the vector with the four signals, the pitch and yaw angles can be obtained by the following decoupling matrix:

$$\begin{pmatrix} \theta_y \\ \theta_z \end{pmatrix} = \frac{2}{l} \begin{pmatrix} 1 & 1 & -1 & -1 \\ 1 & -1 & 1 & -1 \end{pmatrix} \begin{pmatrix} Q_1 \\ Q_2 \\ Q_3 \\ Q_4 \end{pmatrix}. \tag{4.5}$$

in which $l \simeq 1.2\ m$ is the arm lever starting from the middle of the table to the QPD sensor. The output voltage to position calibration is obtained by micrometrically moving the quadrant photodiode.

4.2.5 Seismometer

Three Guralps seismometers are placed around the HAM chamber as shown in fig. 4.10. They are velocity sensors that means that in order to obtain a signal proportional to the position of the ground, they have to have a calibration function similar to that implemented on the geophones. Table 4.2.5 contains the details of the calibration function.

Each of them provides for three output signals correspondent to three orthogonal directions, two horizontal and one vertical called respectively North-South(NS), East-West (EW), Vertical (V). Six of the nine signals are used to measure the motion of the ground around the HAM chamber along the six degrees of freedom.

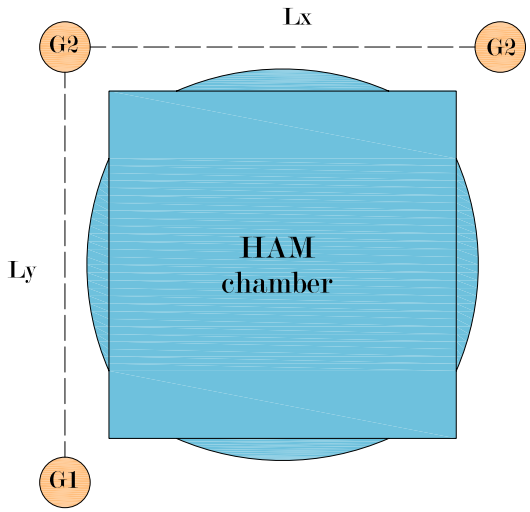

Figure 4.10: Guralp seismometers placements around the HAM chamber.

Poles	*Zeros*	*Gain*
0 (3)	$-23.56 \cdot 10^{-3} \pm i23.56$	-0.314
159	-50	

Table 4.2: Calibration transfer function of the Guralps in the zpk format. As for the geophones, the calibration divides by the frequency to obtain, from a velocity, a signal proportional to the position. Then the double pole at zero frequency and the complex zero at about 23 mHz transform the relative displacement of the test mass into absolute position of the reference. The poles at 159 HZ and the zero at 50 are specified by the constructor.

We used the following decoupling matrix for signal of the Guralps[8].

$$\begin{pmatrix} x \\ y \\ z \\ \theta_x \\ \theta_y \\ \theta_z \end{pmatrix} = \begin{pmatrix} 0 & 0 & 1/3 & 0 & 0 & 1/3 & 0 & 0 & 1/3 \\ 0 & 1/2 & 0 & 0 & 0 & 0 & 0 & 1/2 & 0 \\ 1/3 & 0 & 0 & 1/3 & 0 & 0 & 1/3 & 0 & 0 \\ 0 & 0 & 0 & 1/\mathrm{ly} & 0 & 0 & -1/\mathrm{ly} & 0 & 0 \\ 1/\mathrm{lx} & 0 & 0 & -1/\mathrm{lx} & 0 & 0 & 0 & 0 & 0 \\ 0 & 1/\mathrm{lx} & 0 & 0 & 0 & 0 & 0 & -1/\mathrm{lx} & 0 \end{pmatrix} \begin{pmatrix} \mathrm{V1} \\ \mathrm{NS1} \\ \mathrm{EW1} \\ \mathrm{V2} \\ \mathrm{NS2} \\ \mathrm{EW2} \\ \mathrm{V3} \\ \mathrm{NS3} \\ \mathrm{EW3} \end{pmatrix}. \tag{4.6}$$

[8]The fifth column is null because the channel NS of G2 was broken

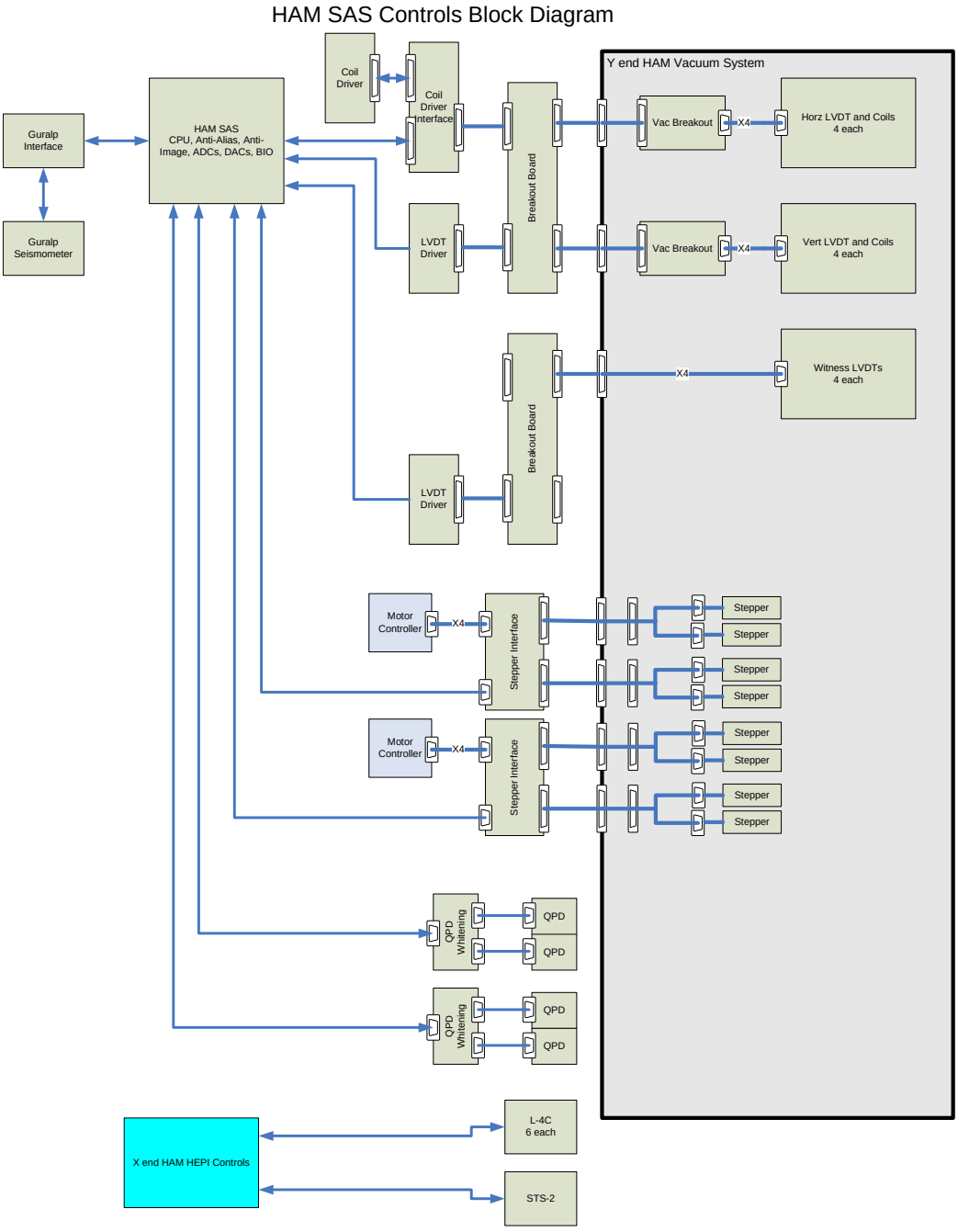

Figure 4.11: HAM SAS Controls Block Diagram.

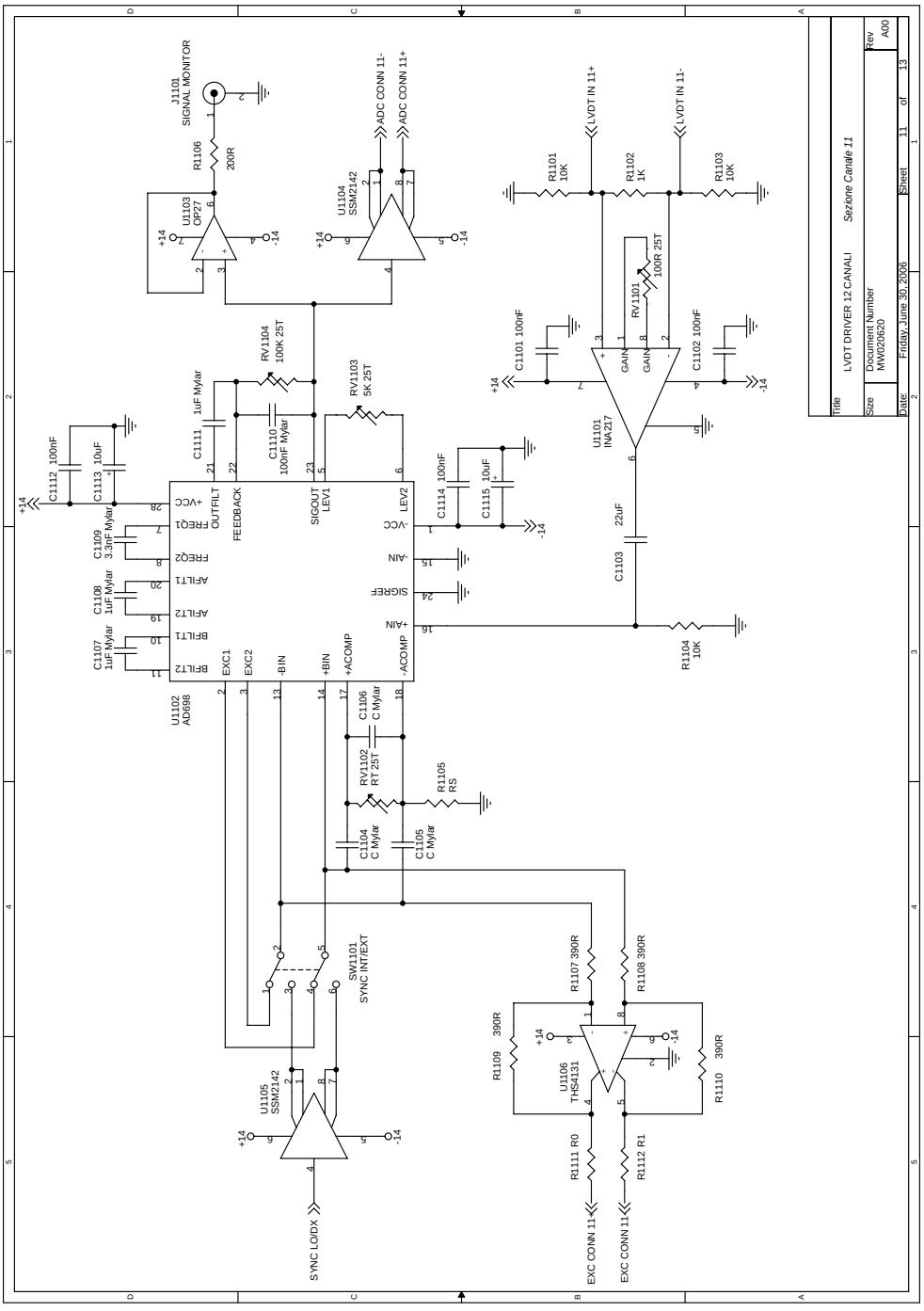

Figure 4.12: LVDT driver board master channel

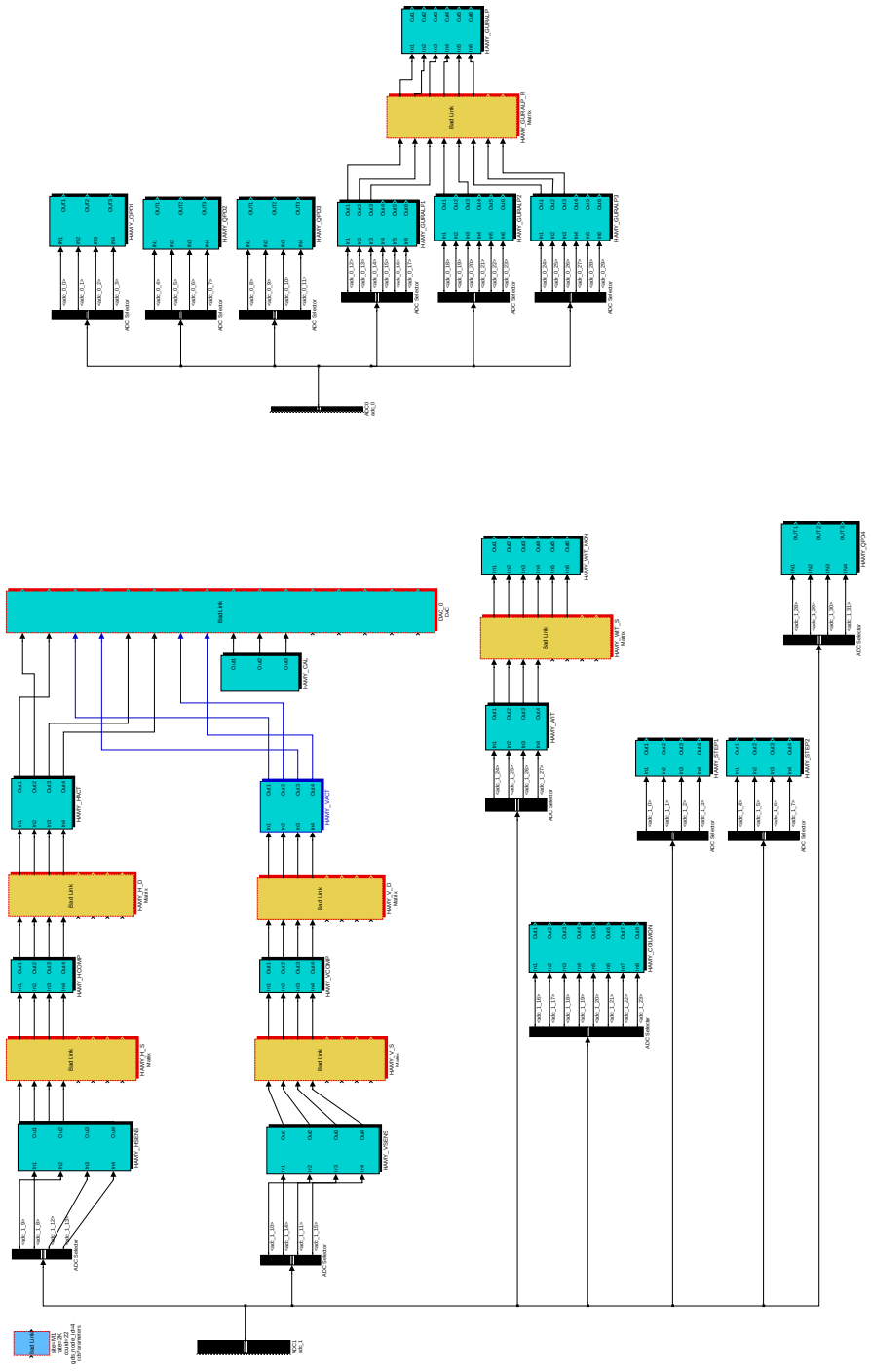

Figure 4.13: Simulink representation of the HAM-SAS front end code

Chapter 5

HAM-SAS control

5.1 Optics Table Control

The optics table is a 6 degree of freedom mechanical system: 6 independent sensors are required to fully determine its position and 6 independent actuators to move it. Each physical sensor is, in principle, sensitive to movements in all the 6 normal modes (which in the following will be often referred to as x, y, θ_z, z, θ_x, θ_y, although they do not correspond necessarily to pure translations and rotations). In the same way, each actuator will generate movements of the optics table involving a mix of the 6 modes. The basic idea of the HAM-SAS controls is to treat as separate the horizontal from the vertical DOFs and to diagonalize the sensing and control actions: the aim is to pass from the sensors/actuators space, to a space where each normal mode is independently sensed and acted upon. Mathematically, this means to realize a coordinate transformation for each group of degrees of freedom such that the equations of motions get the form:

$$\ddot{x}_i + \omega_i^2 x_i = q_i \tag{5.1}$$

where x_i (for i = 1; 2; 3) is a normal mode coordinate, $\omega_i/2\pi$ is the resonant frequency of the $i - th$ mode and q_i is the generalized force corresponding to the coordinate x_i [45, 31]. Experimentally this means to find 3 linear combinations of the sensor outputs, defined *virtual sensors*, each sensitive to a single normal mode and, correspondingly, 3 linear combinations of the excitation coil currents (virtual actuators) which excite each mode separately. In control theory terminology, this means to break down a *multiple in-multiple out* (MIMO) system into many *single in-single out* (SISO) systems. The control of a SISO system is much easier: every mode is controlled by an independent feedback loop, simplyfing greately the loop design and the seismic requirements.

5.2 Diagonalization

The GAS filters support the optics table in such a way that the relative movement of the suspension points respect to the spring box is mostly limited to the vertical direction. This significantly reduces the coupling between the horizontal DOFs of the table (x, y and roll) and the verticals (z, pitch, yaw) and allows to treat them separately into two stages. Let us consider only one stage, i.e. the horizontal.

Be $\mathbf{u}(s)$ the vector containing the Laplace transform of the positions of the four LVDT sensors, and $\mathbf{v}(s)$ the vector with the transforms of the forces exerted by the actuators. We have that

$$\mathbf{u} = \mathbf{H}\,\mathbf{v} \tag{5.2}$$

where $\mathbf{H}$ is a 4×4 matrix in which the generic element h_{ij} represents the transfer function between the actuator j and the sensor i. Neglecting the vertical to the horizontal couplings, each of these transfer functions can be written as a linear combination of three oscillators, one for each of the normal modes of the system:

$$h_{ij}(s) = \frac{u_i(s)}{v_j(s)} = \sum_{k=0}^{3} a_k^{(ij)} \frac{\omega_{0k}^2}{s^2 + \omega_{0k}^2 + i\omega_{0k}^2\phi_k} \tag{5.3}$$

where $a_k^{(ij)}$ is the coupling coefficient for the k-th mode, ω_{0k} the mode's resonant frequency. For $h_{ij}(i\omega)$ we can expect the shape resulting from three overimposed harmonic oscillator functions to look like the graph in fig.5.1.

We have that $\mathbf{u} \in U$, sensors space, and $\mathbf{v} \in V$, actuators space. It is possible to pass to basis for U and for V such that the transfer function matrix H becomes diagonal. With this choice of basis each sensor is a modal sensor which is sensitive to only one of the normal modes of the system. In the same way each actuator becomes a modal actuator wich is able to act only on one mode. In the new coordinates

$$\mathbf{x} = \widetilde{\mathbf{H}}\mathbf{q} \tag{5.4}$$

$$\tilde{h}_{ij}(s) = \frac{x_i(s)}{q_j(s)} = b_k\, h_{ij}(s)\, \delta_{ijk} \tag{5.5}$$

where δ_{ijk} is the Kronecker tensor. Be $\mathbf{S}$ and $\mathbf{D}$ the basis change matrices for U and V representing the *sensing matrix* and *driving matrix* respectively. We have that:

$$\mathbf{x} = \mathbf{S}\mathbf{u} \tag{5.6}$$

$$\mathbf{v} = \mathbf{D}\mathbf{q} \tag{5.7}$$

$$\mathbf{S}\mathbf{u} = \widetilde{\mathbf{H}}\mathbf{D}^{-1}\mathbf{v} \tag{5.8}$$

which makes

$$\mathbf{H} = \mathbf{S}^{-1}\widetilde{\mathbf{H}}\mathbf{D}^{-1} \tag{5.9}$$

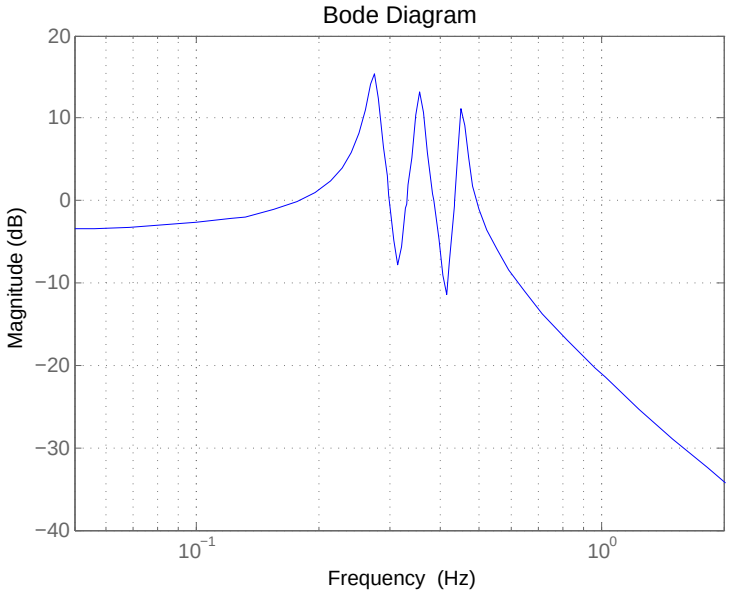

Figure 5.1: Typical real sensor to actuator transfer function.

5.2.1 Measuring the sensing matrix

Being $\mathbf{u} = \mathbf{S^{-1}x}$ we know that the column vectors of $\mathbf{S^{-1}}$ represent the relative sensitivy of the real sensors to each single mode. The only matrix we can measure directly is $\mathbf{H}$ but we can reduce it to a matrix physically equivalent to $\mathbf{S^{-1}}$. We choose one of the real actuators, say v_1, and use it to excite the system. We then measure all the quantities $h_{i1}(\omega_k)$ in correspondence of the three resonant frequencies of the three modes of interest. Taking the imaginary part of these numbers we can build the matrix

$$\mathbf{M} = \begin{pmatrix} \Im\left[h_{11}(\omega_1)\right] & \cdots & \Im\left[h_{11}(\omega_3)\right] \\ \vdots & & \vdots \\ \Im\left[h_{31}(\omega_1)\right] & \cdots & \Im\left[h_{31}(\omega_3)\right] \end{pmatrix} \tag{5.10}$$

and it can be shown that $\mathbf{S^{-1}}$ and $\mathbf{M}$ are equivalent and differ only for a scale factor that multiplies each column.

In fact, let us define $\mathbf{S^{-1}} = \{\sigma_{ij}\}$ and $\mathbf{D^{-1}} = \{\Delta_{ij}\}$. From 5.9 and 5.5 we can write

$$h_{ij}(s) = \sum_{k=1}^{3} \sigma_{ik}\tilde{h}_{kk}\Delta_{kj}. \tag{5.11}$$

At the resonance ω_k

$$\tilde{h}_{kk}(i\omega_k) \approx \Im[\tilde{h}_{kk}(i\omega_k)] = -b_k Q_k \tag{5.12}$$

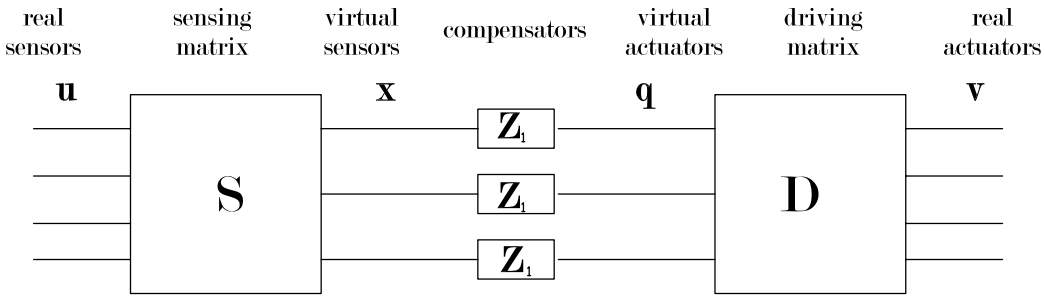

Figure 5.2: Diagonalization scheme

$$h_{ij}(i\omega_k) = -\sigma_{ik} b_k Q_k \Delta_{kj} \tag{5.13}$$

and this means that

$$\mathbf{M} = \begin{pmatrix} -\sigma_{11}\, b_1\, Q_1\, \Delta_{11} & \cdots & -\sigma_{13}\, b_3\, Q_3\, \Delta_{31} \\ \vdots & & \vdots \\ -\sigma_{31}\, b_1\, Q_1\, \Delta_{11} & \cdots & -\sigma_{33}\, b_3\, Q_3\, \Delta_{31} \end{pmatrix} = \left[\alpha_1\, \sigma^{(1)},\ \alpha_2\, \sigma^{(2)},\ \alpha_3\, \sigma^{(3)}\right]. \tag{5.14}$$

$\mathbf{S^{-1}}$ and $\mathbf{M}$ are equivalent because the α factors only change the length of the eigenvectors but not their relative angles. Physically those factors only set the global sensitivity of the sensors to each mode but do not change the relative sensitivity among the sensors to one mode.

The same consideration holds if instead of v_1 we had chosen an other actuator to evaluate the matrix. As long as the system is linear, no matter how we excite a mode, we can get different α values but the ratios between the conversion coefficients in each column of M rest the same.

5.2.2 Measuring the driving matrix

Now, since we have defined the modal sensors, we can measure the driving matrix from their relation with the real actuators

$$\mathbf{x} = \widetilde{\mathbf{H}}\mathbf{D^{-1}}\,\mathbf{v} = \mathbf{N}\,\mathbf{v} \tag{5.15}$$

by simply measuring the ratios

$$\frac{x_i(i\omega)}{v_j(i\omega)} = n_{ij} \tag{5.16}$$

at a fixed frequency. Even though $\mathbf{N}(s)$ is frequency dependent all the dependence is in $\widetilde{\mathbf{H}}$. Since H is a diagonal matrix, $\mathbf{N}$ and $\mathbf{D}^{-1}$ are equivalent. The only specification is that the test frequency at which the measurement is made must be lower than all the resonant frequencies in order to neglect the imaginary part of n_{ij} and have only real numbers to build the matrix.

$$\begin{bmatrix} 1/4 & 1/4 & 1/4 & 1/4 \\ 1/2 & 0 & -1/2 & 0 \\ 0 & 1/2 & 0 & -1/2 \\ 0 & 0 & 0 & 0 \end{bmatrix}$$

Vertical Sensing

$$\begin{bmatrix} 1/4 & 1/2 & 0 & 0 \\ 1/4 & 0 & 1/2 & 0 \\ 1/4 & -1/2 & 0 & 0 \\ 1/4 & 0 & -1/2 & 0 \end{bmatrix}$$

Vertical Driving

$$\begin{bmatrix} 0 & 1/2 & 0 & 1/2 \\ 1/2 & 0 & 1/2 & 0 \\ 1/4 & -1/4 & -1/4 & 1/4 \\ 0 & 0 & 0 & 0 \end{bmatrix}$$

Horizontal Sensing

$$\begin{bmatrix} 0 & 1/2 & 1/4 & 0 \\ 1/2 & 0 & -1/4 & 0 \\ 0 & 1/2 & -1/4 & 0 \\ 1/2 & 0 & 1/4 & 0 \end{bmatrix}$$

Horizontal Driving

Table 5.1: Geometrical diagonalization matrices

5.2.3 Experimental diagonalization

Experimentally the diagonalization of sensors and actuators is an iterative process. The two procedure can be reiterated many times until the virtual sensors are well decoupled and sensitive to the normal modes of the system. On each iteration the virtual sensors are assumed to be real and the new sensing and driving matrices obtained have to be multiplied to the left of the old ones.

For each of the stages we started the diagonalization from the geometrical sensing and driving matrices. That immediately reduced the redundancy of the sensors and actuators. As discussed in sec. 2.4.3, from the symmetry of the system, we expected the modes to be two pure translations and a pure rotation and thus the transfer function to be not too far from being already diagonal with that choice of base. For the vertical DOFs we chose two main axis along the diagonals of the table and the third one along the vertical direction as eigenaxis. For the horizontals, we considered two translational modes along x and y and a rotational mode around the vertical axis. The corresponding matrices are shown in tab 5.1.

For each stage, either horizontal or vertical, we measured the transfer functions between one virtual actuator and all the virtual sensors of the same stage of DOFs. We extracted the imaginary parts in correspondence of the peaks for each sensor and with these we wrote $\mathbf{S^{-1}}$. Then we inverted it to obtain $\mathbf{S}$ and transformed to a 4×4 matrix filling the last column and row with zeros. Finally we multiplied this to the left of the geometric sensing matrix obtaining a new one. The procedure was repeated for each actuator and the obtained matrices were averaged using the

$$\begin{bmatrix} -0.12 & 0.32 & 1 & 0.33 \\ 1 & 0.44 & -0.42 & 0.15 \\ -0.27 & 1 & 0.30 & -1 \\ 0 & 0 & 0 & 0 \end{bmatrix} \qquad \begin{bmatrix} 0.04 & 1 & -0.20 & 0 \\ 0.46 & 0.74 & 0.94 & 0 \\ 1 & -0.04 & 0.15 & 0 \\ 0.57 & 0.21 & -1 & 0 \end{bmatrix}$$

Vertical Sensing *Vertical Driving*

$$\begin{bmatrix} -1 & 0.81 & -0.15 & 0.07 \\ 0.76 & 1 & 0.32 & 0.52 \\ -0.37 & -0.30 & -1 & 1 \\ 0 & 0 & 0 & 0 \end{bmatrix} \qquad \begin{bmatrix} -1 & 0.83 & -0.41 & 0 \\ 0.50 & 0.92 & 0.14 & 0 \\ -0.63 & 0.76 & -1 & 0 \\ 0.13 & 1 & 0.73 & 0 \end{bmatrix}$$

Horizontal Sensing *Horizontal Driving*

Table 5.2: Measured sensing and driving matrices.

norm of the columns as weight. Figures 5.2.3 and 5.2.3 show the transfer functions for the excitation of the Y an Z geometrical virtual actuators respectively.

The inverse of the driving matrix was obtained exciting each geometric virtual actuator one at a time at a fixed low frequency and measuring the transfer coefficients[1] between the virtual sensors as obtained from the new sensing matrix. Then it was inverted, converted to a 4×4 matrix filling the last column and row with zeros and multiplied by the driving matrix.

The amplitude chosen for the excitations determined the signal to noise ratio and the quality of the measurements. The measured matrices are shown in fig.5.2.

The most troublesome to measure was the vertical driving matrix. The transfer coefficients have been always characterized by not negligible imaginary parts even if they were measured at frequencies much lower than the resonances. The reason is probably in a certain amount of coupling with the horizontal DOFs introduced by exciting the table in the range of frequencies where the horizontal resonances occur. This supposed coupling did not produced the same problem in the measurement of the horizontal driving matrix probably because the vertical resonances are all well above the horizontal ones. When the imaginary parts were about the same as the real, the simple transpose of the sensing matrix turned out to be more effective than the measured driving matrix to control the modes. The reason for this is that the vertical actuators are perfectly aligned with the vertical

[1]The transfer coefficient is the value of a transfer function at a given point.

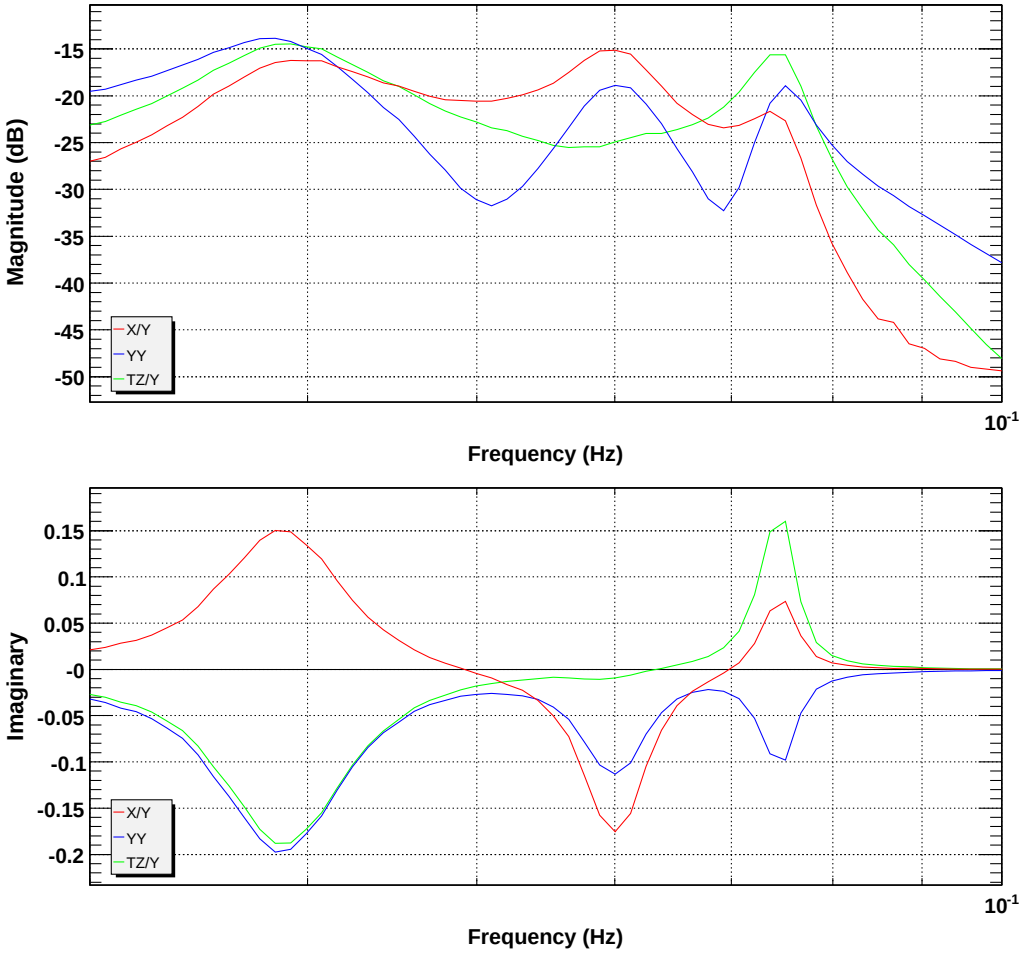

Figure 5.3: Magnitude and imaginary part of the transfer function between the geometrical horizontal DOFs and the geometrical virtual actuator Y. In the peaks of the imaginary parts we get the frequencies of the horizontal modes: 38 mHz; 60 mHz; 75 mHz.

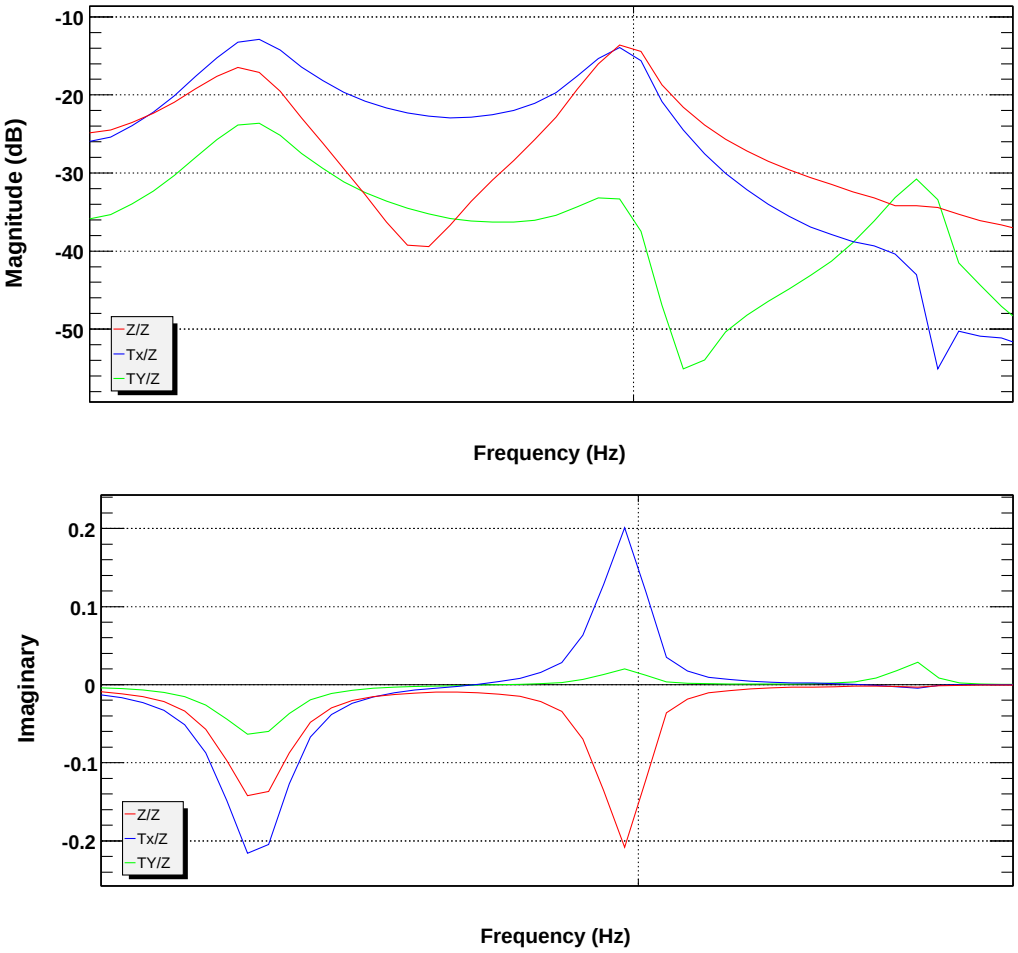

Figure 5.4: Magnitude and imaginary part of the transfer function between the geometrical vertical DOFs and the virtual geometrical actuator Z. The frequency of the modes are: 146 mHz; 198 mHz; 250 mHz.

$$\begin{bmatrix} 0.81 & 1 & 0.50 \\ -1 & 0.60 & -0.60 \\ -0.98 & 0.04 & 1 \end{bmatrix} \qquad \begin{bmatrix} 0.65 & 1 & 0.07 \\ 1 & -0.98 & 0.20 \\ 0.30 & -0.10 & -1 \end{bmatrix}$$

Vertical Modes *Horizontal Modes*

Table 5.3: Inverse of the measured sensing matrices. The columns define the eigenmodes of the system. For the vertical the frequencies are: 146 mHz, 198 mHz, 250 mHz respectively. For the horizontal they are: 38 mHz, 60 mHz, 75 mHz.

LVDTs and, for construction reasons, they must share almost the same calibration current-force among each other.

Figure 5.8,5.9 shows the comparison between the LVDT spectra as obtained by the real sensors, the geometric virtual sensors and the diagonalized sensors.

5.2.4 Identifying the normal modes

From section 5.2.1 it follows that the columns of the inverse of the measured sensing matrix $\mathbf{S^{-1}}$ represent the eigenmodes of the system in the basis of the space in which the matrix is measured. In the case of the geometrical basis, the columns represent the projection of the modes on the x, y and θ_z conventional axis chosen for HAM-SAS.

Table 5.3 contains the vertical and horizontal inverse of the sensing matrices with the eigenmodes as column vectors in the geometric basis representation. The calibration of the LVDT sensors and the inclusion of the arm lengths in the geometrical matrices are essential for the modes to be interpreted in that basis. In particular, in the horizontal matrix the first row has to be intended as meters along x, the second as meters along y and the third as radiants around z. In the vertical matrix, the first row represent meters of transaltion along z. The second is the one we called θ_x (even though it corresponds to a rotation around the diagonal with LVDT sensors V1 and V3) and the third is θ_y (corresponding to the opposite diagonal, between V2 and V4). A more realistic comparison between the geometrical projections of the modes could be done looking at the energies stored in each of them, which can be estimated from the products of the square of the amplitudes for the mass of the system in the case of the translation components, and for the moments of inertia for the rotations: Mx^2, My^2 $I_z\theta_z^2$, Mz^2, $I_x\theta_x^2$, $I_y\theta_y^2$.

In the vertical matrix, the ratio between the third and the second rows' components represents the direction of the eigenaxis in the horizontal plane measured from the first diagonal. From the measured matrices we have that the first mode roughly corresponds to a rotation around the actual y axis plus a translation along

z. The second is mostly a vertical translation plus a rotation around the first diagonal. The third is a vertical translation plus a rotation around an axis which is closer to the first diagonal than to the second[2].

The horizontal matrix was closer to expectations than the vertical. The third column contains a mode which is almost a pure rotation around z. The second is mostly a translation at about 45 degrees between the x and y axis. The first is a mix of a translation along an axis somewhere in between x and y axis and a rotation around the vertical axis.

5.2.5 Actuators calibration

The actuators redundancy allows driving modes which applies null resultant force and null resultant torque to the optics table. In case of equal calibrations between the actuators, these modes are represented by the vector $\mathbf{w_h} = (1, -1, -1, 1)$ for the horizontal actuators and by the vector $\mathbf{w_v} = (1, -1, 1, -1)$ for the vertical actuators (in the vertical case these modes are called *saddle* or *pringle modes*[3]. The geometric diagonalization of the driving matrix excludes actuators' combinations that could drive as pringle modes, as long as the actuators have the same force calibration. Geometrically the image of the vertical matrix $\mathbf{D_v}$ is a 3-dim space orthogonal to the actuation vector $\mathbf{w_v}$ and the image of $\mathbf{D_h}$ is orthogonal to $\mathbf{w_h}$. If the orthogonality is not guaranteed each of the actuators applies a different force for the same current. Thus the scalar product between the pringle vector and the columns of the driving matrix tells us about the actuators' calibration.

From 5.2 we have from the vertical driving matrix:

$$\begin{aligned} \mathbf{D_v}^{(1)} \cdot \mathbf{w_v} &= 0.67 \\ \mathbf{D_v}^{(2)} \cdot \mathbf{w_v} &= 0.00 \\ \mathbf{D_v}^{(3)} \cdot \mathbf{w_v} &= 0.00 \end{aligned} \tag{5.17}$$

and from the horizontal:

$$\begin{aligned} \mathbf{D_h}^{(1)} \cdot \mathbf{w_h} &= 0.00 \\ \mathbf{D_h}^{(2)} \cdot \mathbf{w_h} &= 0.00 \\ \mathbf{D_h}^{(3)} \cdot \mathbf{w_h} &= 0.00 \end{aligned} \tag{5.18}$$

[2]These asymmetries can be explained with a transversal stress applied mostly on the GAS filter number 1 (which is forced to work crookedly) by an error in assembly. Testing this hypothesis would require disassembly and reassembly of the system, which could not be performed for lack of time.

[3]The reason is that they would tend to bend the table in a way similar to the shape of a horse saddle or of a pringle potate chip.

in which the vectors have been first normalized. These numbers confirm the problems encountered with the vertical driving matrix already discussed in section (5.2.3)[4]. In the case of the horizontal actuators, the products are null implying that the calibrations of the actuators are the same.

5.2.6 System Transfer Function

Once we diagonalized the DOFs, we measured the transfer function between every virtual sensor and its correspondent virtual actuator. The results are shown in fig.5.13,5.14. These represent a very important characterization of the system, essential to design the control loops and to evaluate the attenuation performance of the system.

5.3 Control Strategy

HAM-SAS was designed basically as a passive system. The role of the controls is as minimal as possible. They are mostly intended to assist the platform to be in the optimal conditions to give for the best performance. However, since the mechanics is not optimized, controls are also used to compensate and overcome the tuning limitations. The controls mainly provide to: position the optics table in order to be at the optical working point of the filters; to damp the resonances associates with the normal modes of the system; to reduce the effective stiffness of the eigenmodes and thus the resonant frequencies.

5.3.1 Control topology

Once we diagonalized the system's transfer function, the control strategy reduces to that of a SISO system and, starting from the physical plant responses, individual control loops can be designed for every DOF.

In HAM-SAS the LVDT position sensors are used. The scheme in fig.5.5 illustrates the controls topology for one degree of freedom: x_0 is the position of the ground (input) and x that of the optics table (output), x_{off} an offset that determines the desired working point of the optical table in the x direction.; G represents the system and C the compensator. Assuming x_{off} constant, the closed loop transfer function in the s-space is then

$$\frac{x(s)}{x_0(s)} = \frac{G(s)\,(1 + C(s))}{1 + G(s)C(s)} \tag{5.19}$$

[4]The problem may originate from the fact that at least one of the vertical LVDT-actuator units is warped, and therefore the geometrical diagonalization is not a completely orthogonal one.

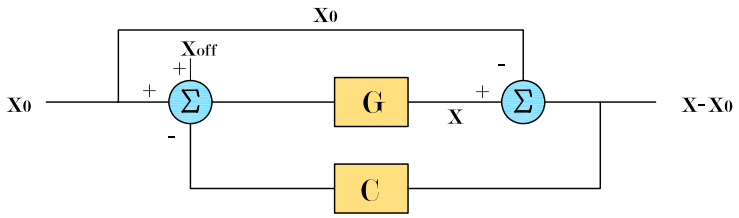

Figure 5.5: Control loop scheme for relative position sensor.

in which $G(s)$ is the physical plant response of the system and $C(s)$ the compensator's transfer function.

5.3.2 Static Position Control (DC)

The purpose of a static position control is to keep the system at an assigned position x_{off} within a defined time scale. the offset x_{off} can be possibly be null, in that case $x = x_0$. A compensator which adds a signal proportional to the time average of the relative position over a defined amount of time can control the position if it is made of an integrator [46]:

$$C(x) = \frac{\alpha}{s} \tag{5.20}$$

in which α sets the gain and has the dimension of a frequency. Considering the general case in which $x_{off} \neq 0$, from 5.19 we have

$$\frac{x(s)}{x_0(s)} = \frac{G(s)\,(1 + C(s))}{1 + G(s)C(s)} + \frac{x_{off}(s)}{1 + G(s)C(s}. \tag{5.21}$$

An offset x_{off} can be modeled as a step function:

$$x_{off} = \begin{cases} 0 & \text{if } t < 0 \\ \tilde{x}_{off} & \text{if } t \geq 0 \end{cases} \tag{5.22}$$

and since this control loop works at ultra low frequency, in that band we can consider $G(s) \simeq 1$ and from (5.21) we have:

$$x(s) - x_0(s) = \frac{\tilde{x}_{off}}{s + \alpha}. \tag{5.23}$$

The time evolution of the position is then obtained from the Laplace inverse:

$$x(t) - x_0(t) = \mathcal{L}^{-1}\left[\frac{\tilde{x}_{off}}{s + \alpha}\right] = \tilde{x}_{\text{off}}\, e^{-\alpha t}. \tag{5.24}$$

We have that α defines the time constant of the process ($\tau = 1/\alpha$) and the loop bandwidth. The unity gain is obtained solving

$$|G(s)C(s)| \simeq \left|\frac{\alpha}{s}\right| = 1 \tag{5.25}$$

which places the unitary gain at:

$$f_{\text{u.g}} = \frac{\alpha}{2\pi}. \tag{5.26}$$

Since the open loop transfer function $G(s)C(s)$ has a phase smaller than -180 degrees above the resonant frequency of $G(s)$, the Nyquist criterion then requires $f_{\text{u.g}}$ to be lower than the resonance of the system $G(s)$ in order for the system to be stable.

5.3.3 Velocity Control (Viscous Damping)

A velocity control is used to apply viscous damping to the system. A force proportional to the relative velocity $(\dot{x} - \dot{x}_0)$ is realized by means of a derivative compensator of the form

$$C(s) = \gamma s \tag{5.27}$$

In particular the quality factor of the system can be reduced by γ since we have that:

$$Q = \frac{\omega_0 m}{\gamma}. \tag{5.28}$$

5.3.4 Stiffness Control (EMAS)

The Electro-Magnetic Anti-Spring strategy (EMAS) was already developed as part of the SAS technology but it has been applied for the first time extensively and by mean of a digital feedback control system in HAM SAS. At the basis of the strategy is the introduction into the system actuation of a positive feedback signal frequency independent, which is equivalent to a spring with repulsive stiffness and competes with the mechanical spring constant to lower the overall stiffness of the mode. The control loop topology is shown in fig.5.6. The transfer function at closed loop is:

$$\frac{x(s)}{x_0(s)} = \frac{G(s)\,(1-k)}{1 - kG(s)}. \tag{5.29}$$

Assuming a simple pendulum physical plant response like

$$G(s) = \frac{\omega_0^2}{\omega_0^2 - \omega^2} \tag{5.30}$$

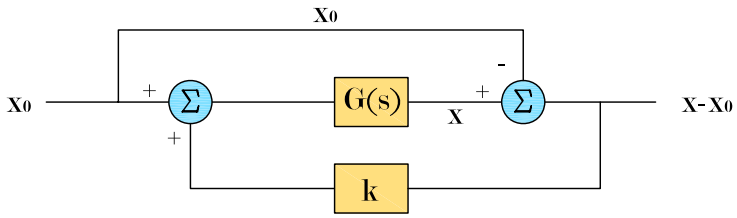

Figure 5.6: Electromagnetic Anti-Spring (EMAS) control loop. A pure gain, frequency indipendent, is fedback into the system to reduce the stiffness.

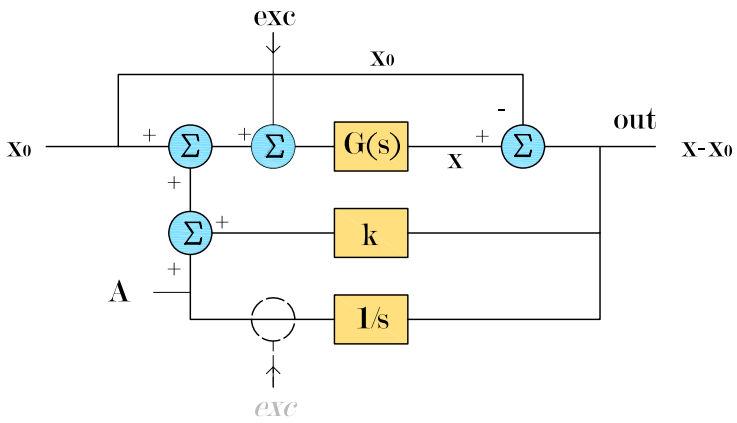

Figure 5.7: Scheme of the control configuration for the measurement of the physical plant as modified by the introduction of the EMAS. The precise measurement would be given exciting after the integrator and measuring the ratio out/A. Since the test points are only in some fixed locations according to the the front end code, the best possible measurement is made exciting right before the physical plant G from the ratio A/exc. This ratio well approximates G' except for the DC value.

the closed loop transfer function becomes

$$G_{\mathrm{c.l}}(s) = \frac{\omega_0^2\,(1-k)}{\omega_0^2\,(1-k) - \omega^2} \tag{5.31}$$

which is equivalent to a system with a reduced resonant frequency

$$\omega_0^{'} = \omega_0\,\sqrt{1-k} \tag{5.32}$$

that is to a system with a reduced stifness.

In order to measure the new physical plant response including the effect of the EMAS we followed the scheme in fig. 5.7. The table has always to be at the working point height, thus a position control must be included in parallel to the anti-spring. Ideally, the precise way to measure the new plant $G^{'}$ would be exciting right after the integrator and then it would be $G^{'} = \mathrm{out}/A$. Since EPICS

allows only a limited number of test points, one has to find the best location into the system's map to measure the transfer function. According to the front end code and to the available test points the closest thing to G' that we could measure was A/exc. This ratio well approximates G' for low gain of the integrator but it still differs for the DC value. The result of one of this kind of measurement for the z emas is shown in fig.5.12.

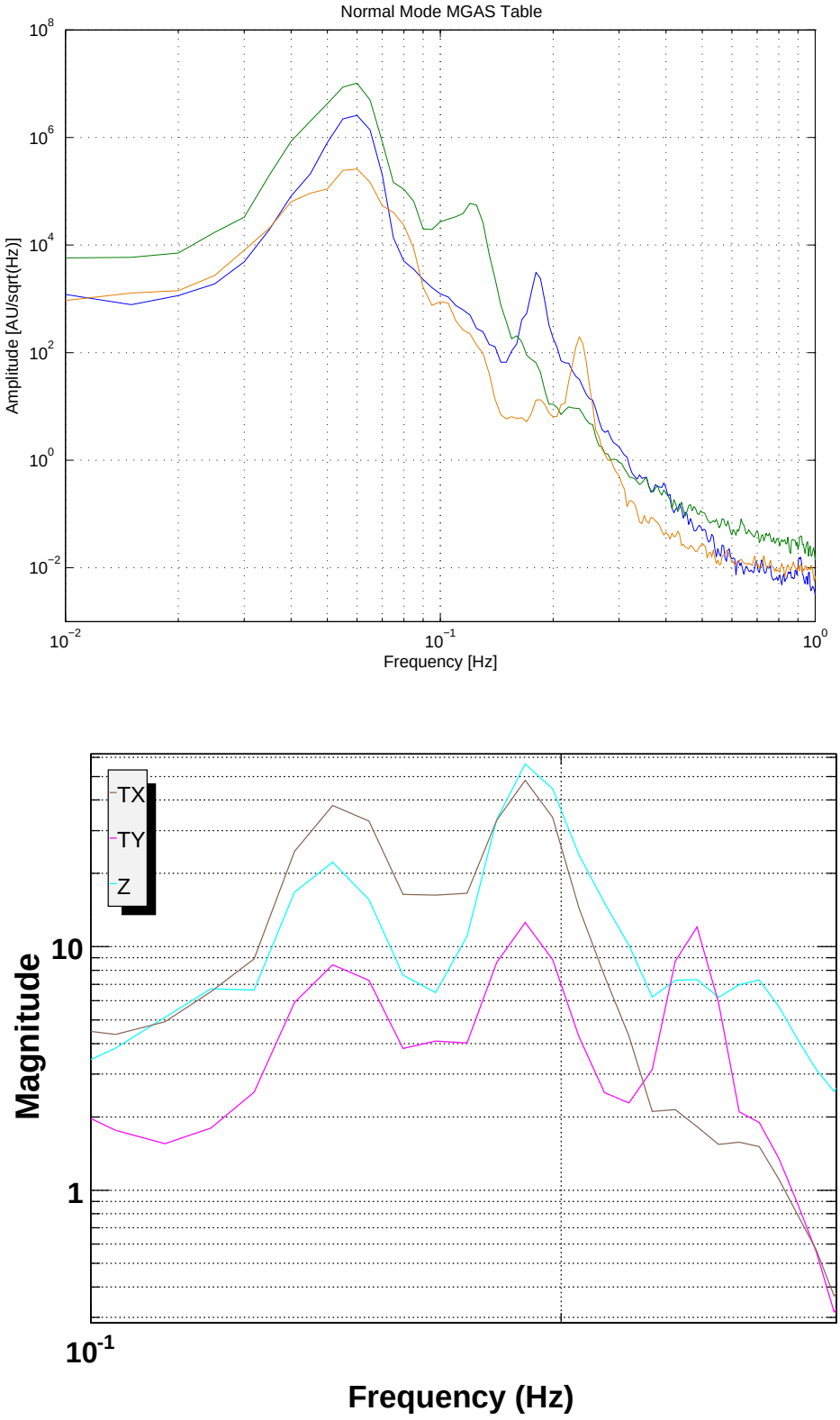

Figure 5.8: Modal vertical LVDT power spectra. The upper plot shows the signals from the virtual sensors after the diagonalization. Each sensors senses much more only one of the three resonances. Still, mostly on the first two resonances a little of coupling persists. The lower plot shows the spectra from the virtual sensors before the diagonalization, when they were aligned to the geometrical directions. The plots refer to an early configuration of the system when the resonances were at slightly different frequencies and the LVDT still not calibrated.

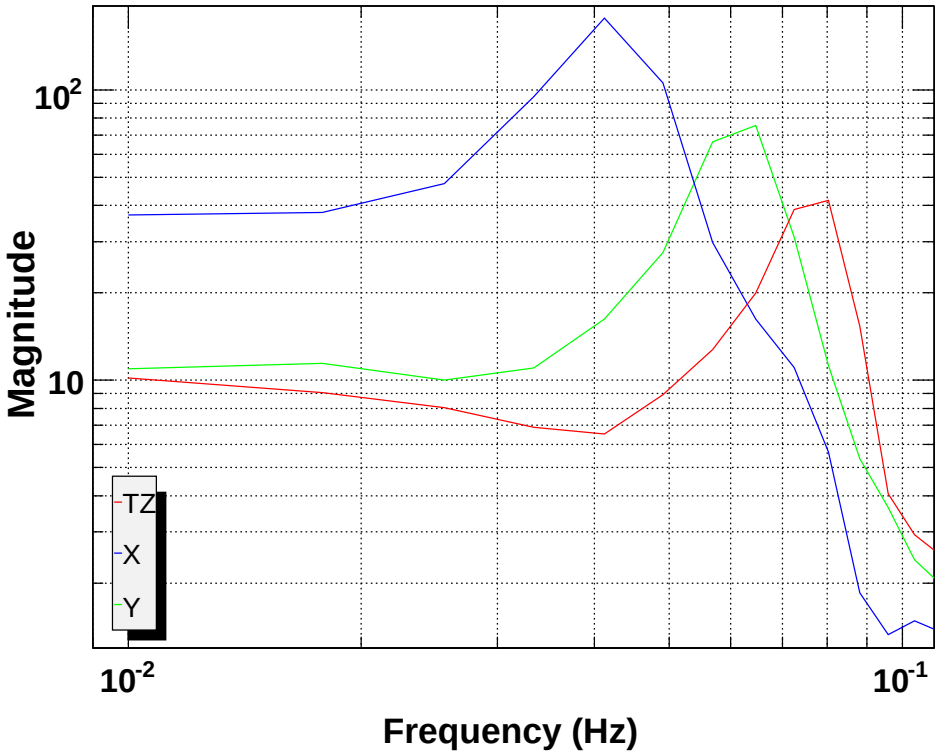

Figure 5.9: Modal horizontal LVDT power spectra. In this case the diagonalization of the sensors is very good and the three virtual sensors sense almost only one mode each.

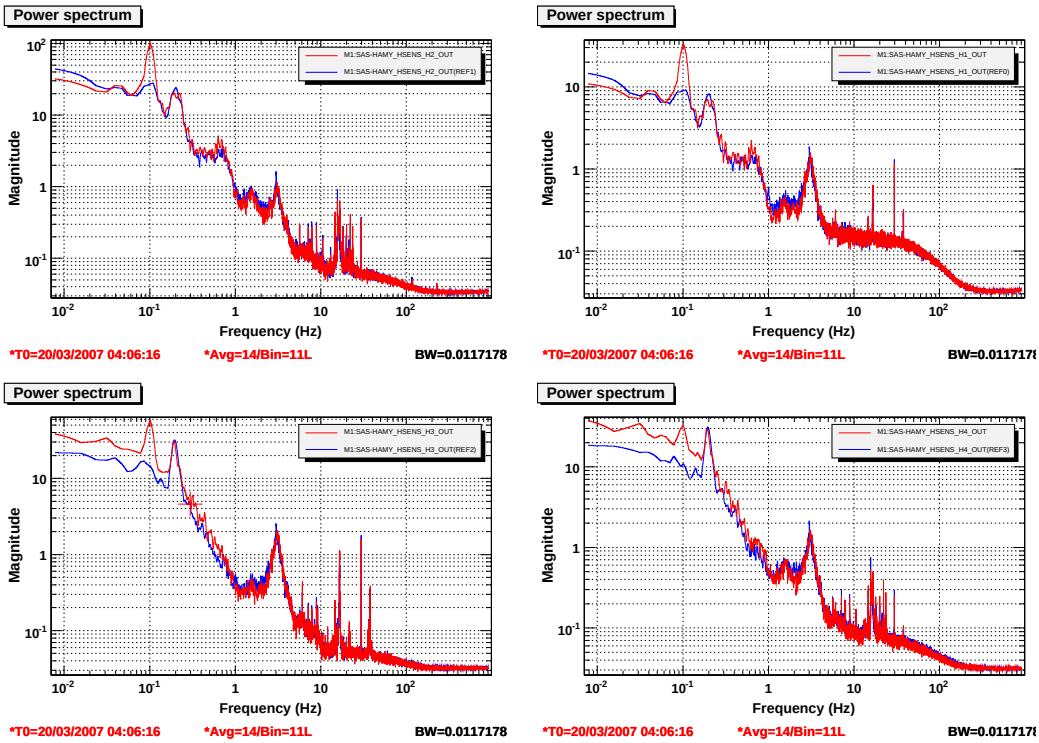

Figure 5.10: The plots show the horizontal LVDTS before (red curves) and after (blu curves) closing local damping control loops on each horizontal actuator (each actuator is controlled indipendently by the others). The sensors were not calibrated yet and the optics table was mechanically locked.

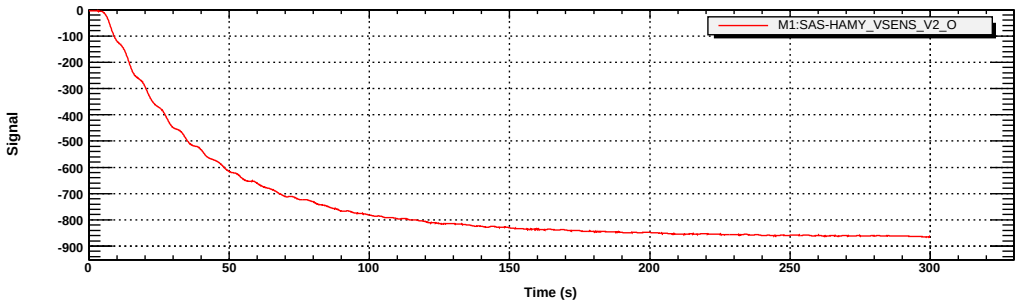

Figure 5.11: The plot shows the position control while it brings the table position as read by one of the vertical LVDT to a given position.

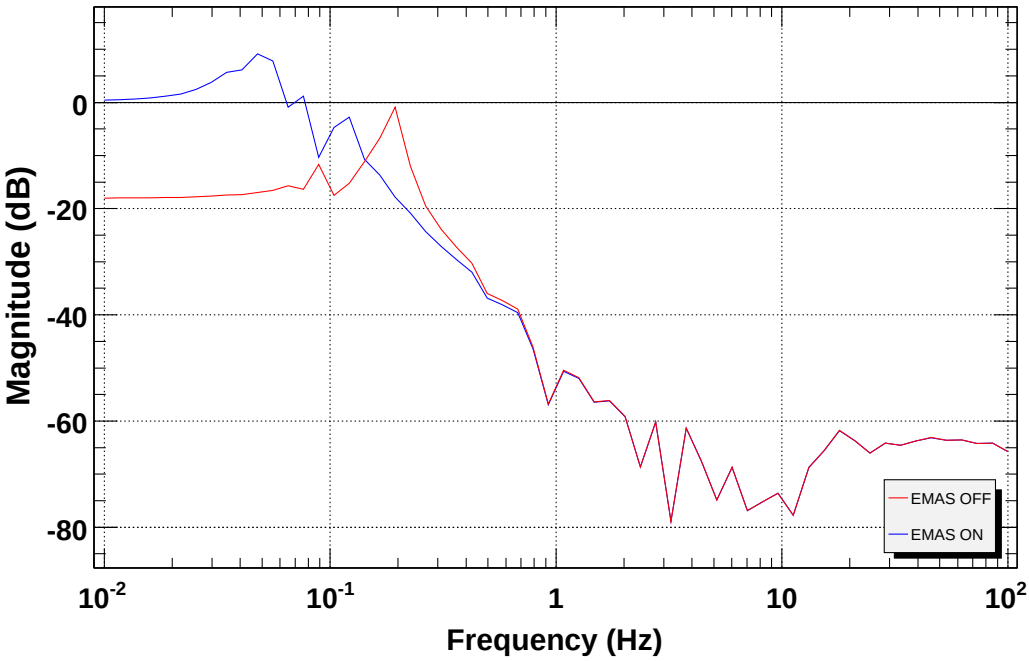

Figure 5.12: The plot shows the effect of an EMAS control applied to the Z mode with $k_{\mathrm{EMAS}} = 7$. The frequency is shifted from about 200 mHz to about 40 mHz. The blue (with EMAS) and red (with EMAS) have different DC values because of the way the modified physical plant response is measured according to the available EPICS test points.

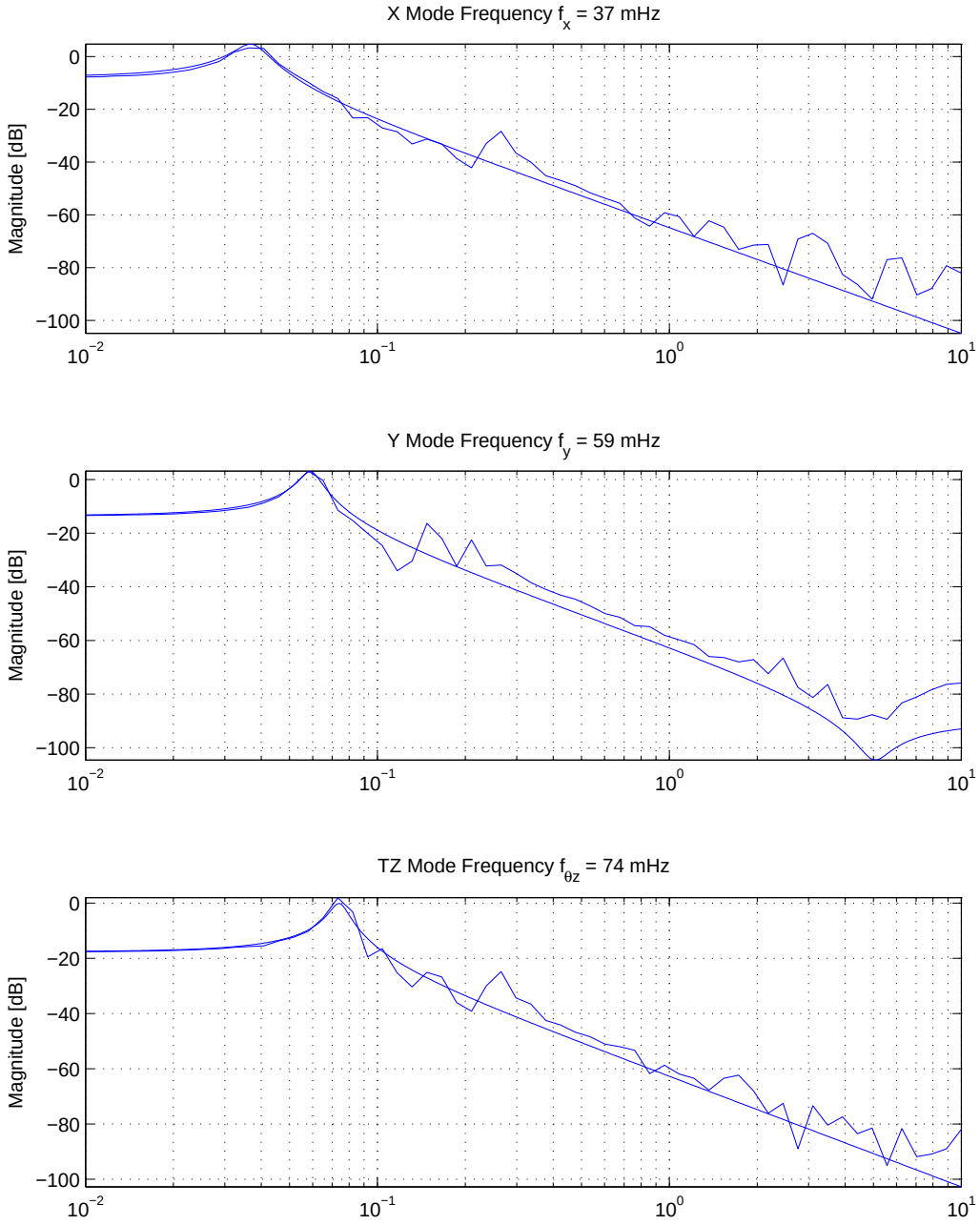

Figure 5.13: Diagonal transfer functions for the horizontal degrees of freedom fitted by a pendulum function.

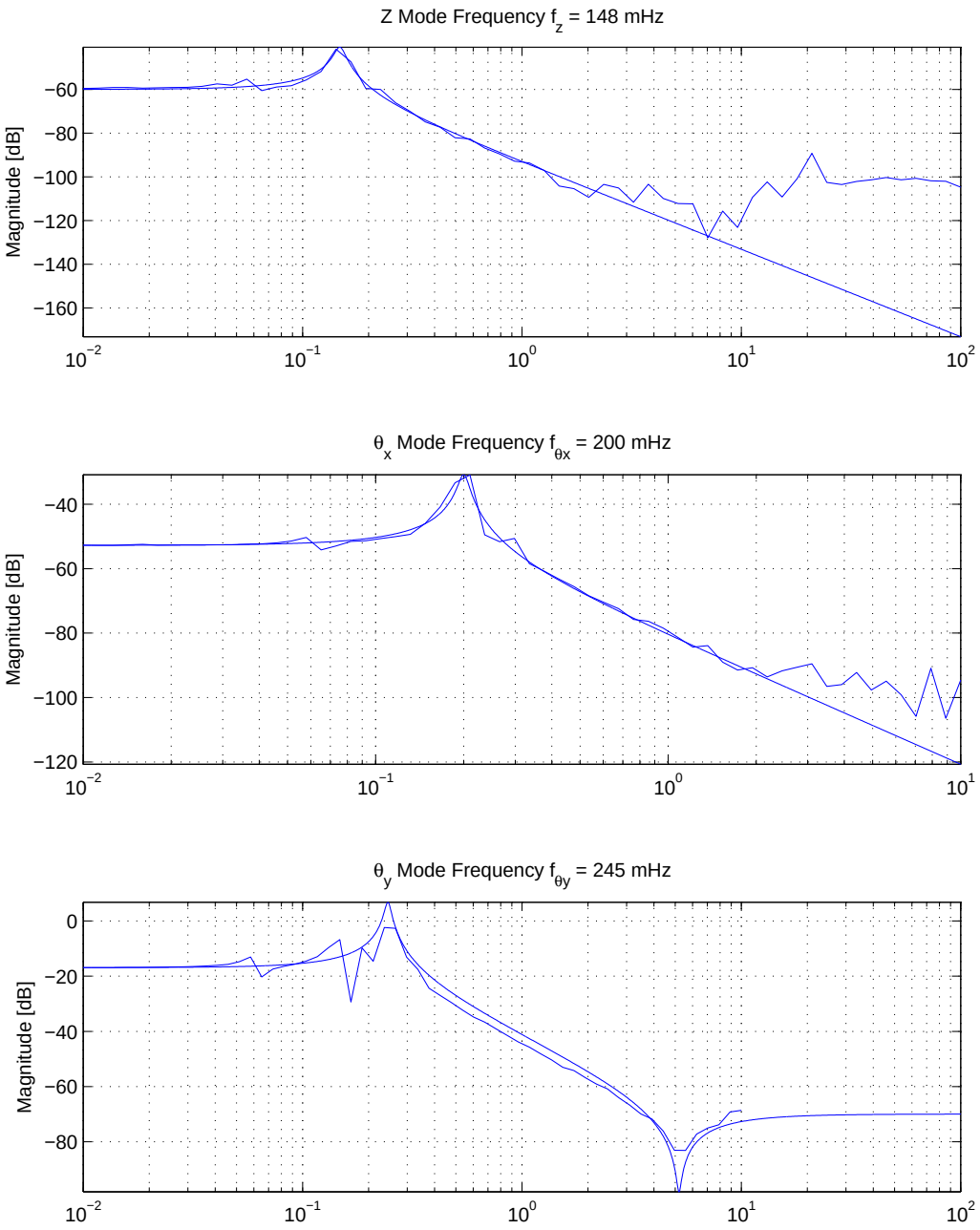

Figure 5.14: Diagonal transfer functions for the vertical degrees of freedom fitted by a pendulum function.

Chapter 6

System Performances

In this chapter we present the latest experimental results from the HAM-SAS experiment. First we introduce the quantities by which we measured the performances of the system. We discuss the attenuation performance achieved, the strategy adopted for the controls and the issue about the very low frequency displacement noise observed.

6.1 Measuring the HAM-SAS Performances

Before discussing the performances of the system, we want to clarify the definitions and the properties of the quantities that we are going to consider. Since we are here interested in seismic attenuation performances, the observable that we have in mind is always a coordinate position.

6.1.1 Power Spectrum Densities

Be $x(t)$ the coordinate describing the system in the time domain [16]. Its *power spectrum density* is defined as the Fourier transform

$$P_x(f) = \frac{1/\sqrt{2\pi}}{x * x(0)} \int_{-\infty}^{+\infty} x * x(\tau)(\tau)\ e^{-2\pi i\omega t} d\tau \tag{6.1}$$

in which $x * x(\tau)$ is the *autocorrelation function* of $x(t)$ which is defined as:

$$x * x(\tau) = \int_{-\infty}^{+\infty} x(t)\, x(t+\tau)\, dt \tag{6.2}$$

From Parseval's theorem the *root mean square* value of x is connected to the power spectrum by:

$$x_{\text{r.m.s.}} = \sqrt{\int_{-\infty}^{+\infty} P_x(f)\, df} \tag{6.3}$$

We rather work with an object derived from the power spectrum: the *amplitude spectral density*[1]. It is simply defined as the square root of the power spectrum:

$$S\,(f) = \sqrt{P_x\,(f)}. \tag{6.4}$$

and its dimensions are $[x]/\sqrt{Hz}$. The advantage of this object is that the unit matches better what we measure with the sensors (i.e. meters).

The spectrum measurements on HAM-SAS data have been made with an FFT Matlab based software tool, averaging over many measurements. The averaged spectra are accompanied by the root mean square of the measurement, intended as the standard deviation on the points j of the set at frequency i:

$$S_{\text{r.m.s.}}(f_i) = \sqrt{\frac{1}{N}\sum_{j=1}^{N}\left(\bar{S}\,(f_i) - S_j(f_i)\right)}. \tag{6.5}$$

The spectrum r.m.s. represents a useful parameter for the evaluation of the measurement noise.

6.1.2 Transmissibility and Signal Coherence

The particular transfer functions in which both the input and the output quantities are dynamic variables as position, velocity or acceleration are called transmissibilities. We evaluated the seismic performance of HAM-SAS measuring the transmissibilities of the system for each degree of freedom. They were obtained simply dividing the Fourier transform of the output signal from the geophones on the optics table by the input signal from the Guralp seismometers on the ground, both of them corresponding to the same degree of freedom.

Experimentally the input and output of a transmissibility measurement can be disturbed by noise and the ratio between the two relative spectra does not necessarily represent the transfer function of the system. In LTI system theory (Linear Time Invariant), it can be demonstrated [48] that two signal $x\,(t)$ and $y\,(t)$ are correlated if and only if it is possible to define a function $H\,(t)$ such that:

$$y\,(t) = H\,(t) * x\,(t) \quad \Rightarrow Y\,(\omega) = H\,(\omega)\,X\,(\omega)\,. \tag{6.6}$$

To evaluate the quality of the measured ratio between the two spectra as actually representing the transfer function, for the measurements on HAM-SAS, we have considered the *coherence* function to evaluate the correlation between the signal. The coherence $C_{xy}\,(\omega)$ between x and y is defined as

$$C_{xy}\,(\omega) = \frac{\left|R_{xy}\,(\omega)\right|^2}{X_x\,(\omega)\,Y_y\,(\omega)} \tag{6.7}$$

[1] Although we often improperly refer to it as power spectrum or just spectrum.

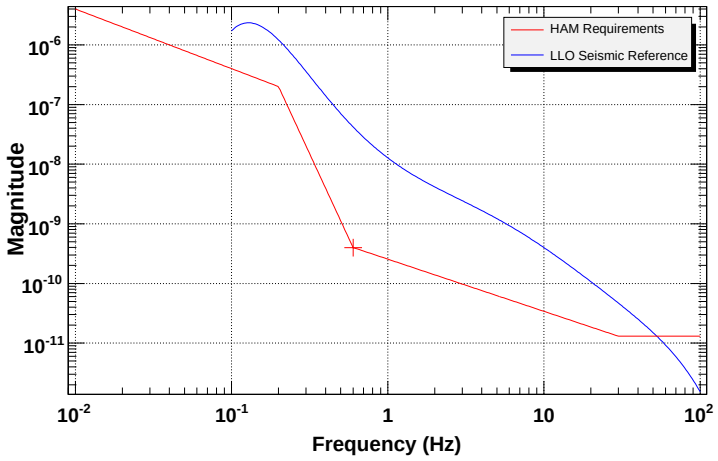

Figure 6.1: Advanced LIGO HAM requirements for the displacement noise of the Power Recycling and Output Mode Cleaner and model of Livingston seismic power spectrum.

where $R_{xy}(\omega)$ is the Fourier transform of the cross-correlation function between x and y, defined as

$$R_{xy}(\tau) = x * y(\tau). \tag{6.8}$$

The coherence is a real function between zero and one. It is one if x and y are correlated. On the other hand, when x and y are uncorrelated (i.e., y is a noise process not derived from x), the coherence converges to zero at all frequencies.

6.2 Evaluating the Seismic Performances

The Advanced LIGO HAM requirements [49] set a reference to evaluate the HAM-SAS seismic performances and they represented the ultimate goal of the system commissioning. In particular the constraints for the Power Recycling and Mode Cleaner optics set a displacement noise limit of $2 \times 10^{-7}\ m/\sqrt{Hz}$ in the 0.1-0.2 Hz band, $4 \times 10^{-10}\ m/\sqrt{Hz}$ at 600 mHz and $3 \times 10^{-11}\ m/\sqrt{Hz}$ above 20 Hz (fig.6.1). The conditions have been defined according to a model of the ground seismic spectra at both of the sites, Hanford (LHO) and Livingston (LLO) [50]. The horizontal and vertical ground noise are considered equal and expressed, in the frequency range $100mHz < f < 40Hz$, as a polynomial expansion in log space:

$$\log x_g(f) = p_1 (\log f)^n + p_2 (\log f)^{n-1} + \ldots + p_n \log f + p_{n+1} \tag{6.9}$$

where x_g is the displacement spectral density. Because the average ground noise at the two observatories and at MIT differ significantly, three separate ground noise

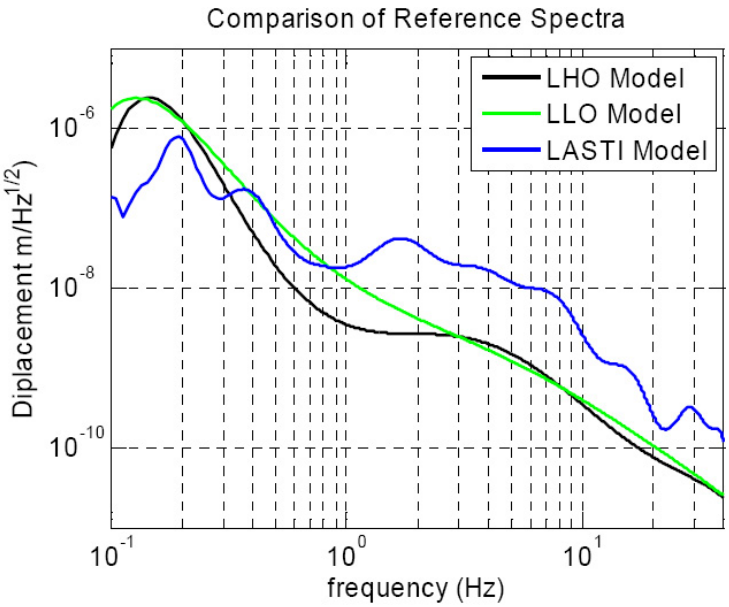

Figure 6.2: Ground noise models for the Hanford (LHO), Livingston (LLO) and LASTI sites. Each curve was obtained by a polynomial fit of the seismometer data. The plot shows LASTI as a noisier location than the sites in the horizontal and vertical DOF.

models are estimated for LHO, LLO and LASTI; these are shown in fig.6.2. In the models the ground noise input is assumed to be the same for all three translational degrees of freedom.

6.3 Experimental Results

We want here to show and discuss some of the latest power spectra and transmissibilities which illustrate the status of the system performances in the present configuration.

As we explained in chapter 5, the roles of the control system are two: to keep the platform at the working point in order to have the best passive isolating performance and to actively assist the mechanics in attenuating the seismic noise. We will see here the effect of these different strategies.

6.3.1 Passive Attenuation

As explained in chapter 3, both the IPs and the GAS filter were set to perform at best at their correspondent working point[2]. Because of absolute and differential thermal drifts of the apparatus, ground movements and tilts (tidal movements, water table variations, movements of heavy loads on the floor and in the building vicinities, diurnal and seasonal differential heating and cooling of the facilities etc.)[3], only position control can guarantee and maintain a perfect alignment of the optical table. The very low tuning of the resonant frequencies exacerbates these drifts both in the vertical and horizontal directions.[4]. Misalignments can even bring to instabilities because of recoil effects between the spring box and the pendulums.

From the measured physical plant responses (see sec. 5.2.6), we designed static positioning control loops (DC) with a very low unitary gain frequency (u.g.f.) of about 1 mHz by which we obtained the power spectrum of fig. 6.3, basically leaving the system free to move at all frequencies .

The structure between 10 and 20 Hz is typical of all the measurements. It corresponds to a internal mechanical resonance of the system which we had no time to identify and damp. We believe it is likely due to either the tilt correcting springs or the wire by which they pull the central column. When the HAM chamber was still open, it was in part, but not totally, attenuated by magnetic dampers (see fig.6.4). It is expected to be fixed with properly designed dampers and/or redesigned springs.

Below about 400 mHz the transmitted seismic motion of the uncontrolled system amplitude becomes higher than the requirements, especially for x, and under 100 mHz, where the horizontal displacement becomes greater than 1 μm/ $\sqrt{\text{Hz}}$. In particular we notice three peaks between 100 and 300 Hz correspondent to the resonances of the vertical DOFs. These resonances enter in every degree of freedom because of couplings between different degrees of freedom. They actually cause a larger appparent displacement in the horizontal than in the vertical. The actual coupling originates likely in recoil effects between the spring box and the optics table. It must be considered that the table with all its payload has a mass which is three times that of the spring box and the center of mass is located 50 cm over the pivot point of the GAS filters. The mechanical solution foreseen for

[2] As part of the lower frequency tuning process, optimization of the GAS system would have required a complete frequency versus load scan of the vertical degree of freedom, to set the payload at the GAS minimum frequency point. Even this step was not performed for lack of time.

[3] The effects of creep [47] in the SAS structure have been neutralized by prolonged baking under load after assembly.

[4] This, as well as time constraints, is the reason why, in absence of working controls of the static positioning, in the first implementation we chose a conservative tune of both GAS filters and the IP table, at twice or more of achievable frequencies.

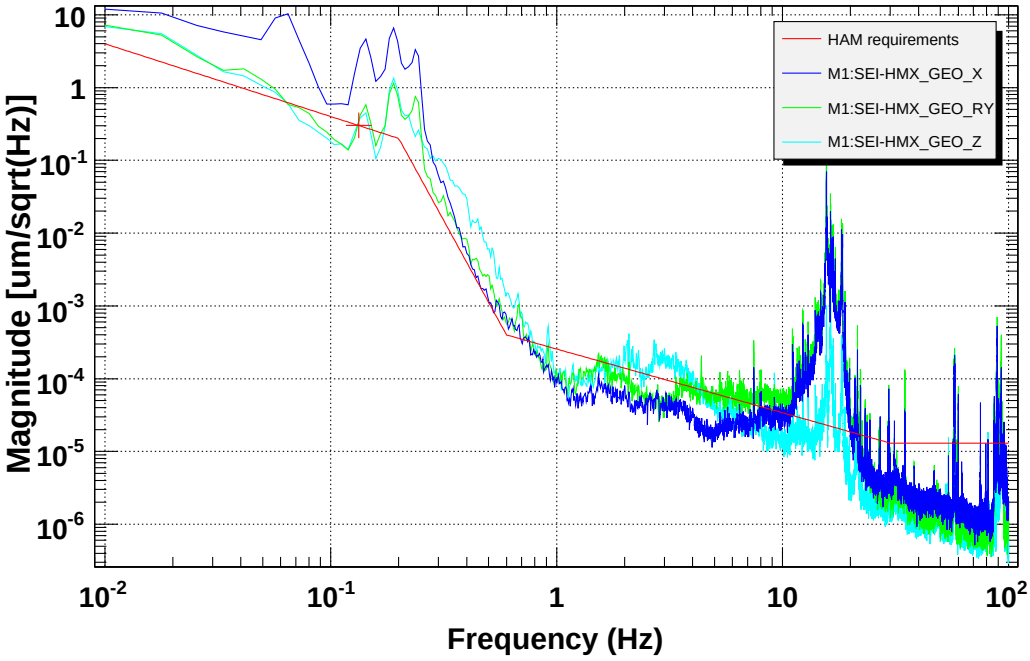

Figure 6.3: Optics table displacement power spectrum of the x, z and yaw (θ_z) degrees of freedom. Only weak DC control loops are closed. The straight line is the HAM requirement refernce. The spectrum can be considered as a measurement of the passive performance of HAM-SAS.

this problem is to implement a lower tuning of the vertical frequencies, by an additional compression of the GAS filters' blades (or by EMAS control), until the natural larger damping at lower frequency neutralizes these resonances.

As already pointed out in sec. 4.2.3, the geophones are inertial sensors and thus affected by tilt-to-horizontal coupling. For this reason in x and y spectra, especially at low frequency, where we suspect the effect to be more important, we cannot distinguish between the actual horizontal motion and what is angular motion of the vertical DOFs sensed as horizontal motion. Under 100 mHz the measurements from the geophones have then to be considered with that caveat. As explained in sec. 4.2.3, the tilt contribution could be subtracted out of x if we had an independent and reliable measure of it. The tilt signal is useful for subtraction from the horizontal signal if it is coherenthas coherence with the horizontal signal. But neither the tilt measured by the vertical geophones (i.e. R_y in fig.6.3), nor the optical lever were found to be coherent with the horizontal signal. For the geophones the reason is that their sensitivity decreases significantly below 100 Hz whereas a very high accuracy would be needed to measure a tilt angle from the

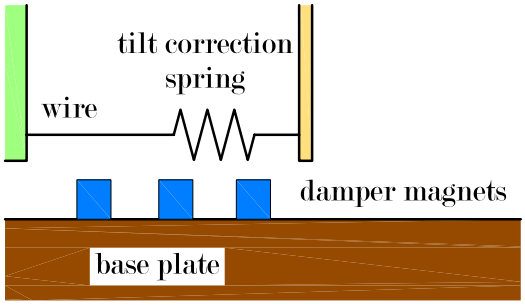

Figure 6.4: Damper magnets installed to attenuate the wire and tilt correction spring's resonance.

difference of two vertical signals[5].

6.3.2 Getting to the Design Performances

The HAM SAS mechanics is equivalent to that of an extremely large seismometer. Its mass is basically completely inertial at high frequency, while in the low frequency band it moves around under the influence of tilt for the horizontal direction and in a way which is also affected by the hysteresis of the materials used to build its flexures. Like the mass of any horizontal accelerometer, the dominant fraction of its horizontal residual motion is excited by ground tilt. Ideally, this sort of random motion, in absence of any damping mechanism, would be enhanced indefinitely as the resonance frequencies are tuned toward zero frequency[6]. If a suitable evaluation of the ground tilt were available, the part induced by the tilt of the residual motion could be eliminated by feed-forward controls[7].

Without any closed loops on the system, the LVDT signals from HAM SAS are equivalent to those of an array of seismometers (fig.6.5). Then the control strategy consists in having no control at high frequency, where its attenuation performance corresponds to the sensitivity limit of seismometers and geophones, and to reduce the residual motion by tying the system to ground at the lowest frequencies by means of LVDT signal feedbacks. The LVDTs, being relative position sensors, are not directly influenced by tilts. Important is the choice of of filters and of the optimal u.g.f. to avoid feeding LVDT and actuation noise to the high frequency side, where the performance is already equivalent to that of an

[5]This is basically the same reason why it is not easy to have reliable tilt-seismometer sensors.

[6]The limit case, for zero frequency tune, is that of a mass on a completely frictionless table, which would move to infinity for even the slightest table tilt

[7]The feed-forward filtering is an alternative for feedback for the seismic noise attenuation when a signal correlated to the noise is available. The idea is to produce a secondary noise source such that it cancels the effect of the primary noise at the location of the error sensors.

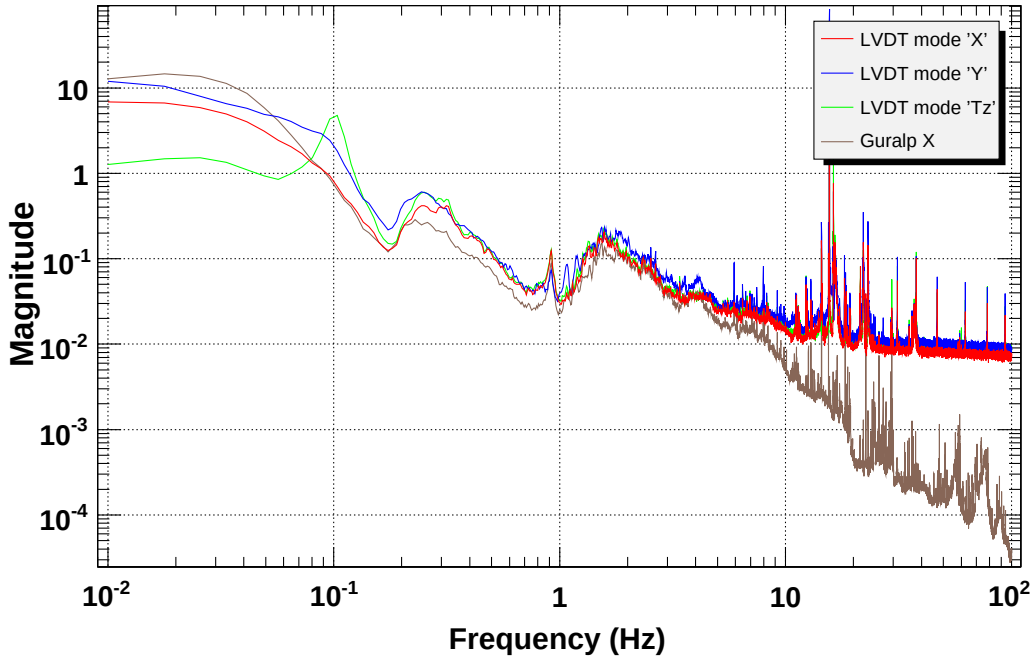

Figure 6.5: The Guralps' and the LVDTs' signal match at high frequency. HAM-SAS and the optics table can bee considered as afree mass in that range and thus the relative position signal from the LVDTs follows the ground movement. (The unit on the Y-axis is $\mu m/\sqrt{Hz}$).

ideal seismometer. The process is analogous to, and shares the same noise sources of an active attenuation system, where the signal of position sensors is used to stabilize the r.m.s. displacement at the lowest frequencies, and which is blended into the signal of the best available seismometer above a critical frequency. In both active and passive systems the amount of low frequency r.m.s. residual motion is determined by the u.g.f., and in both systems the horizontal residual motion can ideally be reduced by means of tilt meter signals.

The low frequency seismic residual motion can be amplified by the quality factor of the mechanical resonances of the system. The effects of these resonances in SAS can be eliminated in two ways. The resonances can be damped - like in most seismometers - by electromagnetic damping, or by driving the motion resonances sufficiently low in frequency that the quality factor drops. If the quality factor becomes smaller than 1, the system is completely dominated by tilt and by the internal forces in its flexure materials.

SAS has two ways to control its resonant frequencies. First the frequencies are minimized mechanically, by increasing the load of the IP tables and the radial compression of the GAS filters as close as possible to the critical point. This

process is practically limited only by the onset of hysteresis. After getting to the limits of the mechanical tuning, the resonance frequencies can be further reduced by means of the electromagnetic spring control system (EMAS)[8]. Since strong EMAS can reintroduce control noise, it is first important to mechanically minimize the frequency resonances[9]. An other benefit of minimizing the resonant frequencies is that the actuator authority requirements are reduced, and thus also the noise re-injection due to the electronics.

6.3.3 Lowering the Vertical Frequencies

It is know that for oscillators at very low frequency hysteresis becomes an important effect and that the quality factor scales with the square of the frequency (see sec. 2.3.5, [53]). Thus we implemented the Electro-Magnetic Anti-Spring (see sec.5.3.4) controls system to the vertical degrees of freedom with the purpose to damp the vertical resonance and to increase the attenuation factor. Figure (6.6) shows the results of this strategy. The vertical frequencies are all shifted below 100 mHz and the vertical power spectrum easily meets the requirements. All the resonant frequencies of the six modes are then concentrated in the low frequency region. As a consequence the effect of the coupling between the horizontal and the vertical DOFs and tilt became more and more important the measured horizontal displacement exceeds the requirements.

We tried to damp the resonances at low frequencies with damping control loops in every DOF but the price for an appreciable reduction of the horizontal displacement was a large control bandwidth and then a significant noise re-injected above 1 Hz.

Also, the EMAS made the system less stable and a small environmental change like a person walking close by the HAM chamber could trigger an instability in the loops.

6.3.4 Active Performance

We found that the best performance can be achieved with only position controls and damping controls in parallel, tuned in order to have u.g.f. between about 0.5 and 1 Hz. Optimizing the gains and the bandwidth for each loop, we ensured the stability and reduced the noise re-injection at high frequency as much as possible (fig. 6.8). The results for x and z are shown in fig.6.11.

[8]The EMAS springs are a more complex system, but have the advantage that they can be easily coupled with very low u.g.f. static positioning feedback, to counter the otherwise dominating hysteresis effects.

[9]In the present tests the mechanical tuning was halted roughly twice above previously achieved levels

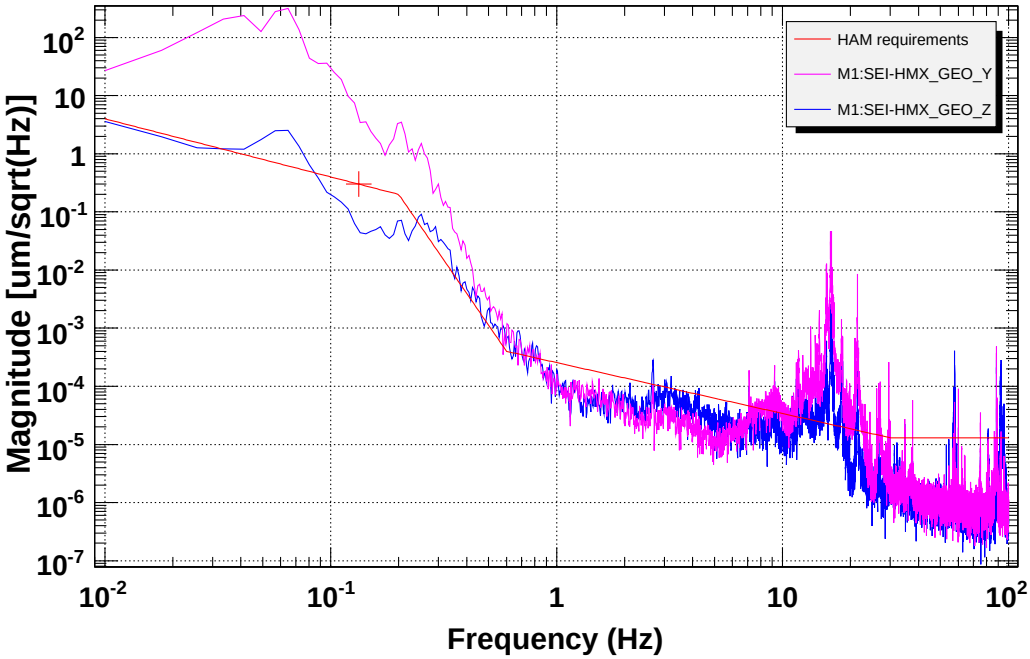

Figure 6.6: Electromagnetic Anti-Springs are applied to move the vertical resonances to lower frequencies in order to reduce their quality factors and lower in frequency the onset of the attenuation rolloff. The strategy succeeded for the vertical DOFs although all the 6 modes were then located in the range of few tens of mHz where they inter-couple. As a result the detected horizontal displacement increased.

The power spectra for the vertical direction meets the requirements in all range of frequencies, except for a small residual peak still present in correspondence of the vertical modes. The horizontal displacements is in agreement with the requirements as well, except for the very low range where, as we already pointed out, the geophones are not reliable in the horizontal directions because of the tilt-to-horizontal coupling. It must be said that we found no coherence with the tilt measurements as obtained from the optical lever (fig.6.9).

With this minimal control strategy applied (figg.6.7,6.7), we measured the transmissibilities between the ground seismometers and the geophones on the optics table (fig.6.12,6.13,6.14). Within the limits given by the coherences, the transmissibilities show attenuation factors of -70 dB in the horizontal degrees of freedom and of -60 in the vertical. These values correspond to the design and simulations performances.

The experience with SAS systems ([15], [23]) makes us confident that, with more reliable sensors and seismometers and the applications of the other subsystems like the COP correction counterweights on the IPs and of the “magic

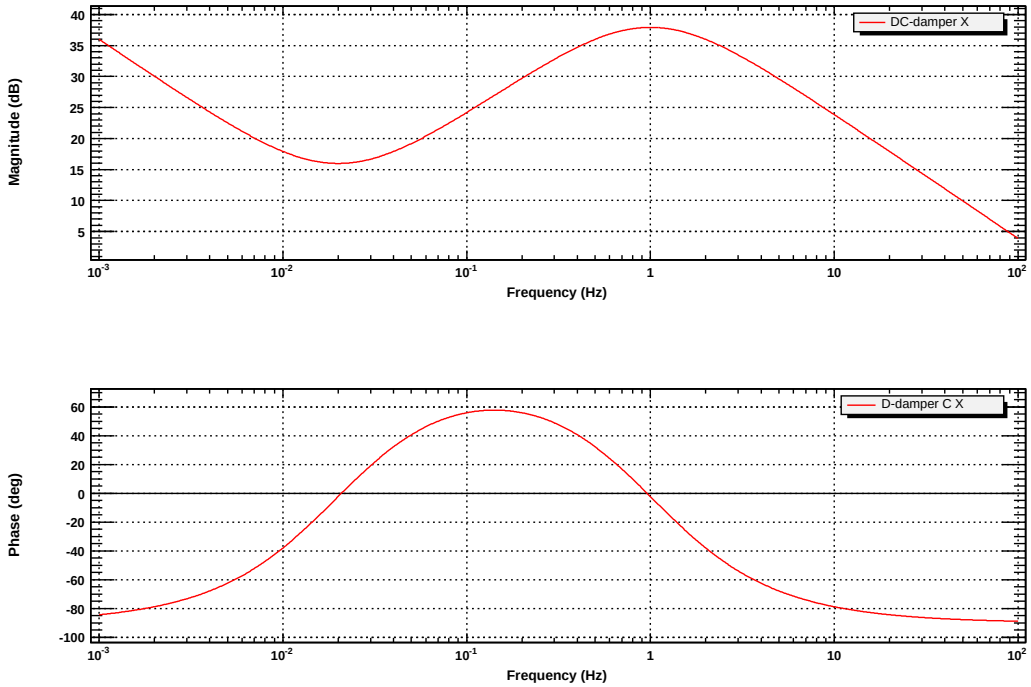

Figure 6.7: The plot shows the transfer function amplitude and phase of the position and damping combined control for the horizontal mode X that we applied to obtain the performances which met the seismic attenuation requirements. The same filter shape, but with different gains and locations of poles and zeros adapted to the specific physical plant responses are applied to the other modes.

wands" on the GAS filters, these performance could be extended to -100 dB in the horizontal DOF and -80 dB in the vertical while minimizing the low frequency r.m.s.residual motion at the same time.

6.4 Ground Tilt

Even if the displacement noise at very low frequency can be significantly attenuated by the damping controls, the source of much of the measured horizontal geophone noise still remains not definitely identified. The seismic noise measured by the seismometers does not explain it unless it comes from angular seismic noise, which the seismometers would not sense.

According to the model of section 2.4.2 the response of the IPs to the ground tilt is

$$x = \frac{A + B\omega^2}{A - C\omega^2} x_0 + \frac{k_\theta / l^2}{A - C\omega^2} \Theta \tag{6.10}$$

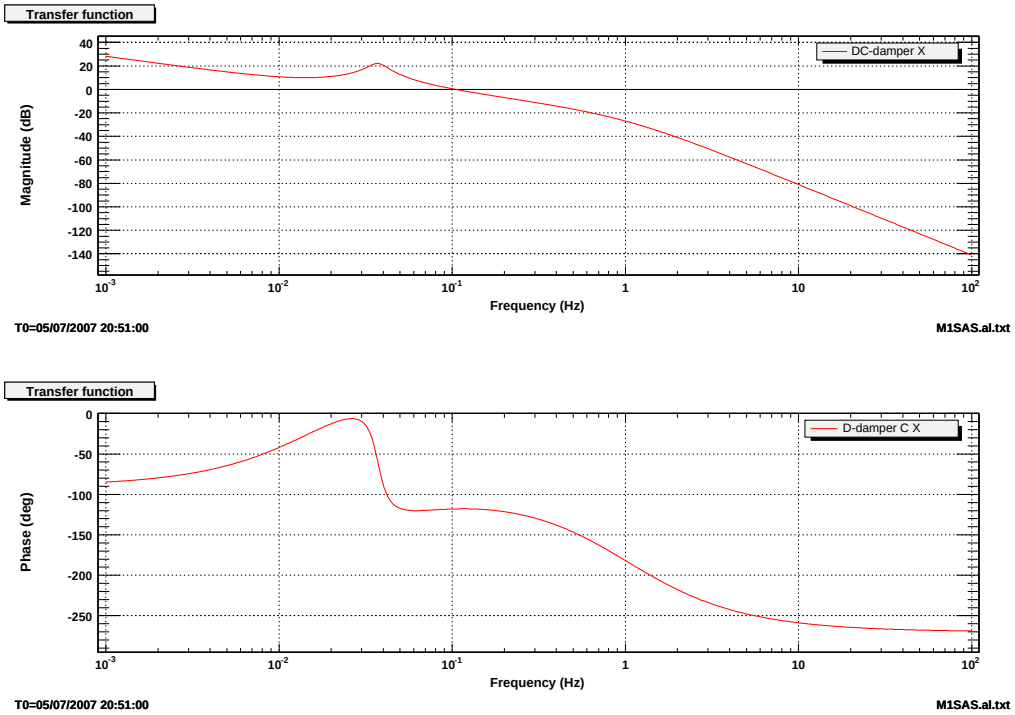

Figure 6.8: The plot shows the Bode plot of the open loop transfer function GC for the x degree of freedom. The same strategy is applied to all the DOFs. The u.g.f. is chosen as a trade off between the necessity to damp the low frequency resonances and the re-injection of high frequency noise. In this case u.g.f.=100 mHz.

where Θ represent the angular spectrum of the ground. Since direct and accurate measurements of the ground tilt do not exist, the classical model, very often adopted to have an estimation, relies on the Rayleigh waves propagation model. In it, as discussed in the first chapter, the ground tilt noise spectrum is proportional to the vertical component of Rayleigh waves divided by the propagation speed. As discussed in chapter 1, the coupling factor between the nominal ground tilt Θ and its translational motion X_0 varies from 10^{-3} to 10^{-1} rad/m and thus, ideally, the contribute should be negligible. However the model does not take into account local environmental factors like the wind and anthropogenic activities which can tilt the local structures (buildings) and are more likely to make the contribution dominant at very low frequencies. The experience from the HAM-SAS prototype and the seismic team at Virgo ([52]) reinforce that hypothesis, although the ultimate proof will come when reliable tilt-seismomters will be available. Both LIGO and Virgo are now strongly involved in the development of such sensors.

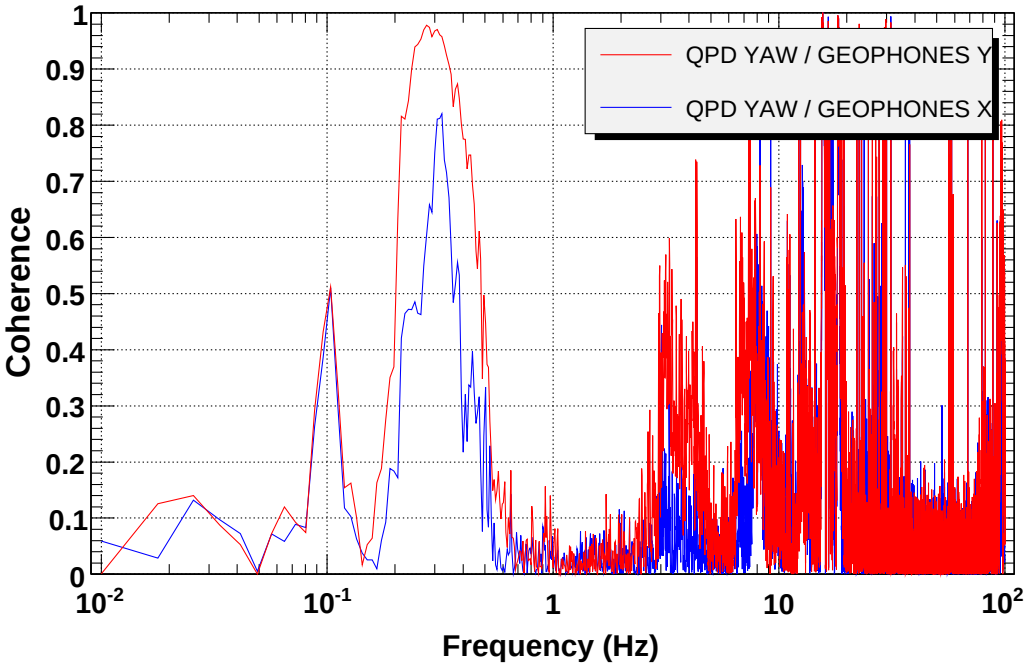

Figure 6.9: Coherence between the pitch as measured by the optical lever and the horizontal degress of fredom as measured by the geophones.

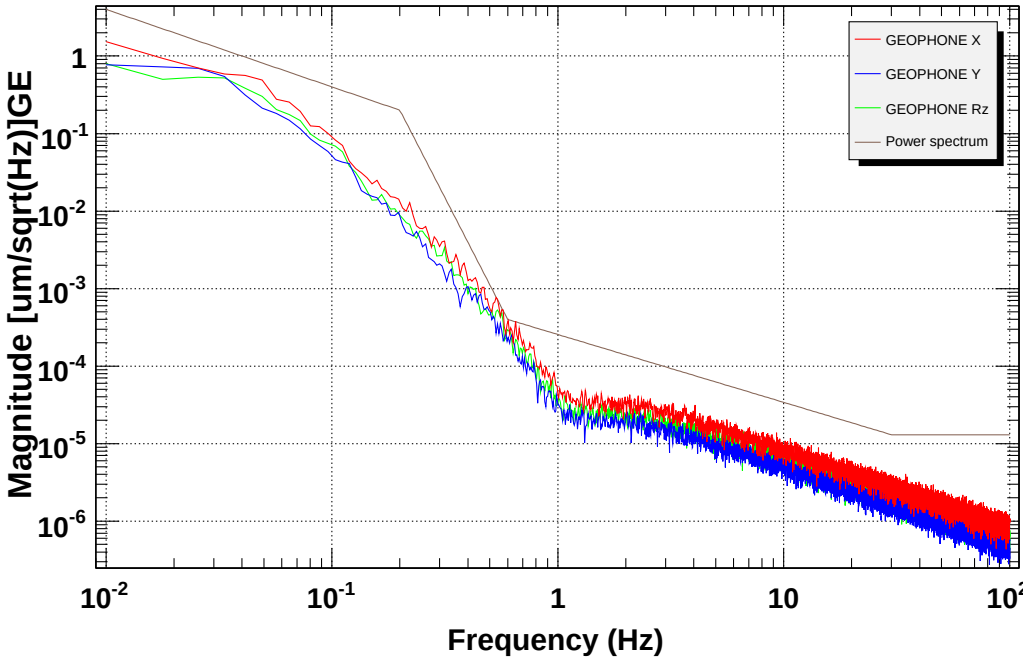

Figure 6.10: Geophones noise floor measured disconnecting the sensors from the readout board.

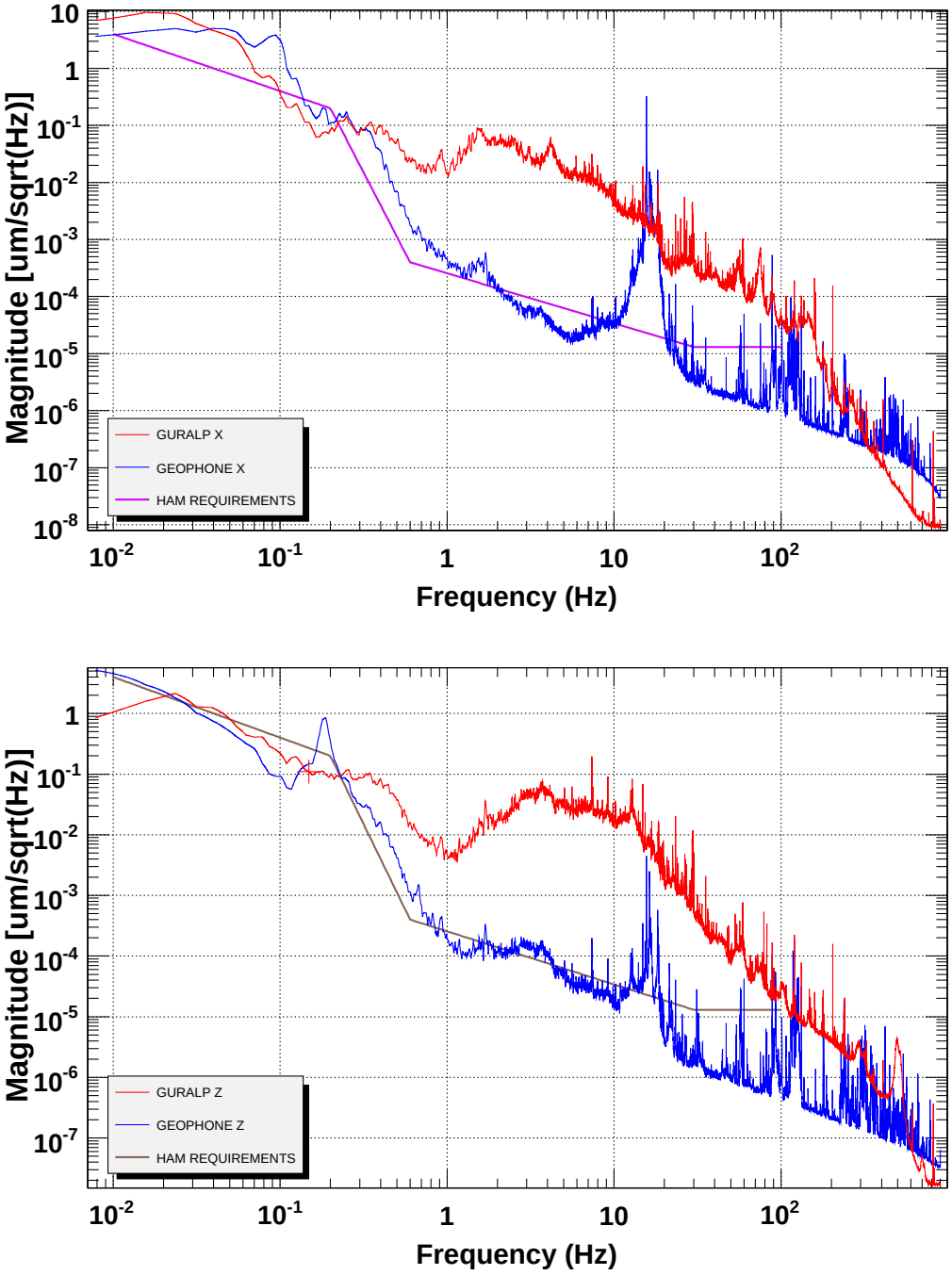

Figure 6.11: The plot shows the power spectrum on the x direction (upper plot) and of the vertical direction z (lower plot) each one compared with the reference given by the correspondent displacement spectra from the seismometers on the ground (red curves) and the HAM requirements. DC, damping and Resonance Gain controls are active.

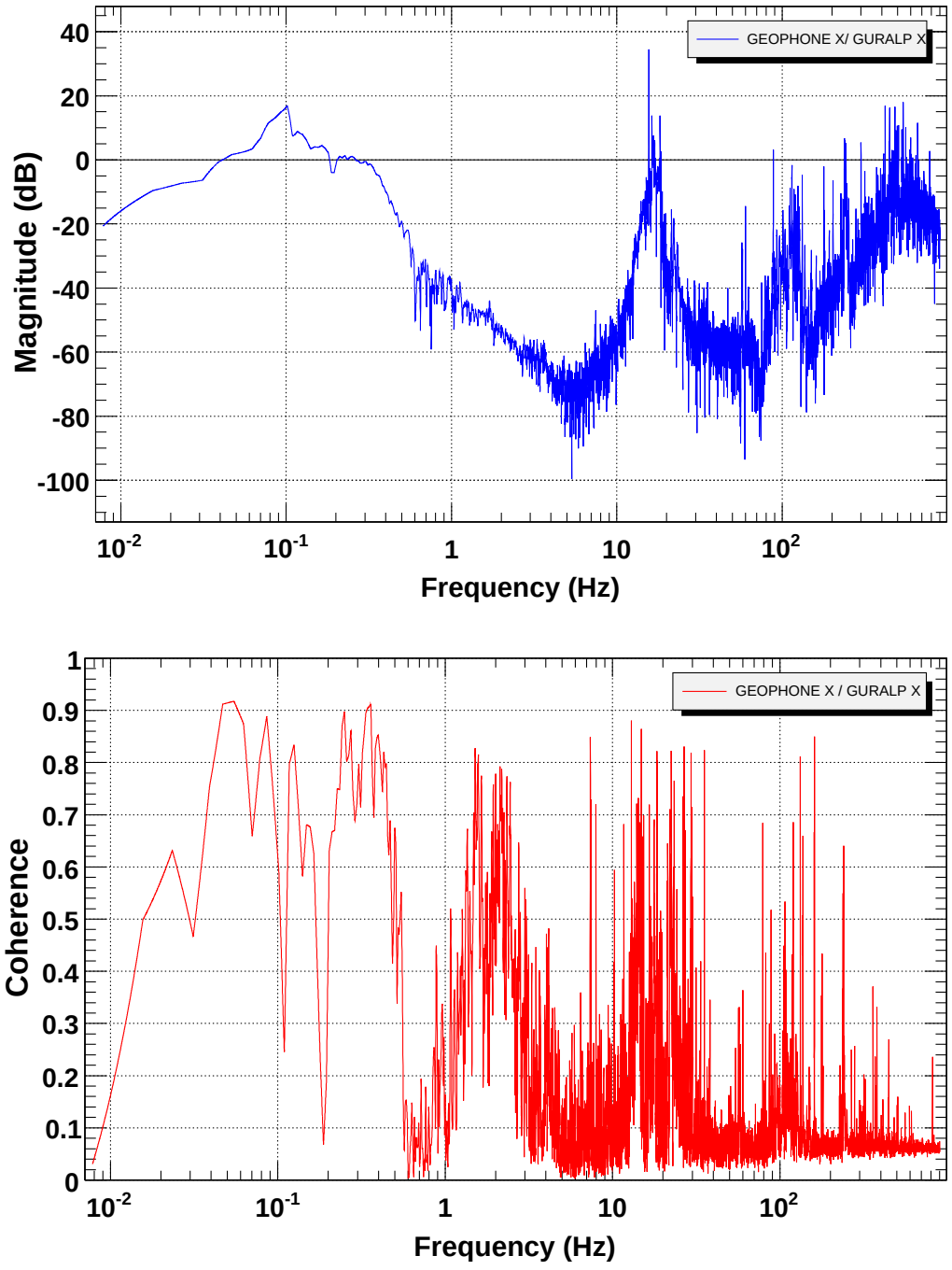

Figure 6.12: Active performance. Horizontal Transmissibility along x. The coherence is often low but -70 dB are reached at 4 Hz. The geophone noise floor is reached at about 20 Hz

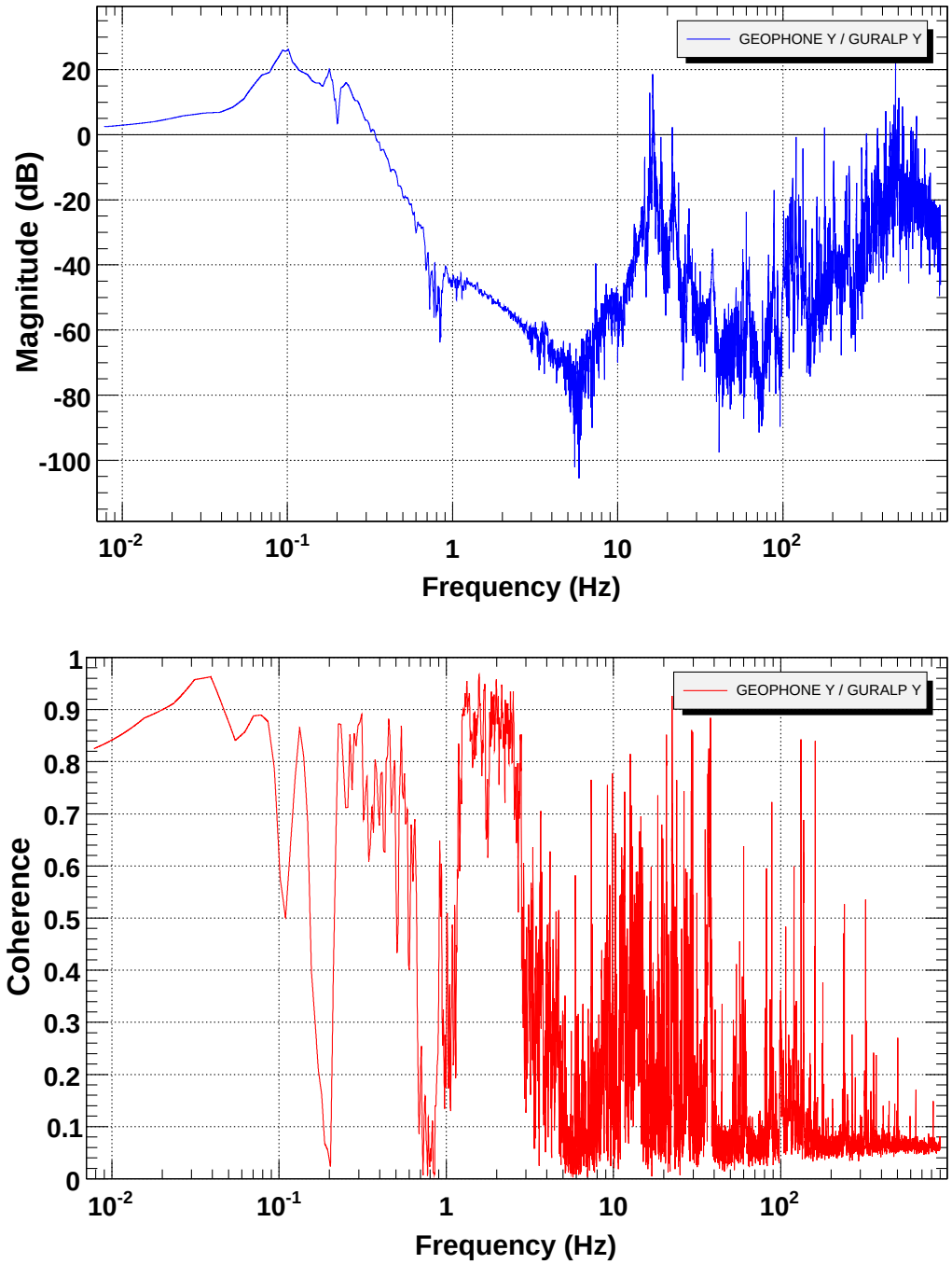

Figure 6.13: Active performance. Horizontal Transmissibility along *y*. In this case the coherence is higher than for *x* and the measurement is less noisy. Also in this case an attenuation of -70 dB is reached at 4 Hz. The geophone noise floor is reached at about 20 Hz.

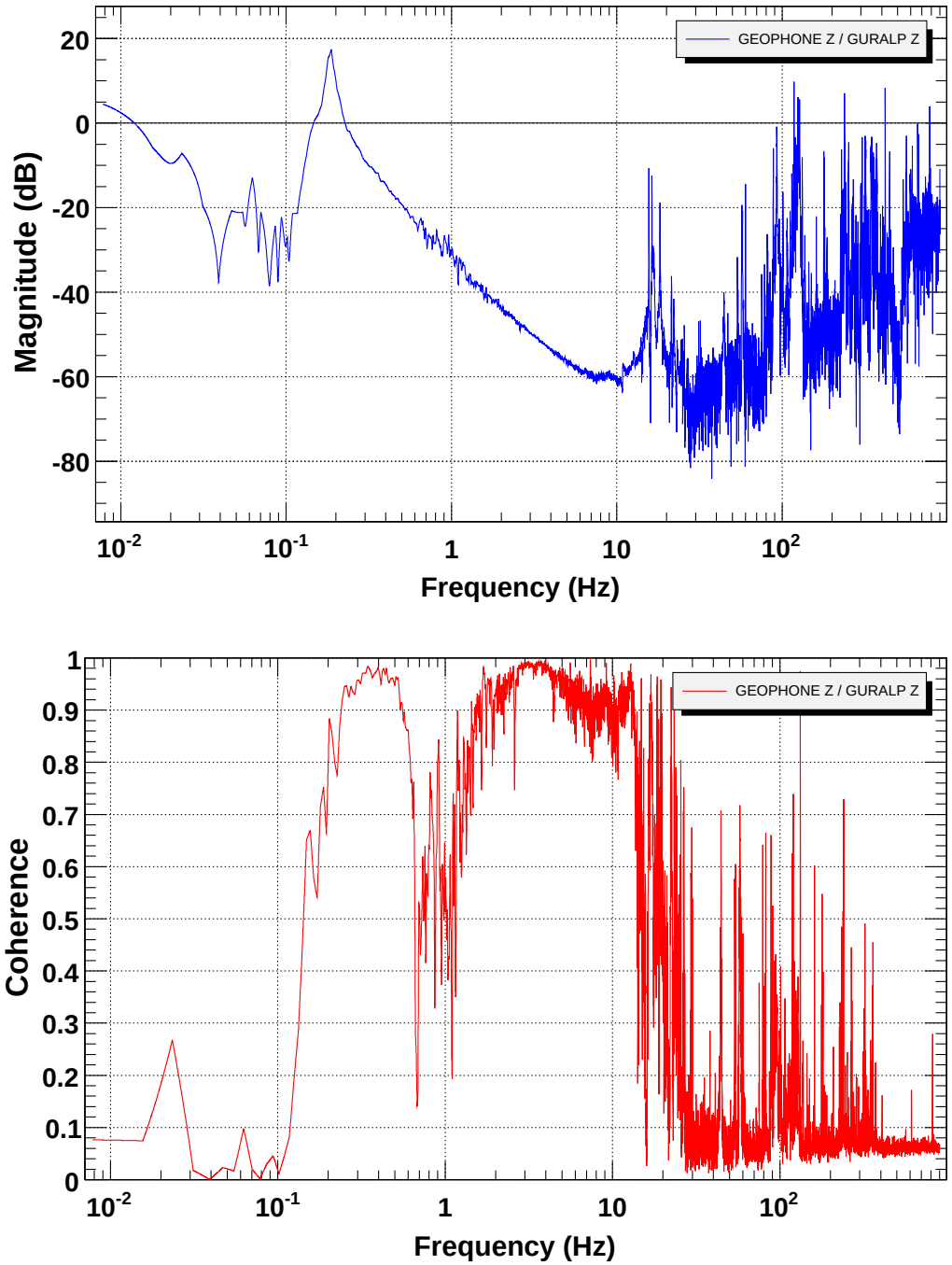

Figure 6.14: Active performance. Vertical transmissibility along z. In the vertical direction the coherence is almost zero at very low frequency but is good above. As a result we have a cleaner measurement than the horizontal ones. An attenuation of -60 dB is reached at 10 Hz, then the geophone noise floor is reached

Chapter 7

Conclusions

HAM-SAS represents the convergence of more than ten years of R&D carried out at LIGO by the SAS group to develop passive and 'soft' solutions for the seismic isolation systems of Advanced LIGO. The several technologies produced and the know-how acquired in the past years merged into one complex system designed for a specific task in the intermediate and advanced interferometers. The HAM-SAS first item produced served as a test bench for the SAS systems for Advanced LIGO, to prove to measure up the leap from the lab to the site, from single separate systems to a multi stage reliable attenuator for an actual high-requirement optical bench. The results discussed in this thesis show that HAM-SAS was able to accomplish that task. We proved that the system is able to support and control the HAM optics table in in a facility similar to those of the sites that the LASTI vacuum chambers reproduces. We showed that along each degree of freedom the system, in its passive configuration, responds like a second order filter with attenuation that manifestly falls as $1/\omega^2$ up to 10 Hz, reaching -60 dB in the vertical and -70 dB in the horizontal. Above that frequency the attenuation is limited by the familiar plateaus produced by the center of percussion effect of inverted pendulums and GAS filters. This made us confident that, having the possibility to implement the SAS solutions for this limitations, an additional order of magnitude in attenuation could be likely achieved in all directions.

The geometry of the system allowed us to apply straightforward control strategies. Vertical and horizontal degrees of freedom are in first approximation independent in most of the frequency range. For both the horizontal and the vertical stages we treated each mode individually and designed control loops to damp the resonances and control the static position. With such limited bandwidth controls we could bring the displacement noise power spectrum of the platform to meet the Advanced LIGO requirements for the HAM chambers practically at all frequencies. Since the controls inevitably re-inject some noise at high frequency, a further improvement of the performance would come from setting the vertical modes at

lower frequencies by re-tuning the GAS filters, improving the tilt correction system and adding some mass to the IP table. Since the Q factors reduce with ω^2 we expect that the reduction of the resonant frequencies will also reduce or eliminate the need for viscous resonance damping.

The residual motion at very low frequency, especially in the horizontal degrees of freedom, was larger than expected. In that frequency region we found the sensitivity limit of the geophone sensors and of the seismometers which made hard to clearly distinguish between the contribution from the environment and the part played by the system. We suspect the role of the ground angular noise to be determinant in overwhelming the sensor signals. Unfortunately no reliable measurement of the angular spectrum could be obtainable from the available seismometers on ground. The issue of the seismic angular noise touches HAM-SAS but it is getting growing attention from both LIGO and Virgo in view of advanced suspensions.

HAM-SAS showed very interesting performances as a seismic attenuation system. It was a complex project and it happened within a very tight time schedule that did not leave sufficient room for the complete optimization of the system. As we could expect from a prototype, we encountered many problems and difficulties, but we solved many and we learned from each of them becoming confident in the HAM SAS potentialities as a platform for seismic isolation in Advanced LIGO.

Bibliography

[1] A. Einstein *Approximative integration of the field equations of gravitation* in The Collected Papers of Albert Einstein, pp. 201-210, Princeton University Press, 1987.

[2] R. Hulse and J. Taylor, *Discovery of a pulsar in a binary system*, The Astrophysical Journal, vol. 195, pp. L51-L53, 1975.

[3] L. D. Landau and E. M. Lifshitz, *The Classical Theory of Fields*, Pergamon Press

[4] DeSalvo R., *Passive, non-linear, mechanical structures for seismic attenuation 5th ASME Int. Conf. on Multibody Systems, Nonlinear Dynamics and Controls* (Long Beach, CA, 24-28 Sept.), and references therein (LIGO-P050001-00-D).

[5] Robertson N et al 2004 Proc. SPIE 5500 81-91 .

[6] Abbott R et al, *Seismic isolation enhancement for initial advanced LIGO*, Class. Quantum. Grav. 21 S915-921

[7] Wang C. et al, *Constant force actuator for gravitational wave detectors seismic attenuation systems*, Nucl. Instrum. Methods A 489 563-9.

[8] Tariq H et al, *The linear variable differential transformer (LVDT) position sensor for gravitational wave interferometer low-frequency controls*, Nucl. Instrum. Methods A 489 570-6 .

[9] C. Hardham et al, *Quiet Hydraulic Actuators for LIGO*,Proceedings of Control of Precision Systems, ASPE Topical Meeting, April 2001.

[10] C. Hardham et al, *Multi-DOF Isolation and Alignment with Quiet Hydraulic Actuators*, LIGO-P040021-00-R.

[11] Yumei Huang, Virginio Sannibale, Valerio Boschi, Dennis Coyne, Riccardo DeSalvo, *Spring box simulations*, LIGO Document LIGO-T03xxxx-yy-D

[12] G. Cella, V. Sannibale, R. De Salvo, S. Màrka, A. Takamori, *Monolithic Geometric Anti-Spring Blades*, gr-qc/0406091, NIM A 540 (2005) 502-519.

[13] S. Braccini, F. Frasconi, et al., *The maraging-steel blades of the Virgo super attenuator*, Meas. Sci. Technol. 11 (2000) 467-476.

[14] A. Stochino, *Performance Improvement of the Geometric Anti Spring (GAS) Seismic Filter for Gravitational Waves Detectors*, SURF-LIGO 2005 Final Report, LIGO-P050074-00-R.

[15] A. Stochino, R. De Salvo, Y. Huang, V. Sannibale, *Improvement of the seismic noise attenuation performance of the Monolithic Geometric Anti Spring filters for Gravitational Wave Interferometric Detectors*, NIM, accepted for publication (2007)

[16] Peter R. Saulson, *Foundamentals of Inteferometric Gravitational Waves Detector*, World Scientific.

[17] A. Abramovici et al., Science **256** (1992) 325.

[18] The VIRGO Collaboration, *VIRGO Final Design Report*, (1997).

[19] K. Danzmann et al., Max-Plank-Institut für Quantenoptik Report, (1994).

[20] K. Tsubono, *Gravitational Wave Experiments*, World Scientific, pp.122 (1995).

[21] C. Casciano, *Seismic Isolation for the Test Masses of the VIRGO Gravitational Wave Antenna*, PhD Thesis, University of Pisa (2002).

[22] M. Barton, A. Bertolini, E. Black, G. Cella, E. Cowan, E. D'ambrosio, R. DeSalvo, K. Libbrecht, V. Sannibale, A. Takamori, N. Viboud, P. Willems, H. Yamamoto, *Proposal of a Seismic Attenuation System (SAS) for the LIGO Advanced Configuration (LIGO-II)*, T990075-00, 1999, LIGO Internal Note.

[23] A. Takamori, et al., *Mirror Suspension System for the TAMA SAS*, Class. Quantum Grav. **19**, 1615, (2002).

[24] *Gravitational Wave Detection II*, Proceedings of the 2nd TAMA International Workshop held 19-22 October, 1999 in Tokyo, Japan. Universal Academy Press Frontiers Science Series Edited by S. Kawamura and N. Mio. 32 (2000) 311.

[25] G. Cella, R. DeSalvo, V. Sannibale, H. Tariq, N. Vibound, and A. Takamori, Nucl. Instrum. Meth. A, **487**, 652, (2002).

[26] A. Bertolini, G. Cella, R. DeSalvo, and V. Sannibale, Nucl. Instrum. Meth. A, **435**, 475, (1999).

[27] H. Brody, *The sweet spot of a baseball bat*, American Journal of Physics, **54**(7), 640-643 (1986).

[28] G. Losurdo, et al.: *An inverted pendulum pre-isolator stage for VIRGO suspension system*, Rev. Sci. Instrum., 70, 2507-2515 (1999).

[29] G. Cella, V. Sannibale et al., *Monolithic geometric anti-spring blades*, Nucl. Instr. and Met. A **540** (2005) 502-519.

[30] M. Ando, A. Bertolini, G. Cella, R. DeSalvo, *Report to NSF on the TAMA-SAS Passive Seismic Attenuation Chain Test for the Tokyo University 3 meter Interferometer*, LIGO-T010006-00-R.

[31] G. Losurdo, *Ultra-Low Frequency Inverted Pendulum for the VIRGO Test Mass Suspension*, Tesi di Dottorato di Ricerca in Fisica, Scuola Normale Superiore di Pisa - Classe di Scienze, Italia Ottobre 1998.

[32] P. Raffai, et al., *Inverted Pendulum as Low Frequency Pre-Isolation for Advacned Gravitational Wave Detectors*, submitted to LSC.

[33] H. Tariq, et al. *The Linear Variable Differential Transformer (LVDT) Position Sensor for Gravitational Wave Interferometer Low-frequency Controls*, Nuclear Instruments and Methods in Physics Research Section A, Volume 489, Issue 1-3, p. 570-576.

[34] M. Mantovani, R. DeSalvo, *One Hertz Seismic Attenuation for Low Frequency Gravitational Waves Interferometers*, accepted for publication on Nucl. Instr. and Meth. (2005).

[35] A. Bertolini et al, *Design and prototype tests of a seismic attenuation system for the advanced-LIGO output mode cleaner*, Class. Quantum Grav. **23** S111-S118, (2006).

[36] Ligo Internal Document, D051100 to 051199 (2006)

[37] M. Husman, *Suspension and Control for Interferometric Gravitational Wave Detectors*, Ph.D. Thesis, University of Glasgow (2000).

[38] V. Sannibale et al., *A new seismic attenuation filter stage (MGASF) for advanced gravitational wave interferometers detectors*, submitted to NIM (2006).

[39] M.Beccaria, et al., *Nuc. Intrum. Meth. in Phys. Res. A.*, **394**,397-408 (1997).

[40] C. Bradaschia, et al., Nucl. Instrum. Meth. A, 289, 518 (1992).

[41] J. Hough, K. Danzmann, et al., GEO600 Proposal, unpublished (1994).

[42] K. Kuroda, et al., in Proceedings of the 1st International Conference on GW: Sources and Detectors, eds. F. Fidecaro, I. Ciufolini, World Scientific, Singapore (1997). (1994).

[43] LIGO Scientific Collaboration, ed. P Fritschel, *Advanced LIGO Systems Design*, LIGO Document T010075-00-D (2001).

[44] Torrie C.I., *Development of the suspensions for the GEO 600 gravitational wave detector*, PhD thesis, (2000), University of Glasgow.

[45] H. Goldstein, *Classical Mechanics*, Addison-Wesley.

[46] J. J. D'Azzo, C. H. Houpis, S. N. Sheldon, *Linear Control System Analysis and Design with Matlab*, Fifth Edition, Marcel Dekker, Inc. (2003)

[47] A. Bertolini, *High sensitivity accelerometers for gravity experiments*, PhD. Thesis, University of Pisa, LIGO-P010009-00-Z

[48] Julius O. Smith III, *Mathematics of the Discrete Fourier Transform (DFT), with Audio Applications*, Second Edition, W3K Publishing, 2007.

[49] P. Fritschel, *HAM Seismic Isolation Requirements*, LIGO Internal Document T060075-00-D, (2006)

[50] P. Fritschel et al., *Seismic Isolation Subsystem Design Requirements Document*, LIGO Internal Note E990303-00-D, (2001)

[51] J. Peterson, *Observations and Modeling of Seismic Background Noise*, USGS Report 93-322 (1993)

[52] G. Losurdo, *MIT Lunch Talk*, May 17th 2007, LIGO MIT

[53] R. De Salvo, S. Marka, K. Numata, V. Sannibale, A. Takamori, H. Tariq, E.J. Ugas, T. Yoda, Y. Aso, A. Bertolini, *Study of quality factor and hysteresis associated with the state-of-the-art passive seismic isolation system for Gravitational Wave Interferometric Detectors.*, Nucl. Instrum. Meth. A 538:526-537, 2005